Exploiting MRI Information For Improved Kinetic Modelling of Dynamic PET Data

Hasan Sari

A dissertation submitted in partial fulfillment

of the requirements for the degree of

Doctor of Philosophy

of

University College London.

Department of Medical Physics and Biomedical Engineering

University College London

November 18, 2016

I, Hasan Sari, confirm that the work presented in this thesis is my own. Where information has been derived from other sources, I confirm that this has been indicated in the work.

Abstract

Kinetic analysis of dynamic PET data requires an accurate estimation of the concentration of the available tracer in blood plasma, also known as the arterial input function (AIF). The gold standard method to determine the AIF involves serial blood sampling and is avoided in practice due to its invasiveness. An image derived input function (IDIF) can be a blood-free alternative but its accuracy is limited due to partial volume (PV) effects caused by the restricted spatial resolution of PET scanners. Furthermore, IDIFs are not accurate when metabolite products are present in the blood. Magnetic resonance imaging (MRI) can provide complementary information to PET with high spatial resolution and excellent soft tissue contrast. Furthermore, dynamic MRI techniques can be reliably used to measure the AIF, the concentration of contrast agent in plasma, due to their high temporal resolution.

The underlying aim of this research is to improve IDIF estimation in PET, utilising spatial and temporal information from MRI. An IDIF measurement method was developed which involves segmentation of carotid arteries from MR angiography images and uses a practical PVC method to correct for PV effects. It was demonstrated that the IDIFs can be used to compute the cerebral metabolic rate of glucose in the brain with no significant difference compared to arterial sampling.

The simultaneous estimation method (SIME) is an alternative technique used to estimate the AIF by fitting time activity curves derived from multiple regions. Due to its computational complexity, SIME is usually complemented with blood samples. In this work, we observed that the early part of an image derived blood curve or an MRI derived AIF could provide prior knowledge regarding the AIF. This was incorporated into SIME to make more accurate kinetic parameter estimations and to perform blood-free analysis of tracers with metabolites.

Acknowledgements

A great many people deserve acknowledgement for their contributions to the work presented in this thesis.

First and foremost, I would like to thank Professor Brian Hutton for his supervision, encouragement and guidance throughout my PhD. His support, experience and enthusiasm have been indispensable. I am also grateful to Dr Kjell Erlandsson for the great supervision, support and guidance he gave me during this time. He has been always there to be a daily source of practical help and ideas. I have learnt much from our discussions regarding PET imaging and kinetic analysis.

I am also thankful to Dr David Atkinson for his feedback on MRI analysis techniques and for his proofreading of this thesis. I am very grateful to Prof Ian Law and Dr Lisbeth Marner from University of Copenhagen for provision of clinical datasets.

This work was funded by a joint studentship by Siemens Molecular Imaging and UCL Faculty of Engineering Sciences. I wish to express my gratitude for the funding I received during these years, which also enabled me to present my work at international conferences. I would like to thank Dr Jerome Declerck, Dr Chloe Hutton and Dr Xiao-bo Pan from Siemens Molecular Imaging for their useful discus-

sions and advices throughout this project. I am also thankful to Dr Kris Thielemans and the whole PET-MRI group of UCL for the regular discussions and feedback.

I thank everyone in the Institute of Nuclear Medicine for providing a great place to work. Thanks to my fellow colleagues in the physics research group for their friendship and assistance. In particular, I thank Richard, Alex, Ottavia, Alaleh, Tsai, Beverley and Debora.

Finally, I would like to thank my family and friends for all their support and encouragements. A special thank you goes to my parents Emine and Hüseyin, my brother Barış, and my uncle Mustafa for their endless trust, patience and moral support over the years.

Contents

1 Introduction **23**

1.1 Motivation 25

1.2 Organisation of the Thesis 28

1.3 Contributions 30

2 Background Theory to PET and MR Imaging **33**

2.1 Theory of Positron Emission Tomography 33

2.2 PET Image Formation 35

2.2.1 Data Corrections 38

2.2.2 Partial Volume Correction 40

2.3 Theory of Magnetic Resonance Imaging 45

2.4 Image Formation in MRI 50

2.4.1 Structural MR pulse sequences -MPRAGE 52

2.4.2 Vascular MR pulse sequences 53

2.4.3 Dynamic MR pulse sequences 55

2.5 The Physical Basis of PET/MRI 58

2.6 Coregistration of PET/MR data 62

2.7 Attenuation Correction in PET/MR scanners 64

3 Quantitative Analysis of PET and MRI data 67

3.1 PET 67

3.1.1 Quantification in PET 67

3.1.2 Principles of PET tracer kinetics 69

3.1.3 Compartmental Model Analysis 71

3.1.4 Graphical Analysis Techniques 77

3.2 MRI 79

3.2.1 Dynamic MRI 79

3.2.2 DCE-MRI Quantification Techniques 81

3.2.3 Theory of DSC-MRI Acquisition and Quantification 83

3.3 Arterial Input Function 85

4 Improved quantification of clinical dynamic FDG images using image derived input functions with MR-defined carotid arteries 91

4.1 Introduction 91

4.2 Literature Survey 92

4.3 Theory of the Single Target Correction method 98

4.4 Experiments with simulations 101

4.4.1 Generation of simulated data 101

4.4.2 Application of the STC method to the simulated data 103

4.5 ^{18}F-FDG Experiments 105

4.5.1 Materials 105

4.5.2 Data Analysis 107

4.5.3 Performance Evaluation of Input Functions 111

4.6 Results 112

4.6.1 Simulation results 112

4.6.2 ^{18}F-FDG results 116

4.7 Discussions 122

4.8 Conclusions 129

5 Exploiting Prior Information in the PET SIME Method 131

5.1 Introduction 131

5.2 Literature Survey 133

5.3 Simultaneous Estimation Method (SIME) 135

5.4 Simulation work 138

5.4.1 Materials and Methods 138

5.4.2 Analysis of parameter estimates 142

5.5 Results 144

5.6 Discussion and Conclusions 151

6 Comparison of PET and MRI derived input functions 153

6.1 Introduction 153

6.2 Literature Review 154

6.3 Accounting for different injection rates 158

6.4 Materials and Methods 161

6.4.1 Validity of the proposed AIF model 161

6.4.2 Simulated Input Functions 162
6.4.3 Clinical Data 163
6.5 Results 165
6.5.1 Validity of the proposed AIF model 165
6.5.2 Simulated and Clinical AIF Fits 168
6.6 Discussions and Conclusions 171

7 Application of Constrained SIME to ^{18}F-FDG and ^{11}C-SB207145 tracers 174

7.1 Introduction 174
7.2 Materials and Methods 175
7.2.1 ^{18}F-FDG data 175
7.2.2 [^{11}C]-SB207145 PET data 178
7.2.3 [^{11}C]-SB207145 Constrained SIME model 182
7.3 Results 187
7.3.1 ^{18}F-FDG Results 187
7.3.2 [^{11}C]-SB207145 Results 191
7.4 Discussions and Conclusions 202

8 Conclusions and future work 208

8.1 Conclusions 208
8.2 Future work 213

Bibliography 216

List of Figures

1.1 Project outline 27

2.1 Positron emission and annihilation process 34

2.2 PET coincidence detection 36

2.3 Scatter and random coincidence events 40

2.4 Partial volume effects 42

2.5 Alignment of spins in a magnetic field 46

2.6 T_1 recovery and T_2 relaxation curves 47

2.7 Illustration of spin echo pulse sequence 49

2.8 MRI encoding trajectories 51

2.9 Maximum intensity projection of a TOF-MR angiography image . . 54

2.10 PET Detector assembly in Siemens Biograph mMR 61

2.11 Schematic representation of Siemens Biograph mMR scanner 61

2.12 Example attenuation maps derived from UTE and atlas-based methods 66

3.1 Dynamic PET vs. static PET 68

3.2 Schematic representation of compartmental modelling 72

3.3 Tissue compartmental models 74

3.4 Patlak plot 78

3.5 Logan plot 79

3.6 Tofts model 82

3.7 Arterial input function 86

3.8 Formation of metabolites 89

4.1 Generation of simulated ^{18}F-FDG data 102

4.2 Image-derived PSF measurement 104

4.3 Images used in the study 107

4.4 Segmented arteries 108

4.5 PSF FWHMs calculated for each subject 110

4.6 Plasma to wholeblood tracer concentration ratio 110

4.7 Performance of STC in simulated data 114

4.8 Effect of segmentation errors on estimated PSF 115

4.9 PVC recovery performance with different PSFs 115

4.10 Illustration of IDIFs 117

4.11 Area under curve of estimated AIFs 118

4.12 Bland-Altman Plots of cMRglc estimates 120

5.1 Simultaenous estimation approach 136

5.2 Simulated time activity curves 140

5.3 Simulated AIF with different λ_1 values 143

5.4 Bias on estimated influx constant values 145

5.5 Absolute bias on estimated kinetic microparameters 147

5.6 Coefficient of variation on estimated influx constant values 148

5.7 Sensitivity analysis results 149

5.8 Results of the inter-individual variability analysis 150

6.1 The Double Butteworth function 160

6.2 Illustration of AIFs with different injection durations 166

6.3 Relationship between injection duration vs $\Delta\tau$ of AIF model 166

6.4 Simulated PET-AIF and MRI-AIFs fitted with 10 parameter AIF model 168

6.5 Population based PET-AIF and MRI-AIF fitted with the proposed AIF function 169

6.6 Fitted AIFs adjusted for different injection durations 170

7.1 TACs used in the constrained ^{18}F-FDG SIME analysis 177

7.2 TACs used in the constrained ^{11}C-SB207145 SIME analysis 181

7.3 Parent fractions fitted with Hill function 185

7.4 Constrained SIME model used to analyse ^{11}C-SB207145 tracer . . . 186

7.5 K_i parameter estimates for ^{18}F-FDG 189

7.6 Kinetic parameters estimates for 4 brain regions in ^{18}F-FDG studies 190

7.7 The population based plasma to whole blood ratio used in ^{11}C-SB207145 analysis 192

7.8 Comparison of image derived and blood sampled whole blood curves 193

7.9 Comparison of whole blood AUCs 194

7.10 Mean metabolite curve estimated using $\text{SIME}_{\text{Hill}}$ 194

7.11 Comparison of parent AIF AUCs 196

7.12 Comparison of estimated V_T values using different methods 197

7.13 Kinetic parameters estimated for 5 brain regions using different methods 198

7.14 Intraclass Correlation Coefficient of V_T estimates 201

List of Tables

2.1 A selection of common PET radiotracers with their characteristics . 34

4.1 Kinetic parameter estimates for grey matter matter 121

4.2 Kinetic parameter estimates for white matter matter 121

5.1 True values of the kinetic parameters used to generate the three time activity curves 138

6.1 Fitted parameters of AIFs with different injection durations 167

6.2 Comparison of fitted κ_1 values when fitted with the 10 parameter AIF Model 170

6.3 Comparison of fitted λ_1 values when fitted with 6 parameter Feng AIF Model 171

7.1 Estimated V_Ts using different number and variations of TACs. Results obtained using AIF samples are present to stand as the true ground. The percentage errors against the gold standard V_T for each method and each region are included. The following TACs are removed to generate the different TAC sets: 4 TACs: sup. fr. cortex, 4 TACs 2: cerebellum, 3 TACs: cerebellum and sup. fr. cortex, 3 TACs 2: cerebellum and hippocampus, 2 TACs: cerebellum, sup. fr. cortex, and hippocampus. 200

Nomenclature

Symbols

α	Flip angle
B_0	Strength of the external magnetic field
C_a	Concentration in arterial blood
a(·)	True image
b(·)	Blurred image
C_{EES}	Concentration in extravascular extracellular space
cMRGlc	Cerebral metabolic rate of glucose consumption
$\otimes$	Convolution
C_B	Concentration of the specifically bound tracer
C_F	Concentration of the tracer in extravascular pool within the tissue
C_P	Parent concentration in plasma
C_{NS}	Concentration of non-specifically bound tracer

C_{PG} Cold glucose concentration in plasma

C_{RBC} Concentration in red blood cells

C_T Concentration in tissue

C_v Concentration in venous blood

C_{WB} Concentration in whole blood

E Extraction fraction

F Blood flow

ω Angular precessional frequency

γ Gyromagnetic ratio

$g_k(\cdot)$ Spill-over term

$h(\cdot,\cdot)$ PSF

K_1 Rate constant for transfer from arterial plasma to tissue

k_2 Rate constant for transfer from tissue to plasma

k_{ep} Rate constant for the transfer from EES to plasma

K_i Influx constant

k_3, k_4 Rate constants

K^{trans} Rate constant for the transfer from the plasma to extravascular extracellular space used in MRI

M_0 Net magnetic moment

μ Attenuation

PS Permeability surface area product

R($\cdot$) Recovery factors

σ Variance in data

T_1 Spin-lattice relaxation

T_2 Spin-spin relaxation

V_b Blood volume

Ω VOI

V_T Volume of distribution

Acronyms / Abbreviations

2D Two dimensional

3D Three dimensional

AIF Arterial Input Function

APD Avalanche Photo Diodes

CSF Cerebral spinal fluid

CT Computed Tomography

DCE-MRI Dynamic Contrast Enhanced MRI

DF Degree of freedom

DSC-MRI Dynamic Susceptibility Contrast MRI

EPI Echo-planar imaging

FBP Filtered Backprojection

FOV Field of view

FWHM Full width at half maximum

Gd Gadolinium

GE Gradient echo

GM Grey matter

GRASS Gradient Recalled Acquisition at Steady State

GTM Geometric Transfer Matrix

HRRT High Resolution Research Tomograph

IDIF Image Derived Input Function

LOR Line of response

LSO Lutetium Oxyorthosilicate

MI Mutual Information

MIP Maximum intensity projection

MLEM Maximum Likelihood Expectation Maximisation

MPRAGE Magnetisation-Prepared Rapid Gradient Echo

MRA MR Angiography

MRI Magnetic Resonance Imaging

MTC Multi-Target Correction

NCC Normalised Cross Correlation

NMI Normalised Mutual Information

ODE Ordinary differential equation

OSEM Ordered Subsets Expectation Maximisation

PET Positron Emission Tomography

PSF Point Spread Function

PVC Partial Volume Correction

PV Partial Volume

RF Radio frequency

SE Spin echo

SIME Simultaneous Estimation Method

SSE Sum of squares error

STC Single Target Correction

SUV Standardised uptake value

TAC Time activity curve

TC Tissue compartment

TOF Time-of-flight

TR Repetition time

UTE Ultrashort echo time

WM White matter

ZTE Zero echo time

Chapter 1

Introduction

Since the discovery of X-ray imaging by Roentgen [Roentgen, 1895] in 1895, diagnostic imaging has been used to look non-invasively inside the human body. In 1953, the first clinical positron imaging device was developed by Brownell et al. [Brownell and Sweet, 1953]. That scanner produced a low resolution image only, but was sensitive in determining if a tumour existed in the brain. In order to further increase sensitivity the first multiple detector positron imaging device was developed in 1962 [Brownell et al., 1969]. That scanner, specifically developed for brain imaging, was used for clinical purposes for nearly a decade and found significant clinical use in cancer imaging and in research to image molecular processes.

Dual-modality imaging systems, such as Positron Emission Tomography (PET) /Computed Tomography (CT), were introduced in 2000s and today, over 5000 PET/CT systems are installed worldwide as PET/CT has become the modality-of-choice for clinical oncology scans [Beyer et al., 2000]. The coregistered anatomical information provided from CT scans benefited PET scanners which lack an equivalent spatial resolution. However, PET/CT has several limitations which could

be overcome by replacing the CT part with an Magnetic Resonance Imaging (MRI) scanner. In clinical systems, PET and CT detectors are not combined together and hence the PET and CT components have to be placed axially. Therefore, PET/CT scanners can only be used for sequential imaging rather than simultaneous. This may lead to errors in image alignment and registration and may result in residual patient motion as the images are obtained at different times. In addition, sequential imaging can limit the accuracy of combined dynamic PET and CT studies as the physiology of the patient may change between the sequential scans. Finally, both PET and CT imaging cause exposure to radiation which limits the use of PET/CT scanners in research studies.

The development of hybrid PET/MRI scanners started in the late 90s and saw some interest as MRI brought some advantages compared to CT in anatomical imaging. MRI offers high resolution images and is able to provide a strong visualisation of soft tissues. On the other hand, PET has a very high sensitivity and is very useful in the imaging of metabolic processes in living bodies, but lacks the spatial resolution offered by MRI. Hence, it can be said that PET and MRI are highly complementary and combination of these two modalities was a natural research topic.

During this decade, fully integrated clinical PET/MRI scanners have been manufactured by Siemens Healthcare and GE Healthcare where a 3 Tesla whole-body MR system hosts a fully integrated PET detector in its isocenter. MRI provided anatomical information with excellent soft tissue contrast and spatial resolution to complement excellent sensitivity of PET. Advent of this simultaneous PET/MR modality opened the doors for a wide research area, and researchers, radiologists

and nuclear medicine physicians started to evaluate the clinical potential of this new scanner and to validate new imaging applications. The technology and specifics of these integrated PET/MRI systems are further described in this thesis.

1.1 Motivation

In both PET and MRI, dynamic data can be acquired immediately after an administration of a PET tracer or Gadolinium based MR contrast agent. As most PET tracers can get into the cells and get bound or metabolised there, PET imaging provides information about intracellular processes whereas MR can only provide insight about processes happening in the extracellular space as Gd chelates cannot penetrate into cells.

Both dynamic PET and MRI data can be analysed using compartmental kinetic analysis methods which require an accurate knowledge of the tracer/contrast agent concentration in the blood over time, also known as the arterial input function (AIF). In both PET and MR imaging, the gold standard method to measure the AIF involves collection of arterial samples during the scanning period, which makes it an invasive and laborious process. Furthermore, MR compatible arterial sampling instruments are required for arterial sampling in a PET/MR scanner which can add to the costs. These limitations stop many research centres from collecting arterial samples and there is therefore a need for more practical and non-invasive alternatives.

The AIF can be measured using image-based methods from reconstructed PET and MRI images, but these techniques have separate limitations and data correction

steps that involve several assumptions. PET data can provide truly quantitative information regarding the concentration of the PET tracer in the arterial plasma at a specific time, whereas MRI scanners can only approximately relate the signal to the contrast agent concentration. On the other hand, MRI can have a very high temporal resolution which can be used to track the rapid changes in the early phase of the dynamic scan whereas PET scanners are limited to lower temporal sampling as they require sufficiently high counts to have meaningful data. Furthermore, due to the lower spatial resolution of PET scanners, PET images can suffer from spill-over effects from surrounding tissues, hence an AIF measurement from small arteries will be contaminated from signal from background regions.

Acquiring dynamic PET and MRI data simultaneously can offer a better spatial and/or temporal correlation of datasets from both modalities. Information from these two modalities can be used to complement each other and enable combined analysis of dynamic PET and MRI datasets. Simultaneously acquired PET and MRI images can be aligned more easily as the patient motion and positioning is not expected to change much between image acquisitions. Coregistered MR images with higher spatial resolution can be used to obtain a more accurate segmentation of the anatomical structures and use them to perform PVC and regional analysis of PET images. This can also be applied to estimate an Image-derived input function (IDIF) from PET images more accurately by utilising spatial information from MR images. Simultaneous PET/MR imaging can be used to estimate PET-AIF and MRI-AIF from the same scan and one can hypothesise that mutual information is present between these two AIFs. If a reliable AIF conversion between PET-AIFs and MRI-

AIFs could be performed, the complementary information from both modalities would not only enable us to devise more accurate non-invasive methods to measure the AIF, but would also provide an opportunity for a joint kinetic modelling of data from both modalities.

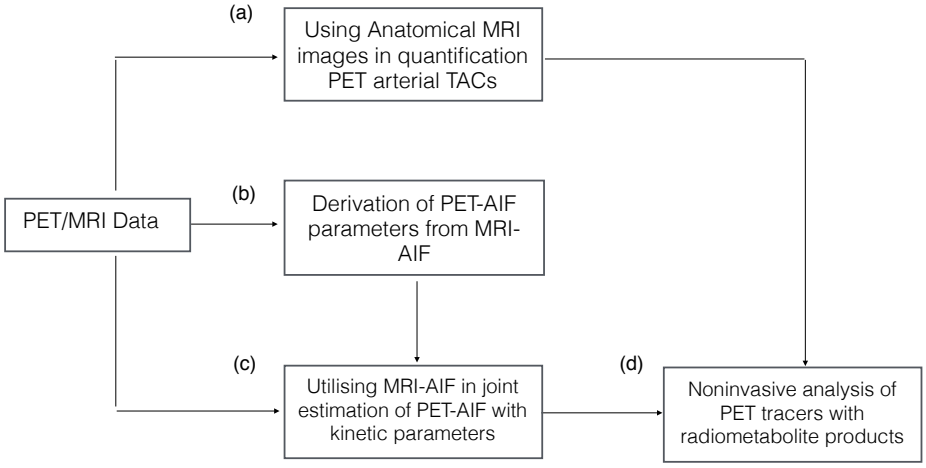

Figure 1.1: Brief outline of the project aims

The goal of this research project is to develop non-invasive PET input function measurement techniques and to improve these by utilising MRI data. Our ultimate aim is to apply developed methods to non-invasively analyse PET tracers with radio-labelled metabolites, without the need to collect any arterial samples. The steps we have been taking to reach this aim are illustrated in figure 1.1 and can be listed as:

(a) Improving the quantification of image derived PET arterial time activity curves (TACs) by using anatomical MR images in the delineation of arterial voxels and partial volume correction.

(b) Testing if a parameter conversion between a PET-AIF and an MRI-AIF can be

performed

(c) Constraining the PET Simultaneous Estimation Method (SIME) which jointly estimates the input function and kinetic parameters by incorporating prior information from PET or MRI blood curves.

(d) Using the constrained SIME method with prior AIF information to perform blood-free kinetic analysis of PET data when radiometabolites are present in the blood plasma.

1.2 Organisation of the Thesis

The aim of the first chapter is to give an introduction to PET/MRI imaging, state our motivation and direction of research. In the second chapter, the physical theory of PET and MRI imaging is briefly presented. The basics of PET and MRI scanners are described and various data acquisition and data correction techniques are outlined. The design of hybrid PET/MRI scanners is also briefly described. Methods used in the coregistration of PET and MRI images are presented and finally, PET attenuation correction techniques with MR derived attenuation maps are summarised.

In Chapter 3, an introduction to dynamic imaging in PET and Dynamic MRI is given, including the kinetic analysis and compartmental modelling of these dynamic data. Introduction to both Dynamic Contrast Enhanced MRI (DCE-MRI) and Dynamic Susceptibility Contrast MRI (DSC-MRI) is also given in this chapter. The need for accurate measurement of the arterial input functions in both dynamic PET and MRI analysis is explained and a comparison of different methods used for

measuring AIF is included.

Chapter 4 includes the methodology developed to derive an arterial input function from PET images by using anatomical information from MR angiography images. MR angiography images with almost five times smaller voxel size than PET images are used to segment the carotid arteries. A novel PVC is also presented in this chapter which only requires the segmentation of carotid arteries and does not need parcellation of background regions. The PVC method is used to correct PVC of dynamic PET frames for image derived input function extraction. The method is tested on ^{18}F-FDG datasets and validated against the gold standard arterial plasma samples.

Simultaneous estimation of the arterial input function and kinetic modelling of multiple brain regions is also possible without any need for separately measuring the input function from images or blood samples. However, this method is computationally complex due to the high number of parameters to be estimated and may not always work with the desired accuracy. In Chapter 5, the effects of incorporating prior information to reduce the number of input function parameters on estimated kinetic parameters is presented. The proposed method is evaluated with simulated ^{18}F-FDG time activity curves.

In Chapter 6, the comparison of PET derived arterial input functions and MRI derived arterial input functions are made. The necessary corrections such as accounting for different injection durations are presented in detail. Input function from ^{18}F-fluorocholine and DSC-MRI studies are compared visually after necessary corrections. These AIFs were fitted using analytical input function models and

a comparison of fitted parameters is also presented.

In Chapter 7, the constrained SIME method with prior AIF information is used to analyse clinical ^{18}F-FDG and ^{11}C-SB207145 PET datasets. The results obtained with the proposed method are validated against results obtained using the gold standard arterial blood samples. Statistical tests are also performed to evaluate the performance of the proposed method.

Finally, the conclusions of the research are further discussed in chapter 8 and findings from each chapter are summarised. Suggestions for possible future research directions are also discussed in this final chapter.

1.3 Contributions

The work included in this thesis was presented in the following conferences and is published as following:

Journal papers

- H. Sari, K. Erlandsson, K. Thielemans, D. Atkinson, S. Arridge, S. Ourselin, and B. Hutton, Incorporation of MRI-AIF information for improved kinetic modelling of dynamic PET data, 2015. IEEE Transactions on Nuclear Science, 62 (3), 612-618.

- H. Sari, K. Erlandsson, I. Law, H. Larsson, S. Ourselin, S. Arridge, D. Atkinson, and B. Hutton, Estimation of an image derived input function with MR-defined carotid arteries in FDG-PET human studies using a novel PVC method, 2016. Journal of Cerebral Blood Flow and Metabolism, in press

Conferences with full-length proceedings

- H. Sari, K. Erlandsson, A. Barnes, D. Atkinson, S. Arridge, S. Ourselin, and B. Hutton, Exploiting an MRI derived arterial input function to improve the PET simultaneous estimation method: validation of assumptions, 2014 IEEE Nuclear Science Symposium and Medical Imaging Conference (NSS/MIC), Seattle, WA, 2014, 1-4

Conference abstracts

- H. Sari, K. Erlandsson, K. Thielemans, D. Atkinson, S. Arridge, S. Ourselin, and B. Hutton, Incorporation of MRI-AIF information for improved kinetic modelling of dynamic PET data, Conference on PET/MR and SPECT/MR (PSMR) 2014, Kos Island, Greece, 2014, EJNMMI Physics. 2014;1 (Suppl 1):A43.

- H. Sari, K. Erlandsson, A. Barnes, D. Atkinson, S. Arridge, S. Ourselin, and B. Hutton, Modelling the impact of injection time on the bolus shapes in PET-MRI AIF Conversion, Conference on PET/MR and SPECT/MR (PSMR), Kos Island, Greece, 2014, EJNMMI Physics. 2014;1 (Suppl 1):A54.

- H. Sari, K. Erlandsson, I. Law, H. Larsson, S. Ourselin, S. Arridge, D. Atkinson, and B. Hutton, Estimation of an image derived input function with MR-defined carotid arteries in FDG-PET human studies using a novel PVC method, 2015 Society of Nuclear Medicine and Molecular Imaging Annual Meeting, Baltimore, USA, J Nucl Med May 1, 2015 vol. 56 (Suppl 3): 1734

- H. Sari, K. Erlandsson, I. Law, L. Marner, H. Larsson, S. Ourselin, S. Arridge, D. Atkinson, and B. Hutton, Blood free modelling of PET tracers with metabolites using MRI corrected whole blood and a constrained simultaneous estimation approach, Conference on PET/MR and SPECT/MR (PSMR) 2016, Cologne, Germany, 2016

Chapter 2

Background Theory to PET and MR Imaging

2.1 Theory of Positron Emission Tomography

In positron emission tomography (PET), small amounts of positron-emitting radionuclides are tagged to molecules of interest, known as radiotracers and are administered to the subject. PET scanners detect the photons emitted as the result of radioactive decay and convert this measurement into a meaningful image which shows the distribution of the radionuclide.

During the radioactive decay of the PET tracer, a positron and a neutrino are ejected from the nucleus. The positron travels a finite distance, called positron range, and gradually loses its kinetic energy until it comes to near rest and then combines with an electron, causing an annihilation. This annihilation emits two 511 keV photons in opposite directions, 180° to each other, as illustrated in figure 2.1. PET imaging relies on the detection of these annihilation events which is further

explained in section 2.2.

Table 2.1: A selection of common PET radiotracers with their characteristics

Tracer	Radio Nuclide	Half-life (min)	Biological Process
^{18}F-FDG	^{18}F	109.8	Glucose metabolism
^{18}F-FMISO	^{18}F	109.8	Hypoxia
^{11}C-methionine	^{11}C	20.4	Cellular amino acid uptake
^{15}O-water	^{15}O	2.03	Perfusion
^{82}Rb-Chloride	^{82}Rb	1.27	Perfusion

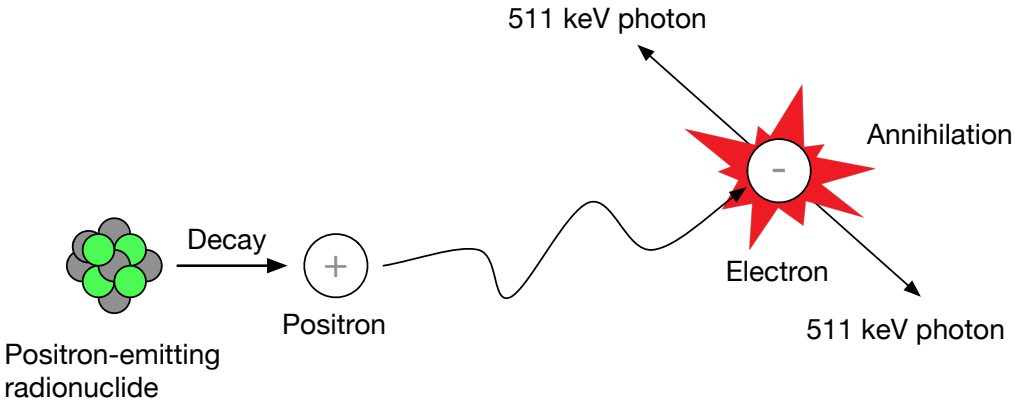

Figure 2.1: The process of positron emission, decay and subsequent annihilation emitting two photons in opposite directions.

Different chemical compounds, which are often used by the body like glucose and water, can be tagged with positron emitting radionuclides to generate radioactive tracers. Radionuclides with short half lives such as ^{18}F, ^{11}C, ^{13}N and ^{15}O are usually used in PET imaging. New tracers are continuously being developed in order to reveal different aspects of the process of interest. Some of the most commonly used radiotracers are listed in table 2.1 [International Atomic Energy Agency, 2008] [Sharma and McConathy, 2013].

Among all these PET radiotracers listed in table 2.1, ^{18}F-fluorodeoxyglucose (^{18}F-FDG) is the most commonly used. ^{18}F-FDG is a radiolabelled glucose ana-

logue and it is used in PET imaging to determine sites where glucose metabolism is high. ^{18}F-FDG is taken up by glucose using cells such as brain, kidney or cancer cells and gets phosphorylated, preventing the glucose from being released again from the cell. One application of ^{18}F-FDG PET imaging is to detect tumours in oncology imaging [Conti et al., 1996] [Fletcher et al., 2008]. Since the cancer cells grow and divide faster than normal cells, they require more energy and metabolise more glucose, resulting in increased glucose uptake. As a result of that, these tissues have higher ^{18}F-FDG uptake in the resulting PET images. Another common tracer, ^{15}O-water is a freely diffusible tracer and does not depend on the metabolic-trapping mechanism which makes it useful for applications to measure blood flow and perfusion [Lubberink et al., 2010] [Salerno and Beller, 2009].[^{18}F]fluorocholine (FCH) is a commonly used tracer for imaging brain tumours citeLam2011 [Roselli et al., 2010] but also for prostate studies [Bauman et al., 2012]. It targets cellular membrane phospholipids, primarily in cancer cells. It penetrates into cells through choline transporters and accumulates in tumours due to malignancy-induced overexpression of choline kinase.

2.2 PET Image Formation

The principle of PET imaging is the detection of the photons emitted from the positron annihilation. A typical PET scanner is formed by multiple rings arranged in a cylindrical shape. Once the scintillation detectors detect a pair of photons arriving in coincidence, where a conincidence detector decides if the detection of this pair of scintillation photons occurred within a specific timing window (6-10 ns) [Cherry

and Dahlbom, 2006], they emit lower energy visible light photons which are detected and amplified by the photomultiplier tubes or photo diodes. When the two photons are detected within in a coincidence window, it shows that the positron annihilation occurred somewhere on the line of response (LOR) connecting the two opposing detectors (Figure 2.2). The rate of detections, count rates, will be proportional to the activity of the source.

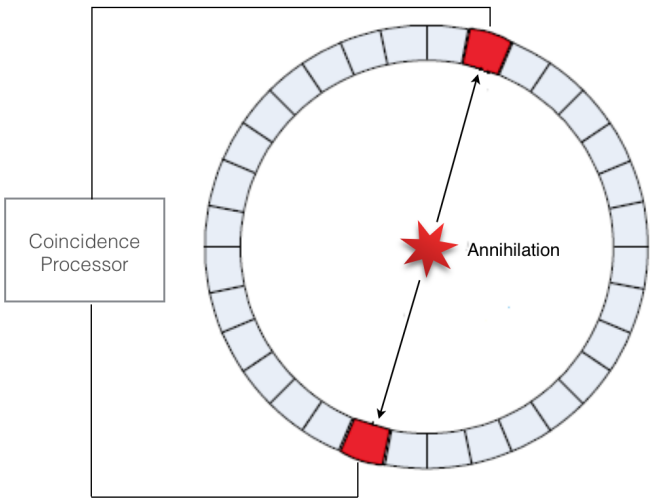

Figure 2.2: PET coincidence detection of a pair of 511keV photons emitted from an annihilation. A line of response (LOR) is identified between the two detectors

During the PET acquisition, coincidence events related to each LOR between pairs of detectors are stored in bins where LORs passing through the same point within the object form a sinusoid curve in the raw data histogram, called a sinogram. The set of these projections produces the sinogram for a single plane and these sinograms are reconstructed to generate a 3D image of the subject.

As an alternative, list-mode acquisition can be performed which also records the arrival times of the events in a list. The list-mode data are sorted into sinograms

with additional timing information. The disadvantage of acquiring in list-mode is that it occupies larger memory space. On the other hand, list-mode data can be used to avoid binning of LORs into detector pixels or voxels, which can lead to information loss. Direct reconstruction from list-mode data can avoid this step, fully utilising the temporal and spatial list-mode information. List-mode acquisitions have applications in high resolution image reconstruction [Reader et al., 2002], dynamic imaging [Nichols et al., 2002] and motion correction [Carson et al., 2003].

Once the sinograms are obtained, the source distribution can be reconstructed using various methods. The aim of an image reconstruction method is to provide an image which describes the distribution of the radiotracer within the object from the detected coincidence events. One way of reconstructing PET data is using the Filtered Back Projection (FBP) method, which is a version of the inverse Radon transform [Kak and Slaney, 1988]. In this method, a filter function is applied to the projections in Fourier space and the activity is back-projected in the image space. The backprojection causes a blurring effect of the object and this is corrected by applying ramp filtering as well as a smoothing function. FBP method has the advantage of being very fast and FBP derived images are widely used in quantitative analysis as the resolution and variance in FBP derived images are predictable due to the linear nature of the algorithm.

PET data can also be reconstructed using iterative reconstruction techniques, which are iterative processes where the intermediate image converges toward the 'true' image. Iterative reconstruction aims to model the data collection process and includes statistical variance as well as other factors such as scattered and random

coincidence events. Maximum Likelihood Expectation Maximisation (MLEM) [Shepp and Vardi, 1982] is an iterative algorithm which updates the image at each iteration by using the ratio of estimated projections with the acquired projections until convergence is reached. MLEM is usually regarded as a slow method due to the large number of iterations required to get an optimal solution. Ordered Subsets Expectation Maximisation (OSEM) algorithm [Hudson and Larkin, 1994] was proposed as a more efficient alternative to MLEM. In OSEM, the projections are grouped into subsets and the image is updated once for each subset.

Fully functional time-of-flight (TOF) PET systems were introduced in early 1980s to increase the signal to noise ratio [Lewellen, 1998]. In a TOF PET system, the difference in arrival times between the 2 coincident photons is measured for each annihilation event. This information is used to determine the most likely location of the source along the LOR. The TOF information usually contains uncertainties but even imperfect TOF information helps to improve the image reconstruction [Surti et al., 2007].

2.2.1 Data Corrections

In practice, the PET data acquisition is not perfect and there are a few factors in the measurement data that need to be taken into account. These effects need to be corrected in order to acquire clinically useful images that can provide accurate quantitative information from PET studies. One of these source of error is *Compton scattering*, where a photon collides with another electron and changes direction. This may cause the LOR not to pass through the annihilation location and will cause

an erroneous LOR to be recorded (figure 2.3a). Correction for scatter is usually done using a single scatter simulation approach, which is based on Monte Carlo simulation of the path of scattered events [Watson et al., 1996].

Another source of error in PET data acquisition is the *random coincidences* (figure 2.3b), where two photons which are not originated from the same source are detected in the same timing window, causing an erroneous measurement of an LOR. These are usually corrected using a delayed coincidence timing window in which only random events can occur. Once measured, the mean of random counts are subtracted from each sinogram bin to obtain the 'randoms subtracted' data. *Dead time*, or pile-up effect, is the arrival of a new photon at a detector before the processing of the preceding photon is completed and can be another source of error in the obtained PET data. Correction for the *radioactive decay* of the radionuclide from the injection time is also need to be considered for accurate quantification of the PET data. Decay correction is performed by calculating the exponential decay of the tracer activity over the course of a scan and correcting the data acquired at a later time back to the original activity recorded at the beginning of the scan. Half-lives of some radionuclides used commonly in PET imaging are given in table 2.1.

Another major factor which needs to be considered is the attenuation effects, which causes a reduction in the number of coincidences detected along the LOR due to the dense tissue causing one or both photons to scatter or not to penetrate through to reach the detectors. Traditionally, attenuation correction is done using a transmission source, where the ratio of detected events originating from a rotating rod source is computed before and after the patient is placed in the scanner, allowing the total

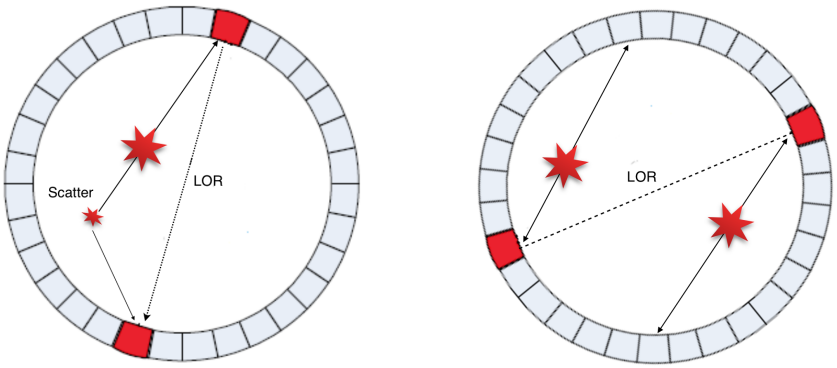

(a) Scatter coincidence

(b) Random coincidence

Figure 2.3: Detection of scattered and random coincidence events, causing an erroneous line of response.

attenuation along each LOR to be directly measured. However, as this approach requires an extra scan some alternative methods are introduced. For instance, an attenuation map can be computed from CT images in a combined PET/CT scanner which can be used to differentiate the attenuation media within the patient body on a voxel-by-voxel basis [Kinahan et al., 1998]. This is done by calculating attenuation coefficients of x-ray in tissue and converting that to suitable values for PET energy (511 keV) to produce the attenuation map. On the other hand, attenuation correction is still a major problem in PET/MRI scanners and various new methods have been recently introduced. Details about attenuation correction in PET/MR is discussed in section 2.4.

2.2.2 Partial Volume Correction

Due to the limited spatial resolution of PET scanners and sampling of an activity distribution into a finite voxel grid, PET images suffer from partial volume (PV) effects which can result in spill-over effects between neighbouring tissues. Even the

images from high resolution research PET scanners (HRRT) for human brain with a spatial resolution, 2.3-3.2 mm (FWHM) in the transaxial direction and 2.5-3.4 mm FWHM in the axial direction [Van Velden et al., 2008] suffer from PV effects and need to be corrected. A typical modern PET scanner has a spatial resolution of around 4.5 mm in the transaxial plane [Delso et al., 2011] [Levin et al., 2016]. This resolution and recontruction of images cause a greater blurring effect on the images. Spatial resolution of a PET scanner can be measured by acquiring images with a ^{22}Na point source, which is the NEMA standard located at different locations within the field of view. FWHMs on the line profiles through the voxel on reconstructed PET images are measured and regarded as the spatial resolution of the scanner [Delso et al., 2011].

Larger PV effects are seen when imaging smaller structures such as carotid arteries with a diameter of 4.5-6.5 mm [Krejza et al., 2006a] or grey matter of cerebral cortex with a thickness of 2-4 mm [Pakkenberg and Gundersen, 1997] and these structures look blurred on the PET images. The blurring effect which is the main cause of the PV effects can be described as the convolution of the activity within the object with the Point Spread Function (PSF) of the imaging system. PSF describes the response of the scanner to a point source and represents the degree of blurring applied to the reconstructed images [Soret et al., 2007] [Erlandsson et al., 2012a]. Due to the PV effects, reconstructed voxels will often contain contributions from neighbouring tissue types and will have spill-in effects from nearby high activity objects and spill-out effects to background regions with lower activities. This phenomenon is illustrated in figure 2.4.

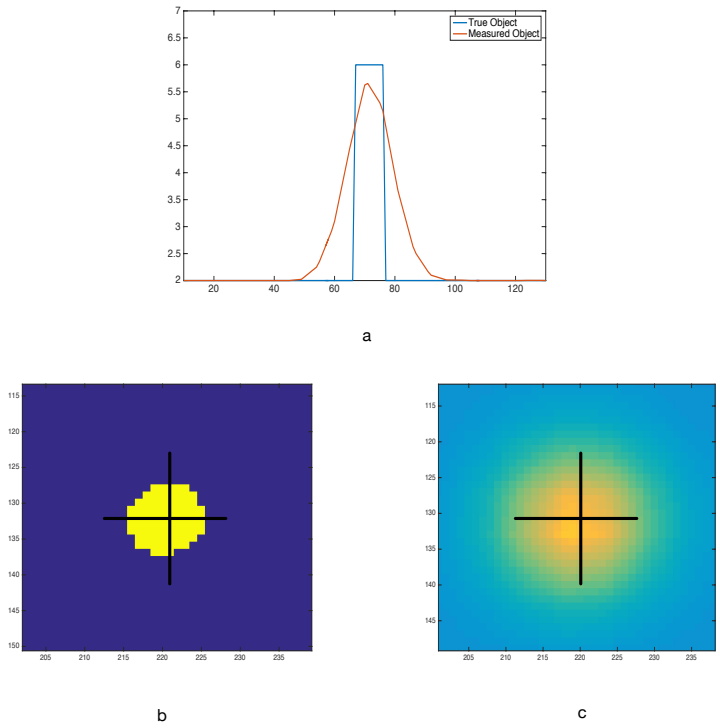

Figure 2.4: Line profiles of the true object and the measured object is shown in (a). Intensities within the object are lost due to spill-out effects to surrounding tissues. An axial slice of the true object (b) and the measured object with PV effects (c) are also illustrated

It is essential to correct for spill-in and spill-out effects before making any quantitative measurements on the reconstructed PET images. There have been multiple methods proposed to correct for PV effects and these can be applied both in sinogram or image space, during or after the reconstruction process. These methods can then be classified as region based or voxel based methods. Erlandsson et al. has presented a good review of the existing partial volume correction (PVC) methods [Erlandsson et al., 2012a]. Most of these methods use segmentation of various brain structures from anatomical MR or CT images of the subject. Knowledge of the anatomy can then be utilised in the PVC of the PET data. PV effects can be time dependent due to tracer kinetics and cardiac, respiratory or patient motions. There-

fore, each PET frame should be separately corrected, when analysing dynamic PET images.

Meltzer et al. [Meltzer et al., 1990] proposed their method which corrects for the spill-over effects between brain tissues including grey matter (GM) and white matter (WM) and non-brain regions including cerebral spinal fluid (CSF) regions. Assuming no uptake in non-brain tissues, the observed image was described as contributions from two compartments which are convolved with PSF. Müller-Gärtner [Müller-Gärtner et al., 1992] has extended this method to also correct for spill-out and spill-in effects between GM and WM regions. In this method, the brain MR image is segmented into GM, WM and CSF regions and the GM is corrected for PV effects. The method works by scaling the background regions to an estimate of their mean value, convolving it with the PSF and subtracting it from the observed PET image, correcting for the GM voxels. The Muller Gartner method provides a voxel-wise correction for the GM tissue

Rousset et al. proposed the Geometric Transfer Matrix (GTM) method [Rousset et al., 1998a] which performs region-based correction utilising anatomical MR data. In this method, the MR image is parcellated into a set of discrete ROIs where each region is assumed to contain a uniform activity which can accurately represented using its mean value. Each region is individually convolved with the PSF and contribution of each region to its neighbours is calculated by summing the voxel intensities which overlap true region a and blurred region b and dividing it to total number of voxels in region a. These contributions are used to construct a matrix known as the Geometric Transfer Matrix. Thus, GTM yields corrected re-

gional mean values of segmented regions. If the segmentation and coregistration errors are neglected, it can be said that using higher number of regions in GTM correction can improve the accuracy of the PVC. Yang et al. [Yang et al., 1996] presented their method where the brain is parcellated into multiple regions and each region is represented using their true relative mean value to a reference region. This image is convolved with the PSF to obtain the correction factors as the ratio of two images, before and after the convolution. The main limitation of Yang's method is its requirement for strong prior information about true relative activity distribution between the brain regions.

Erlandsson et al. reported a hybrid PVC method, named Multi-target correction (MTC) [Erlandsson et al., 2006]. Unlike GTM, MTC can provide a PV corrected image and can correct for multiple regions. This method uses GTM method to get PV-corrected mean values for various regions and then performs a voxel-based PV correction for these regions. Erlandsson et al. presented an alternative method called iterative Yang method, where the PVC was applied and regional mean values are estimated in an iterative fashion. New regional values were computed in each iteration and the correction was repeated [Erlandsson et al., 2006]. This method corrects for PV effects in voxel basis and does not rely on any prior information about the activity distribution between the regions. PVC can alternatively be performed using wavelet-based correction techniques [Boussion et al., 2006] [Shidahara et al., 2009]. These techniques involve transformation from image domain to wavelet domain to perform multiresolution analysis of the images [Turkheimer et al., 1999], which allows incorporation of anatomical infor-

mation into PET images.

2.3 Theory of Magnetic Resonance Imaging

Magnetic resonance imaging (MRI) was developed based on nuclear magnetic resonance (NMR), which is the phenomenon that in the presence of a magnetic field, nuclei of atomic particles absorb and re-emit electromagnetic radiation. Protons possess an intrinsic property referred to as spin which can be visualised as a form of precessional movement about an axis. As shown in figure 2.4, these spins are normally randomly aligned and in overall produce no net magnetic moment. When an external magnetic field, B_0, is presented, these spins align parallel or antiparallel to the field, forming two spin states known as *spin-up* and *spin-down*. This is also known as Zeeman splitting. As the spin-up state has lower energy, slightly more spins will align parallel to the external magnetic field than antiparallel, creating a net magnetic moment M_0. This magnetisation is in order of μT and is measurable by MR scanners.

Since the magnetisation also possesses an angular momentum, rotation around the axis of B_0 will be observed. The rate of this rotation, or precession, depends on the strength of the torque force caused by the magnetisation, which can be written as equation 2.1, also known as the Larmor equation

$$\omega = \gamma B_0 \tag{2.1}$$

where ω is the angular precessional frequency of the proton, also known as

Larmor frequency, γ is the gyromagnetic ratio, 42.58 MHz/T for protons, and B_0 is the strength of the external magnetic field. Using a larger field strength will increase the speed of precession.

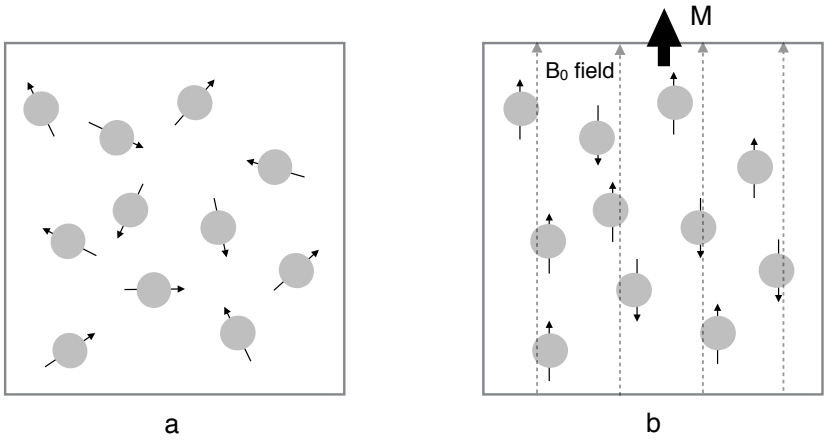

Figure 2.5: Alignment of spins in a magnetic field. (a) with no magnetic field, spins are randomly oriented with no net magnetic moment. (b) In an external field, B_0, spins will align parallel or anti-parallel to the field, with a net magnetic moment, M_0, parallel to the field.

The spins can be excited out of their alignment with a second magnetic field, denoted as B_1 orientated in a direction perpendicular to the B_0 field. The B_1 is also known as an RF pulse and it can be turned on and off. When its frequency matches the Larmor frequency, ω, 'resonance' occurs which causes M_0 to precess around B_1. In a rotating frame, the RF pulse causes the magnetisation to move away from the longitudinal direction by an angle α, also knows as the flip angle [McRobbie et al., 2006]. Applying a longer RF pulse will cause a bigger deflection of the net magnetic field, and hence will increase the angle α.

Once the RF pulse is turned off, the protons return to their equilibrium state in

a process known as relaxation. This causes the signal to decay exponentially and dephase as spins experience different magnetic field inhomogeneities and spin-spin interactions. The precession of the net magnetisation causes an oscillating field component in the transverse plane which induces a voltage in receiver coils appropriately placed relative to the field. This induced current gives rise to the observable MRI signal. The B_1 field can be generated by a coil similar to the one used for detection which means that depending area of the body to be imaged, a single coil, called volume coil, can be used for both excitation and detection purposes. However, it is common practice to use the transmitter coils in the body of the scanner for excitation and use local surface coils for receiving the MR signal. This is particularly the case in the hybrid PET/MR scanners where we need to minimise PET absorption by coils.

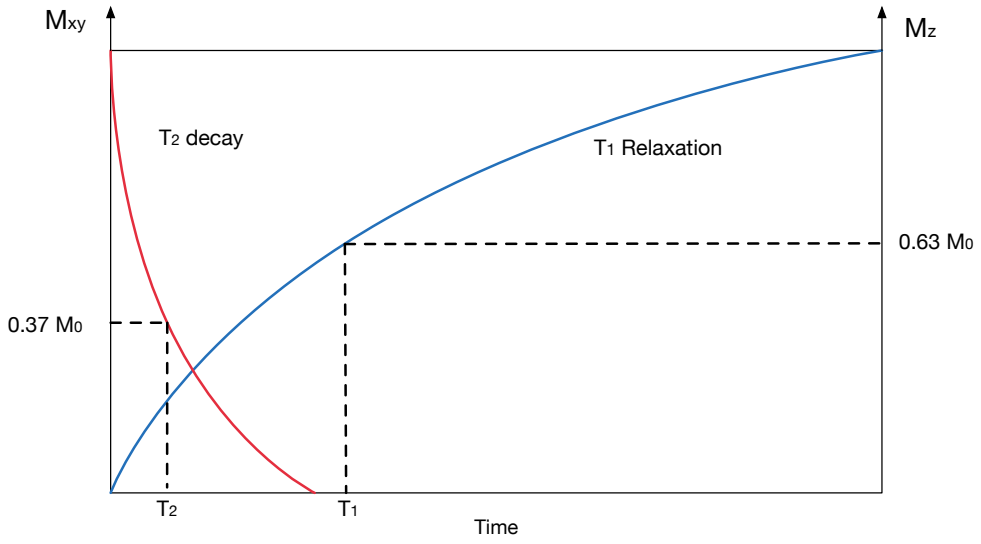

Figure 2.6: Illustration of T_1 recovery and T_2 relaxation curves which occur simultaneously. Reproduced from [McRobbie et al., 2006]

The relaxation which occurs once the RF pulse is turned off can be described

using two separate time constants: T_1 relaxation represents the rate which the magnetisation returns to alignment with the longitudinal axis following the application of an RF pulse, and T_2 relaxation, also known as spin-spin relaxation, represents the rate which coherence is lost between spins in the transverse plane. T_2 relaxation is an exponential decay process and T_2 is the time it takes for the magnetisation to drop to 37% of its original size. On the other hand, T_1 relaxation has an exponentially increasing shape, but is slower than T_2 relaxation. T_1 represents the time it takes for the magnetisation to reach to 63% of its final equilibrium value. T_1 relaxation depends on the field strength and can get slower as the field strength increases where T_2 is less dependent to the field strength. These are illustrated in figure 2.6.

In addition to T_2 decay, T_2^* relaxation occurs as a consequence of inhomogeneities in the main magnetic field, which can be caused by intrinsic defects in the magnet or susceptibility-induced field distortions produced by the tissue. Stable offsets in the main magnetic field across the imaging space cause different locations to slowly accrue phase relative to each other. It can also be expressed as equation 2.3 where T_{2inhom} represents the magnetic field inhomogeneities.

$$\frac{1}{T_2^*} = \frac{1}{T_2} + \frac{1}{T_{2inhom}} \tag{2.2}$$

Values of T_1 and T_2 depend on the property of tissues and the magnetic field strength. T_2 is always shorter than T_1 and different tissues and pathologies have different T_1 and T_2 values. In the brain, grey and white matter have distinct T_1

and T_2 values which makes it easier to separate them and CSF in the image space. Usually, most pathologies have longer T_1 and T_2 times, and appear darker on a T_1-weighted image and brighter on a T_2-weighted image [McRobbie et al., 2006]. T_1 usually varies between 300 to 2000 msec and T_2 usually varies between 30 and 150 msec [Schild, 1990].

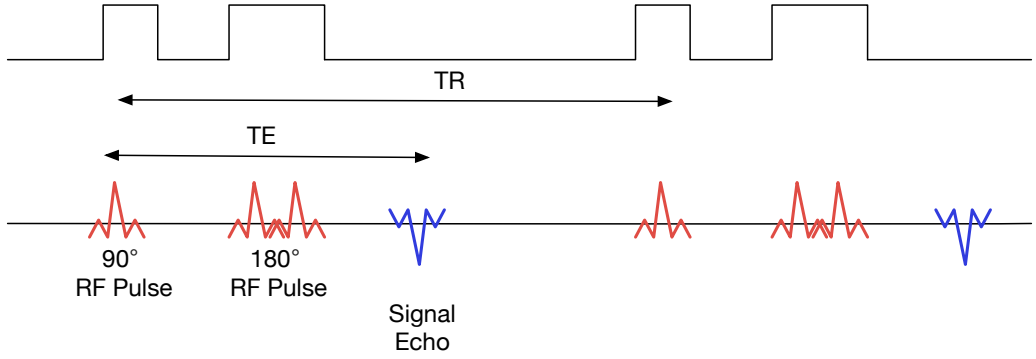

Figure 2.7: Illustration of a spin echo pulse sequence. A 90° RF pulse is followed by a 180° pulse to reverse the spins. TE is the time between the first pulse and the echo. TR is the time between repeated pulse sequences.

Signal echoes can be obtained using two different methods, gradient echo (GE) and spin echo (SE). In GE sequence, an RF excitation pulse, which is usually less than 90° is applied and is immediately followed by a negative magnetic gradient lobe. This initial lobe causes the spinning protons to dephase in transverse direction. Then a reversed positive gradient is applied which causes the spins to rephase and compensate for the dephasing caused by the negative gradient lobe. After a certain time, all the spins will come back into phase, generating a gradient echo.

In the SE method, as illustrated in figure 2.7 the spins are excited using a 90° pulse and left to their natural dephase caused by the external and internal magnetic field inhomogeneities. While the spins are dephasing, a 180° pulse is applied to

flip all the spins. However, these spins continue to dephase in the same direction as before since their precessional frequencies are not changed. All of the spins will come to rephase at a time equal to the delay between the 90° and 180° , also known as the echo time (TE), and will form a spin echo. Application of the 180° phase reversal will mean that the echo height will be governed by the T_2 relaxation constant.

2.4 Image Formation in MRI

In addition to B_0 and B_1, MRI scanners have 3 separate gradient coils, which create magnetic fields called gradients in x,y and z directions. This was introduced by Paul Lauterbur in 1973 [Lauterbur, 1973] and later expanded by Sir Peter Mansfield to develop echo planar imaging [Mansfield, 1977], variations of which are still utilised clinically. These fields create linear variations in the magnetic field in these three directions, and can be used to create spatial variation in the resonance frequency. This phenomenon can be mathematically expressed as:

$$B(r) = B_0 + G.r \tag{2.3}$$

where r is the 3 dimensional spatial location and G is the vector of gradient field strengths. G can be in any of the x,y, and z directions. Compared to the main magnetic field, gradient fields are quite small in strength (i.e 40 mT/m compared to 3 T main field) [Bushong and Clarke, 2013]. For example, the gradient coils can be used to apply a gradient in the z direction, which allow for choosing the slice to be excited. In this case, the thickness of the slice will be determined by the gradient

strength G and the bandwidth ($\Delta\omega$) of the applied RF pulse. The central frequency of the RF pulse will dictate the slice position hence multiple slices can be selected by choosing different frequency RF pulses.

As can be seen equation 2.3, the frequency ω depends on position in the presence of a gradient. The gradients can be controlled to alter the precessional frequency and phase depending on the position. The received MR signal is in Fourier space and is stored in a 'raw-data' container named k-space. K-space contains the frequency encoded and phase encoded data of the MR signal recorded from each anatomical point of the object during MR acquisition.

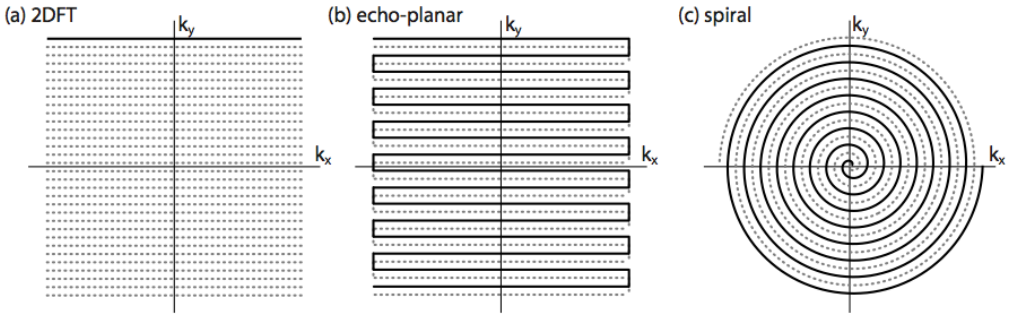

Figure 2.8: Three of the most common k-space trajectories: (a) 2DFT, (b) multi shot echo-planar imaging (EPI) and (c) spiral. The portion of k-space collected during a single repetition period is shown by a black, solid line, and subsequent readouts are shown as grey, dashed line. Taken from [Miller, 2004]

K-space can be measured following a single RF pulse or a number of RF excitations. An MR pulse sequence is used to capture one line of kspace and can be repeated with a repetition time (TR) with various phase encode gradient values to capture the desired space. Multiple encoding trajectories can be used to fill the k-space, where the most common ones include 2DFT trajectory, echo-planar (EPI) trajectory [Mansfield, 1977] and spiral imaging [Meyer et al., 1992]. These encod-

ing techniques are illustrated in figure 2.8. While 2DFT encoding is a multi-shot imaging techniques where k-space is filled in multiple readouts, EPI can be used to fill k-space at once and hence is a single-shot imaging technique, which makes it useful in imaging functional studies or objects with significant motion. Spiral encoding can be used both as single shot or multi-shot. Once the k-space is filled, inverse discrete Fourier transform of k-space is computed to reconstruct the image in a least squares sense.

2.4.1 Structural MR pulse sequences -MPRAGE

In MRI, several anatomical pulse sequences can be used to obtain MR images with high spatial resolution in a short acquisition times. One main branch of these are the Gradient echo (GE) sequences. First proposed by Muger and Brookeman [Mugler and Brookeman, 1990], The three-dimension magnetisation-prepared rapid gradient echo (MPRAGE) sequence [Gillan et al., 1992] is one of the common sequence to obtain a good-resolution T1 weighted images of the whole brain. This sequence can be used to provide excellent tissue contrasts with full brain coverage in short scan times. It is the equivalent of the Gradient Recalled Acquisition at Steady State (GRASS) sequence present in GE Healthcare MRI systems or Turbo field echo sequence in Philips MRI scanners [Nitz, 1999] [Chavhan et al., 2008]. These sequences specifically have short TR to make image acquisition less time consuming. Unlike the spin echo sequence, no 180° pulse is applied as it increases the acquisition times. Instead, a magnetic field gradient is superimposed on the existing magnetic field for a short time to induce large magnetic field inhomogeneities

which causes the spins to dephase faster [Schild, 1990]. The magnetic gradients are applied in opposite directions repetitively to induce a rephasing effect similar to the effect caused by the 180° RF pulse in spin echo sequences. After rephasing of spins, a gradient echo signal is received.

In MPRAGE pulse sequence, the sequence starts with a 180° inversion pulse to enhance the contrast between the grey matter to white matter. After the inversion time (TI), which is the waiting time after the inversion pulse (between 200-1000msec), RF spoiling with a small flip angle and gradient encoding steps are executed [Gillan et al., 1992]. In these fast imaging sequences, it is essential to use RF pulses which cause a low flip angle(α). With the help of these small flip angles, the longitudinal magnetisation is always kept at a certain value which is tilted with the next RF pulse. This enables the receivers to get a reasonable signal even if the next pulse comes after a very short TR [Schild, 1990]. MPRAGE images are commonly acquired in our centre as they are a practical way of obtaining MR images of the brain with a high spatial resolution (around 1 x 1 x 1 mm voxel size) in a short acquisition time (around 5 minutes).

2.4.2 Vascular MR pulse sequences

Time-of-flight MR Angiography (TOF-MRA) is a MR imaging sequence which is mainly used to produce images of the blood vessels without any need for external contrast agents. It utilises the inherent flow sensitivity of the MR signal to visualise blood flow within the vessels [Saloner, 1995]. Moving spins within the blood causes a great influence on the MR signal and can cause artefacts in MR images (i.e.

bright arteries with high T_1) as the Fourier transform of kspace assumes that signal from each voxel does not change between measurements. TOF-MRA sequences turns this phenomenon to their advantages by increasing the signal coming from the blood. They utilise a gradient echo sequence with a short TR and TE. The short TR and TE saturates the signal coming from the stationary spins, or tissues while the unsaturated spins flowing into the imaging slice generate the majority of the MR signal. The maximum MR signal is received when the blood can completely transport itself across the imaging volume within a single TR [McRobbie et al., 2006].

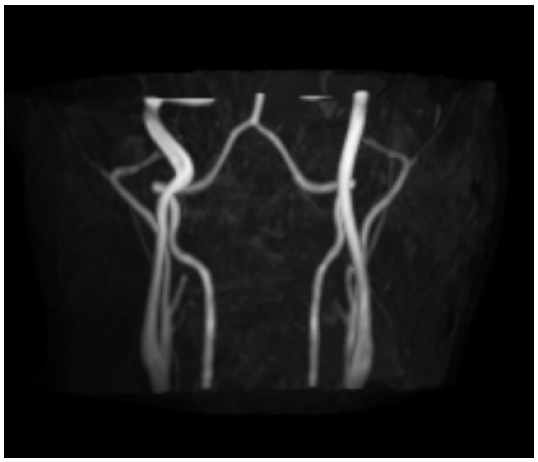

Figure 2.9: Maximum intensity projection (MIP) of the carotid arteries acquired using a 3D TOF-MRA sequence

The TOF-MRA sequence is applied perpendicularly to the direction of the blood flow in order to maximise the blood signal. MRA may not work well if a thick slice is used in the acquisition as slow flowing blood may be detected as stagnant. Image reconstruction can be done in 3D to get 3D TOF-MRA images. These images can be used to generate maximum intensity projections (MIPs), which show the maximum pixel value in three dimensions. These images can be used to vi-

sualise even very small blood vessels with high contrast. A MIP projection of an example 3D TOF-MRA image is shown in figure 2.9.

2.4.3 Dynamic MR pulse sequences

Dynamic MR acquisitions can be performed using MR sequences with high temporal resolution to perform quantitative measurements over MRI data. Dynamic MR sequences are usually used with injection of Gadolinium (Gd) based contrast agents which cause a reduction in T_1 and T_2 relaxation times. They are usually found in the form of chelates as Gd itself is a toxic in its elemental form. They are administered to the subject through their veins using a concentration of 0.1 mmol/kg for an adequate signal enhancement [Geraldes and Laurent, 2009]. Due to the reduction in relaxation constants, Gd-based contrast agents causes a brighter region in T_1 weighted images but a darker region in T_2 weighted images. MR contrast agents can be used with dynamic sequences, which can allow one to perform quantitative measurements, such as blood flow and perfusion measurements on dynamic data. Since the bolus travels with a high speed after the injection, having a high temporal resolution is essential to capture the most information with these sequences. Two different generic approaches can be used to acquire dynamic MR data with contrast agents. Dynamic Contrast Enhanced MRI (DCE-MRI) is a technique based on T_1 weighted image acquisitions whereas dynamic susceptibility contrast enhanced MRI (DSC-MRI) uses T_2 or T_2* weighted images. Common sequences used for these two main dynamic MRI techniques are briefly summarised in the next subsections. Choosing a suitable MR sequence depends on the desired dynamic measurement type, image

quality, the desired field of view, spatial and temporal resolution. Further information regarding the interpretation of DCE-MRI and DSC-MRI and their kinetic modelling is included in chapter 3.

2.4.3.1 DCE-MRI

Gradient echo based sequences are mostly used in DCE-MRI acquisitions. The standard fast GE sequences such as FLASH, turbo FLASH, spoiled gradient-recalled echo (SPRG), volumetric interpolated breath-hold (VIBE), etc., can be used in a repetitive setting to acquire dynamic images [Essig et al., 2013]. In 3D acquisitions, the high amount of spatial coverage might cause reductions in the temporal resolution, and require a modern scanner with a good gradient system.

Before starting the dynamic acquisition, pre-contrast agent images with variable flip angles are obtained in order to be used for T_1 mapping. The information from T_1 mapping is later used to convert the MR signal to actual Gd concentrations. This is further described in Chapter 3. During the acquisition of pre-contrast images, the TR and TE are kept as constants and only the flip angle is changed. The number of used flip angles can vary from 2 to 7 [Cheng et al., 2006] [Committee, 2012]. As an alternative to the variable flip angle technique, optimised Look Locker pulse sequences can be used to obtain data for T_1 mapping [Freeman et al., 1998] [Henderson et al., 1999].

DCE-MRI acquisitions usually lasts around 5 to 7 minutes after the injection since the Gd-chelates have fast washout characteristics. For the DCE-MRI pulse sequences, short TE (ideally TE$<$1.5ms) and short TR (ideally TR$<$3ms) are used.

High temporal resolution, 3 seconds or less, is recommended if the blood signal is to be captured for arterial input function (AIF) measurements. A flip angle ranging between 25° and 35° are used in order to minimise saturation effects [Committee, 2012]. The number of slices can be increased with a cost of losing temporal resolution while increasing the coverage with a good spatial resolution. On the other hand, the slices thickness can be increased with less slices to improve the temporal resolution with the same FOV with poorer spatial resolution. Therefore, it is important to maintain the balance between the required spatial resolution, FOV and temporal resolution.

2.4.3.2 DSC-MRI

Dynamic susceptibility contrast enhanced MRI (DSC-MRI) is mainly used in brain perfusion studies for blood flow and blood volume measurements [Rempp et al., 1994] [Kennan and Jäger, 2003]. Similar to DCE-MRI measurements, it requires rapid pulse sequences to be able to make serial measurements of the signal loss during the passage of the bolus through the tissue. It utilises the effect of Gd contrast agent on the T_2 or T_2* of the brain tissue as the contrast agent travels through the brain. Spin-echo pulse sequences can be used to obtain T_2 weighted measurements where gradient echo pulse sequences are used to obtain T_2* weighted measurements [Kennan and Jäger, 2003]. Typically, injection of a double dose Gd contrast agent (0.2 mmol/kg) is required when SE pulse sequences are used whereas a single dose (0.1 mmol/kg) is sufficient with GE-based pulse sequences [Jahng et al., 2014] [Essig et al., 2013].

Paramagnetic Gd contrast agents induce a change in the average bulk susceptibility of tissues which can be detected by MRI scanners. After the rapid bolus injection (3-5 mL/sec), the contrast agent gets compartmentalised within the vessels due to the presence of the blood-brain barrier, disturbing the local magnetic field. This affects the magnetic field in the surrounding tissues which start to dephase, causing a loss in the T_2 and T_2* signals.

In order to characterise the first pass of the bolus in fast flowing blood, temporal resolution of at least 1.5 second is recommended. Due to the high temporal resolution required, DSC-MRI images usually have smaller FOV compared to anatomical MRI or DCE-MRI scans. In our centre, T_2* weighted GE-EPI pulse sequences are commonly used for DSC-MRI acquisitions. As shown in figure 2.8 GE-EPI allows the filling of multiple k-space lines using a single shot GE pulse and is very sensitive to the susceptibility effects as the signal drop is relatively larger compared to SE-based sequences. In a 3T MRI system, TE is chosen to be in range of 25 to 40 ms and TR between 1500-2000 ms, where flip angle is varied between 60° and 90° [Haaga, John R. Lanzieri and C., 2004] [Jahng et al., 2014]. DSC-MRI acquisitions usually last around 2-3 minutes only.

2.5 The Physical Basis of PET/MRI

Combination of PET and MRI scanners has been a major research topic for decades due to the excellent tissue contrast of the MR images and to eliminate the extra radiation caused by CT scans in PET/CT scanners. It can be argued that MR can outperform CT when anatomic information from soft-tissues and organs is required.

In addition, functional MR imaging techniques can be simultaneously acquired with a hybrid PET/MR scanner, which can provide complementary information to PET data and enhance the overall quantitative imaging performance.

One of the major technical challenges which was stopping the advent of combined PET/MR scanners was the electro-magnetic interaction due to the high MR magnetic fields. Photomultiplier tubes of the PET detectors are very sensitive to magnetic fields and need to be properly shielded to prevent the interferences from the MR system. The traditional PET detectors and their associated electronics contain conducting and radiofrequency emitting components, which can interfere with the MRI system. In addition, the presence of the magnetic field prohibits using ferromagnetic components in the PET/MR scanner. The constrained space within the MR bore where the PET system can be placed had also needed to be considered. Different vendors applied different design choices to overcome these problems and to combine PET and MRI scanners, as briefly discussed in this section.

Philips and General Electric initially chose to develop sequential PET/MR scanners, where PET and MR images are obtained sequentially, rather than simultaneously, similar to existing PET/CT scanners. One such system is the Philips Ingenuity TF PET/MRI scanner, a hybrid scanner with Philips time-of-flight GEMINI TF PET and Achieva 3T MRI system. In this system, the PET and MRI gantries are co-planar and can be placed in the same scanning room, sharing the same bed. After one scan is completed, the patients slides into the other scanner. GE's initial solution was also a sequential system where the PET and MR scanners were placed in different scanning rooms. After one scan, the patient is moved to the other room

to have the next scan, and a post-processing program is used to align PET and MRI images.

Siemens designed the first simultaneous whole-body PET/MRI system called Biograph mMR, which made simultaneous scanning possible. Their design was similar to concept proposed by Shao et al. in 1997 [Shao et al., 1997] used for BrainPET insert. The Biograph mMR fully integrates the PET and MR modalities into a single imaging system and allows simultaneous acquisition of PET and MRI images without compromising on image quality. As shown in figure 2.11, a ring of PET detectors is placed inside the bore of the MRI scanner, between the gradient coils and the RF coil.

In order to overcome electromagnetic interference and enable integration of PET and MRI, Siemens replaced the photomultiplier tubes used in the scintillation crystal blocks of established PET and PET/CT systems with a combined Lutetium Oxyorthosilicate (LSO) crystals and Avalanche Photo Diodes (APD) for optimised readout, components that are not susceptible to magnetic fields (Figure 2.10). A combination of LSO crystals and APD was able to detect positron annihilation events even inside strong magnetic fields.

Another advantage of using photo diodes is their small size compared to photo-multiplier tubes. As MRI already has a small bore size, there is only a limited space to place the PET detectors. 56 of these detector blocks are placed circumferentially to form one detector ring. The full PET detector unit contains 8 of these rings and spans a longitudinal field-of-view of 25.8 cm.

A few years after the introduction of the Siemens Biography mMR scanner, GE

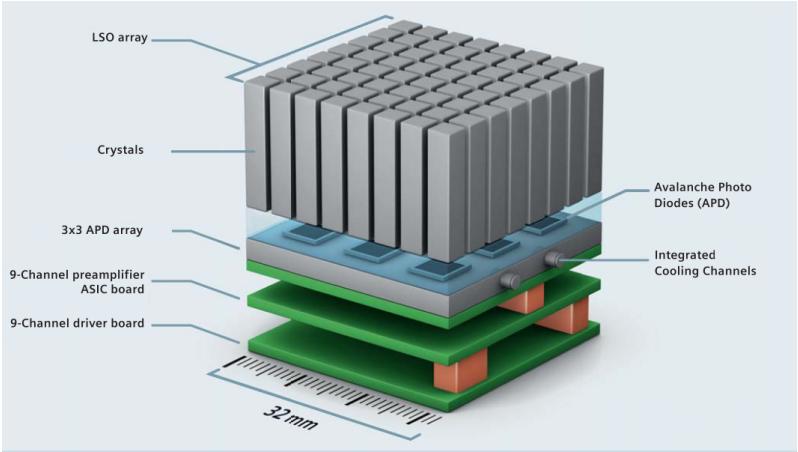

Figure 2.10: PET detector assembly for mMR with 64 Lutetium Oxyorthosilicate crystals. Courtesy of Siemens Healthcare.

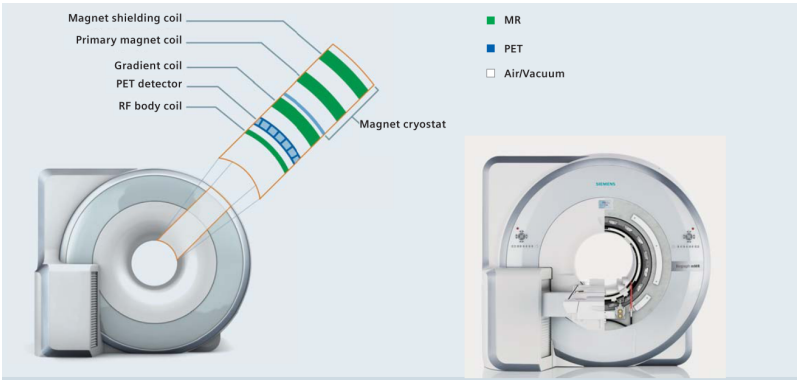

Figure 2.11: Siemens Biograph mMR scanner and its schematic representation showing the placement of the PET detectors inside the MR system. Courtesy of Siemens Healthcare.

Healthcare introduced their combined PET/MR system, called SIGNA PET/MR. Their system also had a PET ring integrated into a 3T MR system resulting in a patient bore opening of 60 cm, with a 25 cm axial FOV. GE used lutetium based scintillators with silicon photomultipliers (SiPM) for their PET detectors. Using these detectors, GE utilised time of flight PET technology in the SIGNA PET/MR scanner, making it the only TOF PET/MR system available [Levin et al., 2016]. This design offers fast coincidence timing resolution (less than 400ps) making it suitable for TOF PET. It is currently the only commercially available simultaneous TOF-

PET/MR system and initial results show no loss in image quality in reconstructed PET and MR images compared to images from PET/CT and standalone MR systems [Iagaru et al., 2015] [Levin et al., 2014].

2.6 Coregistration of PET/MR data

Even when a simultaneous PET/MRI scanner is used in image acquisition, PET and MRI data needs to be geometrically coaligned before any PET/MR image analysis is performed. This process is called image registration and is performed to bring intra-modality or inter-modality images, which can be acquired at different times or different scanners, aligned in the same image space. In PET/MR imaging, this allows the reader to obtain functional and anatomical information at the same time.

There are two approaches to perform image registration, extrinsic registration methods which rely on external markers which are placed on the subject and are detectable by the scanner, or intrinsic registration methods which are purely based on the image data. Extrinsic methods are usually avoided due to their invasiveness and complications. On the other hand, it is very hard to validate registration performance in intrinsic registration as the ground truth usually does not exist. In this work, intrinsic image registration was performed only.

During the registration of two images, the best transformation to spatially align one image to another needs to be computed. The types of transformations which are commonly used in medical imaging can be classified as: rigid, affine and non rigid transformations. Rigid transformations involves translation and rotation of the target image to match the reference image. Rigid registration has 6 parameters in total:

3 parameters to represent the translation on each axis and 3 parameters to represent rotation around each axis. In affine transformation, there are 12 parameters in total as it additionally applies scaling and shearing on the target image. Rigid and affine registration methods apply a global transformation to the target image. On the other hand, local warping can also be applied in non-rigid registration, which makes it a more complex method than the others. Non-rigid transformations can be parametrically defined using statistical shape models [Cootes et al., 2004], B-spline shapes [Rueckert et al., 2006] [Modat et al., 2010], and discrete cosine transformations [Ashburner and Friston, 1999].

During the image registration, a cost function is defined and used within an optimisation scheme to find the best similarity between the target and reference images. Various cost functions can be used for different image registration applications. The sum of squared differences (SSD) or cross-correlation are often used when the source and reference images are acquired using the same modality. These cost functions assume that both images have correlated image intensities, which is usually a valid assumption in intra-modality images. For inter-modality images, cost functions based on statistical dependencies are often chosen, such as Mutual Information (MI), Normalised Mutual Information (NMI), and Normalised Cross Correlation (NCC) [Maintz and Viergever, 1998] [Oliveira and Tavares, 2014].

In this work, FMRIB's Linear Image Registration Tool (FLIRT) (University of Oxford, UK) [Jenkinson and Smith, 2001a] [Jenkinson et al., 2002] was used for registration of PET and MRI data. This software can be used to perform translation only, rigid and affine transformations using the cost functions listed in the previous

paragraph. This package can be downloadeded as part of the FSL (FMRIB Software Library) software package [Woolrich et al., 2009] [Jenkinson et al., 2012].

2.7 Attenuation Correction in PET/MR scanners

Due to the lack of transmission data in PET/MR scanners, methods to derive the attenuation map from MRI data need to be developed to perform attenuation correction on PET data. However, as the MR data mainly reflect the proton density of tissues, photon attenuation information cannot be directly derived from MR images [Izquierdo-Garcia et al., 2014]. In addition, the RF coils present between the subject and the detector also cause additional attenuation, which may require a separate correction [Wagenknecht et al., 2013]. Therefore, performing an accurate attenuation correction in PET/MR scanners is a challenge and a number of methods have been proposed. These methods can be classified into two categories: segmentation-based methods and atlas-based methods.

The segmentation-based techniques parcellate the MR image into different tissue classes and assign an attenuation coefficient to approximate the attenuation characteristics of each tissue class. These methods assume that the attenuation coefficients of soft tissue at 511keV are constant and therefore a predetermined attenuation coefficient can be used [Wagenknecht et al., 2013]. In PET/MRI imaging, the DIXON sequence [Coombs et al., 1997] can be used to produce gradient echo fat only and water only MR images by adjusting the echo time (TE). These images then can be used to divide the body image into separate tissue classes such as air, lung, soft tissue and fat. Then, attenuation factors are assigned for each

class [Martinez-Möller et al., 2009]. Ultrashort echo time (UTE) or zero echo time (ZTE) sequences can also be applied to get additional bone information to use in the segmentation [Izquierdo-Garcia et al., 2014] [Arabi et al., 2015]. These sequences are used in brain studies to obtain three-class attenuation maps including air, soft tissue and bones [Catana et al., 2010] [Keereman et al., 2010]. An axial slice of an example UTE image is shown in figure 2.12a. Berker et al. proposed an attenuation correction method which uses combination of UTE and Dixon sequences for bone and fat detection with a four class PET attenuation map [Berker et al., 2012]. Results showed that this method can be used to obtain visually similar attenuation maps compared to those derived from CT images, with a high voxelwise agreement. However these studies concluded that the accuracy of these methods heavily depends on the segmentation of the bones, which can be negatively affected due to susceptibility effects especially at bone/air and soft-tissue air interfaces [Mehranian et al., 2016]. Different tissue types may produce similar signal intensities which can be another threat to the performance of the segmentation-based attenuation correction methods. In addition, these methods do not provide any correction for the additional attenuation effect caused by the MR components.

Atlas based methods use a number of atlases or templates where the subject's MR images can be registered to and converted to pseudo-CT images using a CT atlas [Hofmann et al., 2008] [Burgos et al., 2014] [Sekine et al., 2016] [Wollenweber et al., 2012] [Izquierdo-Garcia et al., 2014]. Brain templates are generated by taking the mean of the the attenuation maps to reflect population based attenuation coefficients. These methods are susceptible to registration errors and inter-subject

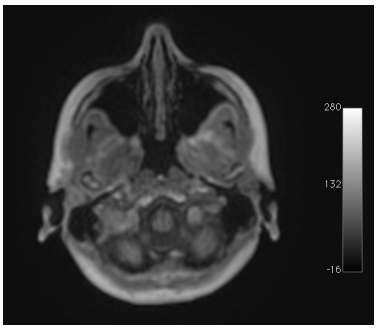

(a) UTE

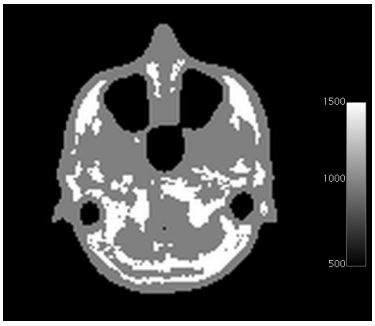

(b) UTE μmap

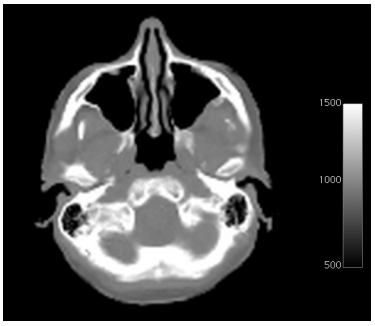

(c) pCT μmap

Figure 2.12: Axial slice of a brain image acquired using a UTE sequence (a) is shown with attenuation maps derived using the UTE image (b) and derived from a pseudo CT image based on an atlas-based method [Burgos et al., 2014]

anatomical variability. A large image database can be used to account for inter-subject variability and multiple atlas registrations can be used to minimise registration errors [Hofmann et al., 2008] [Burgos et al., 2015] [Sekine et al., 2016]. Then each voxel in the MR image is substituted by a CT value using image similarity measurements. Results from multi-atlas methods were shown to be more accurate than single atlas methods and yielded more similar results to gold standard CT based attenuation maps. Attenuation maps derived using an atlas based method [Burgos et al., 2015] and a UTE image are shown in figure 2.12b and 2.12c. These images show that some unsubtle differences can be seen in μ maps derived using UTE based or atlas based techniques.

Chapter 3

Quantitative Analysis of PET and MRI data

3.1 PET

3.1.1 Quantification in PET

In typical static PET scans, the radioactive PET tracer is usually administered to the subject outside the scanning room and there is a waiting period of 20 minutes to 1 hour, until the tracer uptake reaches equilibrium in the tissue of interest. After this waiting period, the patient is placed inside the PET scanner and data acquisition is performed for around 20 minutes. Static imaging techniques are usually used to obtain one late-scan PET image where the metabolic assessment can be approximated and relative tracer uptake of the target tissue can be obtained. An exciting property of PET scanners is that the acquired data can be truly quantitative. After necessary calibrations, the signal recorded by a PET scanner gives absolute tracer concentration measured in Becquerels per millilitre (Bq/mL). The relative tracer

uptake is often characterised using the standardised uptake value (SUV), a metric commonly used to quantitatively interpret PET images in a clinical setting. To calculate SUV, the radiotracer uptake is corrected for the amount of injected activity and the distribution volume within the patient. Typically patient body weight is used to represent the distribution volume. SUV can be calculated using the equation 3.1. This equation can be modified to replace the body weight with lean body mass (LBM) [Tahari et al., 2014] or body surface area [Kim et al., 1994]. Even though SUVs can only approximate the metabolic processes within the body, they are a simple way of obtaining quantitative information from PET imaging without getting into the complications of dynamic PET imaging techniques such as arterial blood sampling.

$$SUV = \frac{C_{PET}}{\text{Dose}/\text{Weight}} \tag{3.1}$$

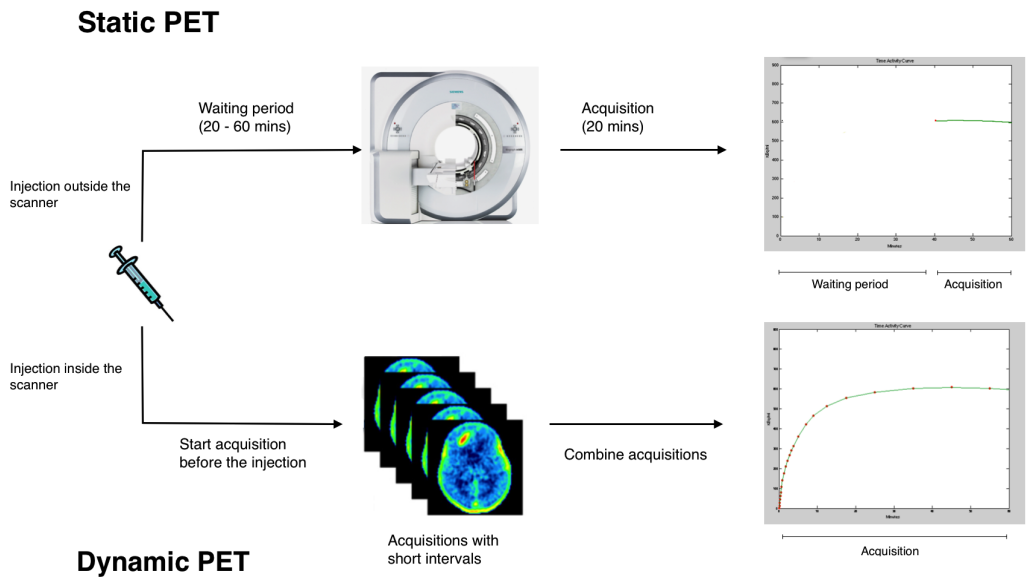

Figure 3.1: A representation of main differences in static and dynamic PET imaging.

The PET signal can also be measured from the time of tracer administration until the end of the scan, with very short intervals of time, allowing us to track the behaviour of the tracer over the time course of the scan. This is defined as dynamic imaging and an illustration of the differences between static and dynamic PET is shown in figure3.1. Dynamic imaging can provide some benefits over static imaging as the process of tracer uptake, retention and washout can be assessed in more detail. Furthermore, using dynamic imaging can reduce the bias which might be present in static images due to the chosen time of data acquisition. In order to analyse the dynamic behaviour of the PET tracer upon injection, kinetic analysis methods are used.

3.1.2 Principles of PET tracer kinetics

Dynamic PET data can be analysed using kinetic models to obtain quantitative information about dynamic processes in the tissue of interest. This can be done by defining the time varying systems by using compartments in which the tracer is assumed to be distributed homogeneously. The PET tracer can exchange between these compartments and these exchanges are defined using ordinary differential equations (ODEs). These ODEs are then solved to obtain values for the rate constants which represent the transport of tracer from one compartment to another. To simplify compartmental modelling, linear regression methods or graphical analysis techniques can be used to quantify acquired PET time series. Introduction to these techniques are given in this section.

Based on the Fick principle, Kety and Schmidt described a blood flow model

[Kety and Schmidt, 1945], which states that the rate of change of the tracer concentration in tissue is proportional to the blood flow (F) and the difference between the concentrations entering and exiting the tissue of interest, as shown in equation 3.2:

$$\frac{dC_T}{dt}(t) = F(C_a(t) - C_v(t)) \tag{3.2}$$

where C_T, C_a and C_v are the tracer concentrations in tissue, arterial and venous blood respectively. For rapidly diffusible PET tracers (e.g ^{15}O-water), the tissue concentration equilibrates with the venous outflow and these concentrations are related by the volume of distribution V_T, by $V_T = C_T/C_v$. Hence, the equation 3.2 can be rewritten as:

$$\frac{dC_T}{dt}(t) = F(C_a - (C_T/V_T)) \tag{3.3}$$

The volume of distribution can be described as the volume of tissue that should contain the same concentration as in blood relative to total tissue volume. This equation can be solved for C_T using Laplace transform as:

$$C_T(t) = FC_a(t) \otimes e^{(-\frac{F}{V_T}t)} \tag{3.4}$$

However the Kety-Schmidt model is only valid for tracers which are fully extracted from blood to tissue. For other traces, only a fraction of tracer is extracted into the tissue through capillaries and the rest transfers directly into the veins. For such tracers, the extraction fraction, which is the amount of trapped tracer in the first pass to the amount delivered, has to be considered. Renkin and Crone [Renkin,

1959] [Crone, 1965] calculated the extraction fraction E using the following equation:

$$E = 1 - e^{(-PS/F)} \tag{3.5}$$

where PS is the permeability surface area product (mL/min/mL), which is the multiplication of total available capillary surface area and the permeability of the PET tracer. These relationships can be used to construct compartmental systems.

Alternatively, kinetic analysis of dynamic PET data can be performed using spectral analysis [Cunningham and Jones, 1993] which was introduced by Cunningham and Jones in 1993. Spectral analysis is a more generalised technique and does not require any priori assumptions regarding the number of compartments required to analyse that specific tracer. In this technique, the tissue TAC is modelled using sum of single exponentials, which represent the impulse response of the tissue, convolved with the AIF. The tissue TAC is fitted using this model and a non-negative linear least squares estimation to produce estimates of macroparameters such as V_T. Spectral analysis can also be used to estimate the number of compartments required to perform compartmental model analysis of a specific tracer.

3.1.3 Compartmental Model Analysis

Compartmental models can be used to describe the behaviour of the tracer measured using dynamic PET studies, where each compartment reflects a different anatomical, physiological or biochemical stage. Each compartment is characterised by the concentration of the tracer within it as a function of time. When compartmental

models are used to define a system, it is assumed that tracer is uniformly distributed in each compartment and no concentration difference is present inside each compartments. Sets of ordinary differential equations can be written to represent the tracer concentration entering and exiting each compartment. These equations are then solved to obtain the quantitative values of interest.

Figure 3.2 illustrates the process of representing a region of interest in a brain using compartmental models. The black circles on 3.2b represents the radioactive tracer molecules as they are seen in the blood and some of them in the extravascular extracellular space. Assuming that there are receptors in the brain specific to the tracer used, some of the tracer is bound to these receptors. This information can be used to construct a compartmental model by identifying the primary states of the tracer and the transfers between these states. Ordinary differential equations can be written to describe the rate of change in tracer concentration in each compartment.

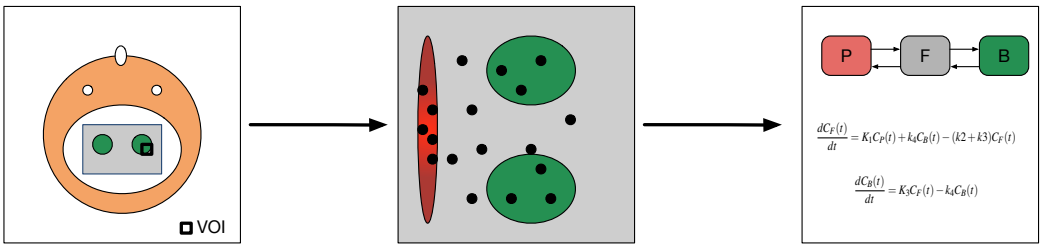

Figure 3.2: Schematic of the compartmental modelling process as applied to PET images. (a) A region of interest is identified on the PET image, (b) the contents of the region and the possible states of the tracer in the region is conceptualised, (c) the ligand states are represented using compartments and mass balances on each compartment is written by ordinary differential equations. Adapted from [E.D. Morris, 2004]

The simplest model used in PET is the one-compartmental model, which is most commonly used to describe blood flow measurement by ^{15}O-water but can

also be used to describe kinetics of some radioglands. As can be seen in figure 3.3a, this model shows the bidirectional flux of tracer between blood and tissue. The net tracer flux into tissue is expressed using the equation 3.6, where $C_T(t)$ is the time-varying tracer concentration in tissue, $C_P(t)$ is the concentration of the tracer in the plasma and K_1, k_2 are the two first-order kinetic rate constants, representing the transfer from arterial blood plasma to tissue and tissue to blood respectively. It can be seen that equation 3.3 and 3.6 are similar, where $K_1 = FE$ and $k_2 = K_1/V_T$. The assumption made is that the tracer is homogeneously distributed within each compartment (blood and tissue in this case).

$$\frac{dC_T(t)}{dt} = K_1 C_P(t) - k_2 C_T(t) \tag{3.6}$$

Equation 3.6 can be solved for $C_T(t)$ using Laplace transform, giving:

$$C_T(t) = K_1 e^{-k_2 t} \otimes C_p(t) = K_1 \int_0^t C_P(\tau) e^{-k_2(\tau - t)} d\tau \tag{3.7}$$

The 1 tissue compartmental model can be expanded to a 2 tissue compartmental model, as shown in figure 3.3b, where the PET tracer has three states: tracer in plasma, free tracer in tissue and tracer bound to the tissue of interest. ^{18}F-FDG is commonly analysed using 2 tissue compartmental model, where the ^{18}F-FDG gets trapped and phosphorylated in the second compartment. Concentration of the tracer in plasma is regarded as the input to the system. C_F represents the extravascular pool of the tracer within the tissue, where the tissue is free and available for binding. The other compartment C_B tells us about the concentration of the tracer which

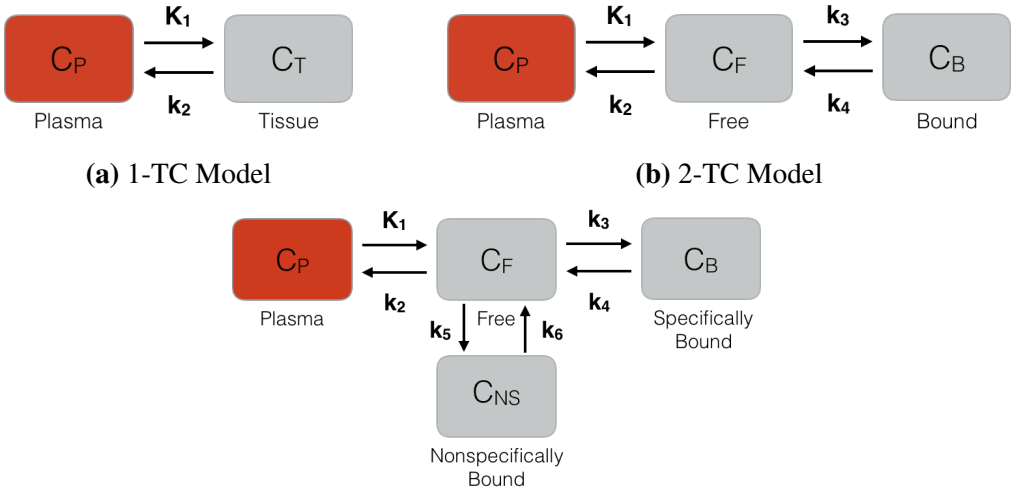

(a) 1-TC Model **(b)** 2-TC Model

(c) 3-TC Model

Figure 3.3: Schematic diagram of tissue compartmental models. (a) One-compartmental model with two rate constants, (b) two-compartmental model with four rate constants, (c) three-compartmental model with six rate constants

is specifically bound to the molecule of interest, or phosphorylated for the case of FDG. The two-compartmental model can be described by two ODEs, shown in equations 3.8 and 3.9. It should be stated that this model is a reversible model as the metabolised tracer can go back to free state. For ^{18}F-FDG , k_4 can be approximated to 0, meaning that the trapped FDG gets trapped in the second tissue compartment. Such tracers are analysed using irreversible models.

$$\frac{dC_F(t)}{dt} = K_1 C_P(t) + k_4 C_B(t) - (k_2 + k_3) C_F(t) \tag{3.8}$$

$$\frac{dC_B(t)}{dt} = K_3 C_F(t) - k_4 C_B(t) \tag{3.9}$$

In some cases, using a two-compartmental model can be inadequate to describe the behaviour of the tracer and a third tissue compartment is introduced. This

model is called three tissue compartmental model and is shown in figure 3.3c. The extra compartment is often called non-specifically bound compartment, C_{NS}. The main difference between the bound and nonspecific bound states is that non-specific binding is not saturable and not displaceable. The three-compartmental model can be described by the following equations:

$$\frac{dC_F(t)}{dt} = K_1 C_P(t) - (k_2 + k_3 + k_5) C_F(t) + k_4 \mathrm{C_b}(t) + k_6 C_{NS}(t) \tag{3.10}$$

$$\frac{dC_B(t)}{dt} = k_3 C_F(t) - k_4 C_B(t) \tag{3.11}$$

$$\frac{dC_{NS}(t)}{dt} = k_5 C_F(t) - k_6 C_{NS}(t) \tag{3.12}$$

For these compartmental models, the measured data with PET, C_{PET}, can be described as the sum of concentrations for each compartment, assuming that there is no tissue blood volume or tissue vascular fraction. By knowing C_{PET} and C_P, the arterial input function (AIF), rate constants K_1 to k_4 can be calculated by least squares curve fitting. However in practice, the VOI drawn in the tissue also includes a fraction of blood present in capillaries and tiny vascular structures. In brain studies, the fraction of blood volume (V_b) is sometimes assumed to be a constant value (i.e. 0.05 for grey matter) [Leenders et al., 1990] but is often estimated together with kinetic parameters. This relationship can be written for two tissue compartmental

model as:

$$C_T = (1 - V_b)(C_F + C_B) + V_b C_{WB} \tag{3.13}$$

As can be seen in 3.13, the blood volume contributes to the tracer concentration in whole blood, C_{WB}. The whole blood concentration can include the tracer in plasma, red blood cells and other radioactive components such as metabolite products.

Once the microparameters (K_1 to k_4) are estimated, these can be combined to compute macroparameters which can have a better reproducibility than microparameters. In ^{18}F-FDG studies, common macroparameters of interests are net influx rate constant (K_i) and cerebral metabolic rate of glucose consumption (cMRGlc) which is directly related to K_i. Total volume of distribution (V_T) and binding potential (BP) are also common macroparameters computed after kinetic modelling. Net influx rate and total volume of distribution can be computed as followings:

$$K_i = \frac{K_1 k_3}{k_2 + k_3} \tag{3.14}$$

$$V_T = \frac{K_1}{k_2} \tag{3.15}$$

for 1-TC model

$$V_T = \frac{K_1}{k_2}(1 + \frac{k_3}{k_4}) \tag{3.16}$$

for 2-TC model.

In some cases, these macroparameters can also be computed using graphical analysis techniques which are further described in the following section.

3.1.4 Graphical Analysis Techniques

PET kinetic modelling can be simplified by using graphical models which are based on compartmental models. Graphical methods benefit from not requiring any non-linear computational fitting. For irreversible tracers, the Patlak model [Patlak et al., 1983] [Rutland, 1985] can be used whereas the Logan analysis [Logan et al., 1990] is one of the approaches that can be used to analyse tracers with reversible binding kinetics.

3.1.4.1 Patlak Method and Logan Analysis

The Patlak approach [Patlak et al., 1983] involves linearisation of the two-compartment model for irreversible tracers (i.e ^{18}F-FDG), where k_4 can be assumed to be zero. It describes the behaviour of the system when the free tracer in tissue has reached its steady state. This usually happens in late time points after the bolus passage of the tracer. The Patlak approach can be formulated as equation 3.17.

$$\frac{C_T(t)}{C_P(t)} = K\frac{\int_0^t C_P(\tau)d\tau}{C_P(t)} + V \tag{3.17}$$

If the total distribution space of the tracer in the tissue is plotted against the normalised integrated tracer concentration in the plasma, a linear increase is expected to be seen. This relationship is shown in figure 3.4 where the net distribution space is $C_T(t)/C_P(t)$ and θ is integrated tracer concentration in arterial plasma:

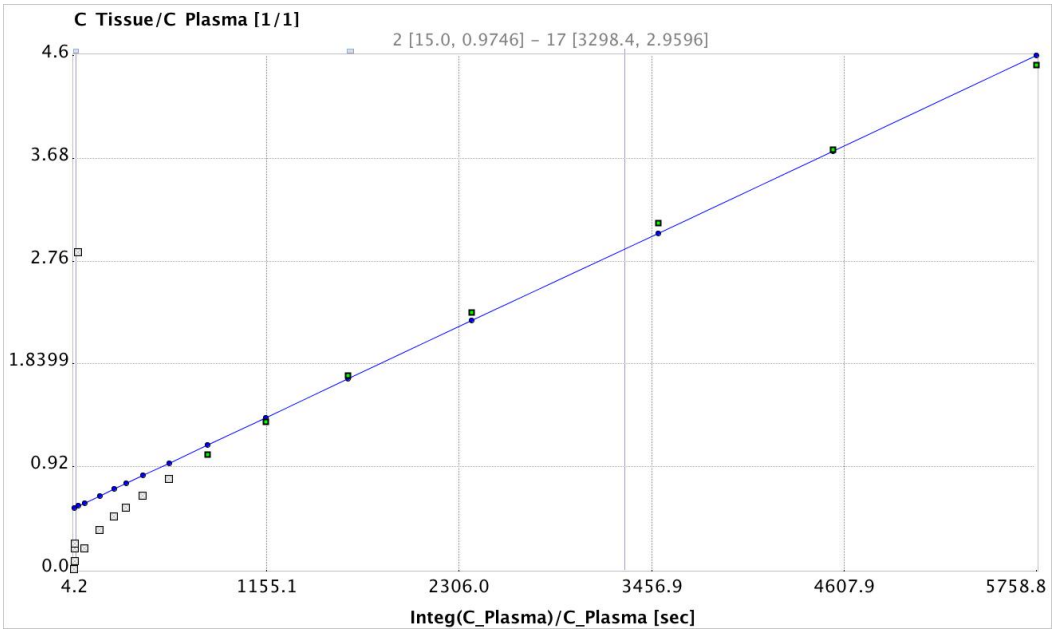

Figure 3.4: Patlak plot with the best linear fit to data points with filled rectangular points

The slope of the linear fit is directly proportional to influx constant (K_i) and rate of glucose consumption cMRGlc for FDG, which can be estimated by using equation 3.18, where LC is the lumped constant which represents the difference between FDG and glucose in transportation and phosphorylation and is assumed to be constant. C_{PG} represents the cold glucose concentration in plasma which is usually measured from a blood sample.

$$\text{cMRGlc} = \frac{K_i C_{PG}}{LC} \tag{3.18}$$

The original formulation of Logan analysis [Logan et al., 1990] is similar to Patlak technique but Logan analysis is applied to PET radiotracers with reversible binding characteristics. The Logan plot can only be used to calculate the distribution volume if a suitable, receptor-free reference region is present or if the metabolite corrected plasma concentration is known. The measured PET activity in tissue can

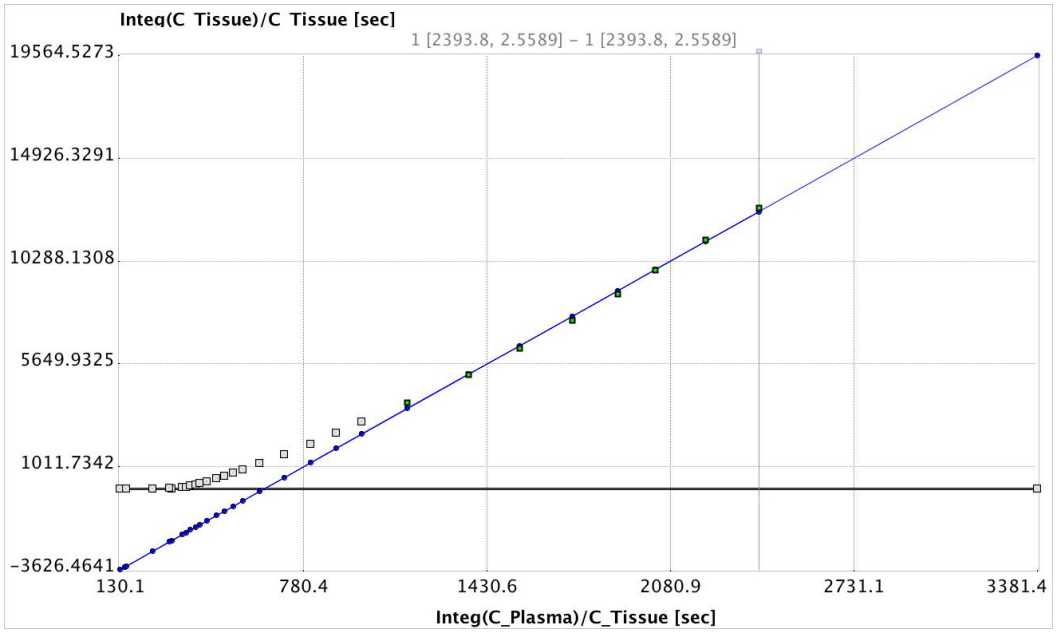

Figure 3.5: Logan plot with the best linear fit to data points with filled rectangular points

be plotted using:

$$\frac{\int_0^t C_T(\tau)d\tau}{C_T(t)} = K\frac{\int_0^t C_P(\tau)d\tau}{C_T(t)} + V \tag{3.19}$$

When both sides of this equation are plotted, as shown in figure 3.5 the plot approaches a straight line after a suitable time. K, the gradient of this line gives us the distribution volume of the tracer (V_T) in the tissue.

3.2 MRI

3.2.1 Dynamic MRI

Perfusion is physiologically defined as the steady-state delivery of blood to the tissue of interest and is one of the important physiological parameters measured in dynamic studies. There are several techniques developed using MRI to derive perfusion-related parameters, mainly used with gadolinium-based contrast agents.

These techniques use dynamic MRI, a similar concept to dynamic PET. Perfusion MRI is widely used in research studies, especially in brain imaging to assess acute stroke or intracranial tumours [Essig et al., 2013].

As also briefly introduced in Chapter 2, Gd-based contrast agents shorten T_1, T_2 and T_2* relaxation times, changing the contrast in the reconstructed MR images. This can be used to quantify the concentration of the contrast agent in the tissue of interest. Gd-based contrast agents are found in chelates, and due to their large molecular size, they cannot penetrate into the intracellular space of tissues and have a rapid excretion from the body. Gd-DTPA (Magnevist, Schering AG, Berlin, Germany) and Gd-DOTA (Dotarem, Guerbet, Paris, France) [Thomsen et al., 2002], [Bousquet et al., 1988] are two of the commonly used MR contrast agents in our institute.

Various methods have been developed to noninvasively measure the perfusion parameters with MRI. It must be noted that most of the work has been directed to the brain region, to measure the cerebral perfusion with MRI. The main methods used in this context can be listed as: Dynamic Contrast Enhanced MRI (DCE-MRI), Dynamic Susceptibility Contrast Enhanced MRI (DSC-MRI), and Arterial Spin Labelling (ASL). The first two methods require the injection of a contrast agent. DCE-MRI utilises the relaxivity effect of this contrast agent on the signal echo and DSC-MRI utilises the susceptibility effect of Gd on the signal echo. On the other hand, ASL uses magnetically labeled blood as a tracer to give desired perfusion parameters. There is no section included for ASL in this thesis but more information about it can be found in the literature [Kim and Kim, 2007] [Kwong

et al., 1995] [Detre et al., 2012]. DSC-MRI and DCE-MRI are further explained in the following sections.

3.2.2 DCE-MRI Quantification Techniques

Dynamic Contrast-Enhanced (DCE) imaging has been increasingly used in characterising tumour biology and treatment response. It requires acquisition of T_1-weighted MRI images in series with short time intervals before and after the injection of the contrast agent. Using the data obtained from DCE-MRI, compartmental models, similar to the techniques used to analyse dynamic PET images as explained in section 3.1.3, can be used to get information about the dynamic behaviour of the contrast agent within the tissue of interest.

When the paramagnetic contrast agent enters the body, it changes the relaxation times of water protons and hence increases the contrast observed in the T_1-weighted images. The increase in relaxation rate, $1/T_1$, can be related to the molar concentration of the contrast agent in each voxel using equation 3.20.

$$\frac{1}{T_1} = \frac{1}{T_{10}} + r_1 C_{Gd} \tag{3.20}$$

where T_{10} is the spin-lattice relaxation time before the arrival of contrast agent and r_1 is the spin-lattice relaxivity constant. C_{Gd} represents the molar concentration of the Gd in tissue of interest. However, this equation is valid only with the assumption the Gd available in the tissues relaxes all of the water independent of time. Therefore in-vivo, a nonlinear relationship between the signal intensity and the Gd concentration, which can be specific to the pulse sequence, is often used.

After finding the Gd contrast agent concentration from the MRI signal enhancement, pharmacokinetic modelling can be performed. Similar to analysis of dynamic PET data, compartmental models can be used to analyse DCE-MRI data. The main difference between dynamic PET and DCE-MRI compartmental analysis is that in DCE-MRI, there is no need for a second tissue compartment to represent intracellular processes as the Gd chelates can not pass the cell membrane and stay in the extracellular space.

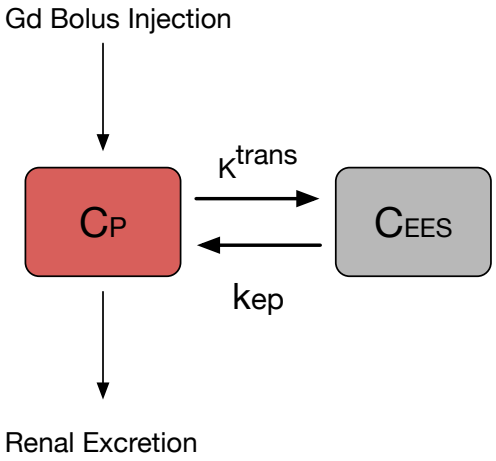

Figure 3.6: Tofts model which with one tissue compartments, used to perform kinetic analysis on DCE-MRI data. K^{trans} represent the transfer from blood plasma to extracellular space and k_{ep} represent the transfer back to the blood plasma

The simplest compartmental model used in DCE-MRI analysis is the one-compartmental model, or Tofts model, which includes a compartment representing extravascular extracellular space (EES) [Tofts and Kermode, 1991] [Tofts et al., 1999]. Equation 3.21 can be extracted from this model, which is identical to the PET one tissue compartmental model. Similar to PET, $C_P(t)$ represents the concentration of the contrast agent found in the blood plasma, so called the arterial input function. Again, this can be measured in subjects by using arterial blood samples,

an image derived method or population average. This is further explained in section 3.3.

$$C_{EES}(t) = C_P \otimes K^{trans} e^{(-k_{ep}t)} \tag{3.21}$$

$$C_T(t) = V_b \mathrm{C_{WB}} + C_P \otimes K^{trans} e^{(-\mathrm{k_{ep}}t)} \tag{3.22}$$

where C_P is the AIF, K^{trans} is the rate constant for the transfer between the blood plasma and extravascular extracellular space (EES) and k_{ep} is the rate constant describing the transfer from extracellular space to intravascular space.

The Tofts model was originally constructed for agents which are diffusible, and remain extracellular, rather than very large molecules that remain intravascular [Tofts et al., 1999]. However in some tissues, particularly in tumours, the assumption of negligible intravascular agent is invalid. To overcome this limitation, the extended Tofts model can be used which also allows for the intravascular contribution, as shown in equation 3.17. Here, V_b is the volume fraction of the plasma space. The total Gd concentration in a voxel or ROI is the sum of the EES contribution, which is usually the dominating part, and the intravascular contribution.

3.2.3 Theory of DSC-MRI Acquisition and Quantification

Dynamic susceptibility contrast-enhanced magnetic resonance imaging (DSC-MRI) with bolus injection of Gd-based contrast agent is one of the most commonly used MRI methods to obtain brain perfusion images. It has a fast acquisition time, around 2 minutes, and provides a higher contrast-to-noise ratio compared to other perfusion

imaging methods, such as ASL or perfusion CT.

The contrast in DSC-MRI images is based on the signal changes generated during the passage of the contrast material through the vasculature. The Gd based contrast agent behaves differently within the brain compared to the rest of the body. Due to the presence of blood-brain barrier, the contrast agent is trapped in the intravascular area, in contrast to other body regions where it rapidly equilibrates between intravascular and extravascular extracellular compartments. This causes a significant decrease in T_2 and T_2^* relaxation signals which can be converted into time-dependent concentration of the contrast agent for each voxel [Rosen et al., 1990]. The concentration of the contrast agent in a ROI can be expressed using the equation 3.23.

$$C_T(t) = \text{CBF}(C_P(t) \otimes R(t)) = \text{CBF} \int_0^t C_P(\tau) R(t-\tau) d\tau \tag{3.23}$$

Where the C_P is the arterial input function, CBF is cerebral blood flow, R(t) is the impulse function of the system (or the residue function) and $\otimes$ describes a convolution operation. R(t) can be described as the fraction of contrast agent concentration at time t after an ideal instantaneous input bolus [Calamante, 2002] [Calamante, 2013]. This equation can be deconvolved to measure the CBF of the patient.

DSC-MRI can also be used to measure cerebral blood volume (CBV) and the mean transit time (MTT) parameters. CBV represents the fraction of tissue volume occupied by blood, usually in units ml g^{-1} and MTT is the time it takes in seconds

for the contrast agent to travel from vascular space and arrive to the tissue of interest. The relationship between CBF, CBV and MTT parameters is written as:

$$\text{MTT} = \frac{\text{CBV}}{\text{CBF}} \tag{3.24}$$

Due to the compartmentalisation of the contrast agent in the vascular space, it can be assumed that the CBV is proportional to the normalised amount of total contrast agent, as written in 3.25:

$$\text{CBV} = \varphi^{-1} \frac{\int C_T(t)dt}{\int C_P(t)dt} \tag{3.25}$$

where φ is a scaling factor which is used as a normalisation factor to account for the fact that higher amounts of injected contrast agent will cause higher concentrations reaching the tissue, regardless of the value of CBV.

3.3 Arterial Input Function

An accurate knowledge of the arterial input function (AIF) is required for correct quantification of dynamic PET and dynamic MRI datasets. AIF describes the concentration of tracer in PET, or contrast agent, within the blood plasma which is available to get bound or metabolised. Usually, the whole AIF, from the time of injection to the end of the scan, is required if the complete time course of the dynamic PET or MR datasets is desired to be analysed. An example of arterial input function is shown in figure 3.7. When a bolus injection is used, the AIF curve increases rapidly to its peak value with the arrival of the tracer/contrast agent to the arteries

and after about half a minute, the rate of change decreases and plateaus as most of the tracer is transferred from the plasma.

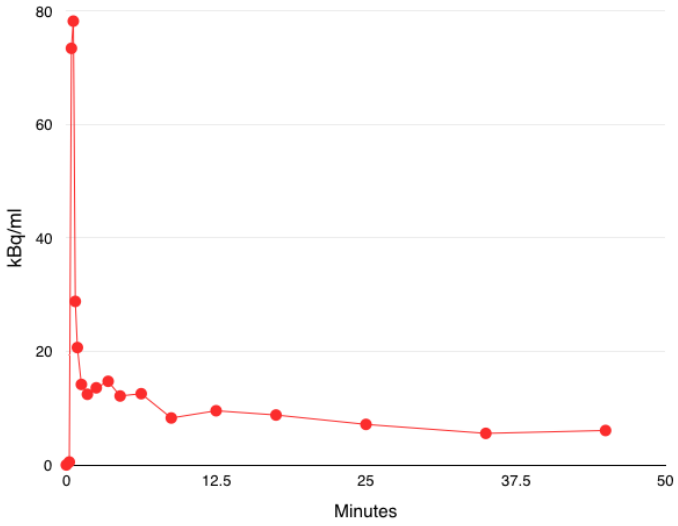

Figure 3.7: A representation of arterial input function obtained from carotid arteries in a brain ^{18}F-FDG study

There are various methods to obtain the AIF and each of these has its own advantages and disadvantages. There is no agreed guideline to be used in the measurement of AIF and this field is open to research as its correct estimation is vital for accurate kinetic analysis. A brief description of AIF measurement methods is given in the next section and their comparison is made stating strengths and weaknesses of each method.

Arterial blood sampling can be regarded as the gold standard of the methods used for the measurement of arterial input function. Following the injection of the radiotracer, serial blood samples are drawn over time and blood sample tubes are centrifugated to seperate plasma. Then, a measured volume of blood from each sample is analysed in a radiation detector, giving the concentration of tracer present in the blood plasma at that time point. Typically, around 20 to 30 blood samples

are required for routine modeling of a dynamic PET scan [Muzi et al., 2012]. Even though this method gives most accurate measurement of the input function, it is a very invasive process which involves risks to the subject and practitioner alike and is complicated as it requires handling radioactive blood. In addition, it is time consuming and can be more costly as it requires extra staff and equipment. For this reason it is difficult to justify arterial blood sampling for routine clinical imaging. One of the other limitations of arterial sampling is the possible delay and dispersion problems. Arterial samples are usually withdrawn from a radial artery which can be distant to the tissue of interest. In such cases, the AIF measured from arterial samples would suffer from delay and dispersion effects which need to be accounted for before an accurate kinetic analysis can be performed. Even though arterial blood sampling can be used to measure the concentration of PET tracer and MR contrast agent, it is more often a method of choice in PET studies.

One alternative method to blood sampling is to use of standardised, population-based arterial input functions. In this method, an average of AIF curves from a group of subjects is calculated and is used as the AIF in future kinetic analyses of that tracer. This can also be combined with one or two measured arterial blood samples, which are used to scale the population based AIF [Takikawa et al., 1993]. The main advantage of this method is its simplicity as no individual AIF measurement is required. However, it brings the risk of introducing large errors into the kinetic analysis as the AIF curve shapes can vary between subjects and scans. In addition, finding a reliable population derived AIF can be possible in dynamic MRI and common PET tracer studies (i.e. ^{18}F-FDG study) but is more difficult when less

common or more recent PET tracers are studied.

Another approach to derive AIF involves placing a volume of interest (VOI) on a suitable artery present in the dynamic PET or MRI image, and deriving the time activity curve of the tracer concentration in plasma over the time course of the scan. The AIF obtained using this method is called an image derived input function (IDIF). The VOI can be placed on the artery manually or automatic image segmentation methods can be used to delineate arteries. The advantage of IDIF extraction is that it is completely non-invasive and requires only post-processing of the image data. However, arteries can be very small in diameter, compared to the resolution of the reconstructed images in PET, and used images can contain significant amount of noise and blurring. In this case, detection of arterial voxels can be problematic using both manual and automatic segmentation methods. The images also suffer from PV effects, introducing errors to the measured total activity, and a PV correction needs to be performed to correct for spill-in and spill-out from neighbouring voxels around the artery before an IDIF measurement is done.

As an alternative to traditional methods to obtain arterial input function, Feng et. al [Feng et al., 1997] proposed their technique which can simultaneously extract AIF and physiological parameters from dynamic PET images. In this method, the AIF is modelled using a mathematical expression. Time activity curves are obtained from multiple regions and kinetic parameters to fit these curves are estimated together with AIF parameters. Details about this method can be found in Chapter 5.

One big problem affecting measurement of an AIF in several PET studies can be the presence of metabolite products in the blood plasma. As illustrated in figure

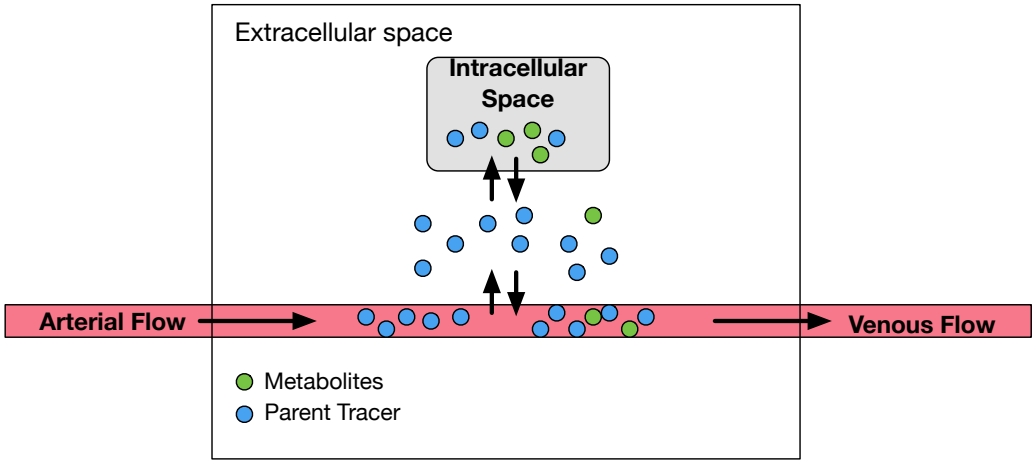

Figure 3.8: A representation of metabolite formation process which happens during the metabolism of the PET tracer in intracellular space.

3.8, during the metabolism of the PET tracer in the body organs, metabolite side products can be formed, which can consequently transfer back to the blood. These metabolite products can still carry the radionuclide label and hence contribute to the radioactive concentration in the blood. These metabolite products usually do not transfer to the brain tissues as they cannot pass the blood-brain barrier. However, they can sometimes reach other tissues and organs and a modified compartmental model to account for metabolites needs to be used in such cases [Tomasi et al., 2012] [Watabe et al., 2006].

The measured blood concentration therefore needs to be corrected for the concentration of metabolites before it can be used as an AIF. This is performed by collecting several arterial blood samples during the PET acquisitions and measuring the concentration of labelled metabolites. The measured blood samples are firstly converted into plasma samples by separating the plasma from red blood cells. The tracer is then further separated from metabolites using High Performance Liquid Chromatography (HPLC). Radioactivities of each fraction are measured using a

well counter. The parent fraction can be then computed by taking the ratio of the parent tracer concentration to total plasma concentration. A parent fraction is 1 at time zero and then follows an exponential decay as the metabolites start to build in the blood. Samples in parent fraction are usually fitted using parametric models [Tonietto et al., 2016]. The fitted parent fraction is multiplied with the plasma blood curve to obtain the true AIF.

Chapter 4

Improved quantification of clinical dynamic FDG images using image derived input functions with MR-defined carotid arteries

4.1 Introduction

Image derived input function is a non-invasive alternative to arterial blood sampling and measure the AIF from reconstructed PET images. The simplest way to measure the tracer concentration in blood plasma is to place a volume of interest on a suitable artery and measure the tracer concentration within that VOI in each frame. However, this method has severe limitations when it is applied to brain images. Due to the limited spatial resolution of the PET images, reconstructed images of small objects usually suffers from partial volume effects. This causes errors in the quan-

tification of PET images including image derived input function (IDIF) calculation. For instance, carotid arteries have a small diameter of about 4-6 mm [Krejza et al., 2006b] which makes it challenging for typical PET scanners with an intrinsic resolution of 4 to 5 mm to delineate its actual geometry. Anatomical MRI images with higher spatial resolution can be used in such cases to correct for spill-in and spill-out effects, and hence improve the PET quantification and IDIF estimation. This brings the challenges of PET/MRI image registration, anatomical segmentation of carotid arteries from MRI images, and partial volume correction of each PET frame. In this chapter, the methods we have developed to address these challenges within the PET IDIF measurement context are described. Furthermore, the validation of the PVC and IDIF method with simulated and clinical ^{18}F-FDG data against the gold standard arterial blood samples is presented.

4.2 Literature Survey

The most straightforward way of deriving an IDIF is locating a large diameter blood pool, such as the heart [Choi et al., 1991] or the aorta [van der Weerdt et al., 2001], placing the VOI in their inner structure to minimise or neglect the PV effects. These techniques were successfully validated in multiple studies. However, since a vascular structure with a large diameter is not present in the field of view in brain PET studies, the IDIF measurements are usually performed on carotid arteries. Carotid arteries have an average diameter which is slightly smaller than the spatial resolution of the PET camera, which makes it necessary to apply a correction for spill-in and spill-out effects. In this section, we particularly focus on techniques which

utilise MRI information to more accurately derive IDIF from PET data.

There have been various studies aiming to validate IDIF extraction techniques over the last 20 years. In 1998, Chen et al. [Chen et al., 1998] developed and validated a method to non-invasively measure cMRGlc using ^{18}F-FDG PET data. The spill-in effects were corrected by including a spill-in correction based on a ROI drawn outside the carotid arteries. Recovery coefficients and spillover coefficients were estimated by using linear or nonlinear least square methods to fit the carotid and background curves. Fregonara et. al also presented a study in 2009 where eight different IDIF extraction methods used in dynamic FDG studies were compared [Zanotti-Fregonara et al., 2009a]. The methods were compared on two numerical human brain phantoms as well as on four healthy volunteers with FDG scans. Six of the methods they compared were algorithms that rely on anatomic information such as ROIs over the carotid arteries where two of them work without any prior anatomic assumption, automatically extracting TACs using kinetic information. Area under curve, cMRglc values calculated with Patlak analysis [Patlak et al., 1983] and individual rate constants were calculated. The results of this comparison study showed that extracting the IDIFs without any blood samples to scale the tail of the curves is difficult and late venous blood samples should be obtained if possible. None of the methods presented in this paper managed to completely correct the partial volume effects and usually underestimated the curve tail. The authors concluded that a reliable blood-sample-free IDIF extraction method was not available for FDG PET brain studies at the time of writing.

Since anatomical brain images with a much higher spatial resolution can be

obtained using MRI scanners, there have been a growing interest to use MR images in the PVC of the PET images before deriving the IDIF. Furthermore, detection of blood vessels using manually drawn ROIs can be inaccurate due to human errors which tends to be non-reproducible. Therefore, using automatic artery segmentation on MRI images for PET-AIF determination can be beneficial. In 1997, Litton used internal carotid arteries defined on MR images to derive the corresponding radioactivity curves on the PET images [Litton, 1997]. It was concluded that their study was limited by the poor resolution of the PET scanner used at that study. Trebossen et al. [Trebossen et al., 1998] also tried to derive a PET IDIF by placing an ROI on the internal carotid arteries on HR PET images, but corrected for the PV effects using geometry extracted from an anatomical MRI image with a voxel size of 1 mm and GTM method [Rousset et al., 1998a]. In their work, they assumed a PSF of PET scanner to be 6.8 mm FWHM. The results were compared to arterial samples and variations were seen in the estimated cMRGlc values (in a range of 2% to 27%).

In 2012, da Silva et al. [da Silva et al., 2013] used a high resolution MR-compatible BrainPET insert within a 3T Siemens MR scanner to acquire simultaneous PET and MRI images. In this study, three healthy volunteers were scanned. The MPRAGE MRI images were resliced to the PET space and isocontours were defined on carotid arteries. These coordinates were transferred to coregistered dynamic PET images. It was concluded from their study that an accurate co-registration of the carotid arteries can be obtained for PET and MRI images acquired by an integrated scanner. Hence, carotid arteries defined on higher resolution MRI images can be

transferred onto PET images for a more accurate AIF determination. Fung et al. have also published their work where they used MR-defined carotid centrelines for an image-derived input function in PET [Fung and Carson, 2013]. They performed [^{15}O] water PET on nine healthy patients with blood samples for conventional input function measurement. The same patients also had T_1-weighted MPRAGE images on a separate 3T MR scanner. Left and right carotid arteries were segmented from this MRI image using the active contour model of Chan and Vese [Chan and Vese, 2001]. After that, the centrelines were extracted from the segmented carotids. To do that, the vessel centrelines were modelled as cubic B-spline curves. The curved shape of arteries was characterised entirely in 3D space by using control points in the 3D coordinate system of the image and centreline models were fitted to the segmented arteries. Locations of the control points which minimise the sum of the squared Euclidian distance between carotid voxels and and their corresponding nearest points along the B-spline curve were estimated in an iterative manner. After the segmentation of carotid arteries and extraction of their centrelines, non-brain tissue was extracted from MR images and stripped MR brain images were registered to PET images using a rigid transformation. As a final registration step, local registration was performed to re-register centrelines using rigid transformation. This step was done to eliminate small registration errors which could be present after the global registration step. The input function was extracted using the mean value of carotid centreline intensities on dynamic PET frames and areas under curves were compared to the arterial input function obtained from blood samples. They have assessed their method by comparing the area under curve (AUC) of the IDIF and

the CBF to the gold standard curve, obtained from arterial blood samples. Their results showed that the method was able to yield a consistent IDIF for a subject across multiple injections, if a scaling factor can be derived from the ratio of IDIF and arterial blood samples. However, they concluded that carotid ROIs with larger diameters will be required in a simultaneous PET-MR system, as its resolution would be lower than the HRRT, causing some more spill-in effects. Lyoo et al. [Lyoo et al., 2014] developed a fully automatic method to derive IDIFs in [^{11}C](R)-rolipram PET studies, utilising T1 weighted structural MR images. Time average of the PET frames were measured and the average was spatially normalised to the Montreal Neurological Institute (MNI) MR template space. Then the average of spatially normalised PET images for 10 subjects was computed to create a template for this specific ligand. The time activity curves for grey matter and white matter were derived from regions segmented from coregistered MR images. Carotid arteries were manually segmented from the average of early PET images to generate a template for the blood signal. The template TACs for GM, WM and carotid arteries were used within a supervised clustering method to describe similarity of each voxel to these template TACs. The delineated carotid artery voxels were used to generate the image derived whole blood curve. PVC was performed using a method similar to that presented by Chen et al. [Chen et al., 1998]. A good similarity in V_T values computed by arterial samples and IDIFs was observed.

Time of flight MRI angiography (MRA) images with a high spatial resolution and a good arterial blood signal contrast can be used to improve the accuracy of carotid artery segmentation. Su et al. [Su et al., 2013b] used MRA images together

with [^{15}O]H_2O data acquired on a high resolution PET scanner to derive IDIFs. Carotid arteries, signal contributing tissue i.e brain tissue, muscle and non-signal contributing tissue i.e bone, cerebrospinal fluid, and airways were segmented from the MRA images using a modified adaptive segmentation algorithm [Wilson and Noble, 1999]. The PET data were modelled as a linear mixture of true arterial signal and PV effects from surrounding tissues. The amount of partial volume effect was derived from an empirically derived PSF, which was found by matching the IDIF to arterial samples for one subject. The AIF was simultaneously measured with the CBF and highly reproducible CBF estimations with a good agreement to arterial samples were obtained. Jochimsen et al. [Jochimsen et al., 2016] also utilised MRA images to segment arteries from neck images in [^{15}O]H_2O sheep studies to derive the IDIF. In order to segment the arteries, a vessel enhancing filter to enhance the blood signal was applied. Then, an image thresholding and a clustering technique was applied to segment the major arteries. In the PV correction, a PSF, which was derived from a cylindrical syringe phantom experiment, was used. The GTM method was used to correct for PV effects and the normalised mean activity in each PET frame was used to derive the IDIF. They found that CBF values estimated by the IDIFs were 22% higher than the ones estimated with arterial samples. This was due to the differences in sampling locations as a result of delay and dispersion effects. Su et al. has also used TOF-MRA images to derive the IDIF in amyloid scans with PiB tracer [Su et al., 2015]. Similar to their previous work, the recovery coefficients were determined based on an experimentally measured PSF and segmented artery and background regions. Metabolite correction was performed

using population based data. The distribution volume V_T was computed using Logan graphical analysis and a good agreement with a comparable variability against arterial samples was observed.

Audrey et al. has presented effects of using atlas based and ZTE-based MR based attenuation techniques in the shape of the derived IDIFs [Fan et al., 2016]. They have focused on the neck region where atlas based attenuation techniques are more problematic. A difference was observed in the estimated IDIF peaks where the atlas based MRAC method yielded a smaller peak. A difference in the CBF measurements was also observed. Khaligni et al. has developed a method to get PET angiography images using time of flight information on GE Healthcare's Signa PET/MR scanner [Khaligni et al., 2016a]. The optimal time to segment arteries from PET images was found by binning the PET list mode file every second and plotting the total number of true and scatter coincident events over time. The PV effects were corrected using the artery volumes calculated from TOF-MRA images. This method was applied to [^{15}O]H_2O PET studies and it was observed that using MRA images with smaller voxel size and and a thinner slab resulted in more accurate CSF estimates and are recommended for IDIF estimation [Khaligni et al., 2016b].

4.3 Theory of the Single Target Correction method

As described in the literature review section of this chapter, there have been various IDIF extraction techniques which can be applied to multiple PET tracer studies. In order to account for PV effects, these existing methods require complete parcella-

tion of the images into multiple regions, including the background regions. When used to measure IDIF from carotid arteries, these PVC methods bring the need for unnecessary complex segmentation of brain structures. In this section, a more practical PVC method, called Single-Target Correction (STC) is presented. This method requires the segmentation of the structure of interest (i.e. carotid arteries) only and is not dependent on any separately segmented background regions.

For a carotid artery IDIF extraction application, the STC only requires delineation of the carotid arteries, and an accurate measurement of the point spread function, representing the blurring applied to the reconstructed PET images. It is not dependent on any separately segmented background regions and hence, unlike other methods, it does not require complex segmentation of the background areas. The correction is an iterative procedure and is performed on a voxel-by-voxel basis to correct for spill-in effects. Individual voxel values were used for the spill-in correction. Uniform activity concentration is assumed for spill-out effects and a region-based concentration is performed. The STC method is an extension of the previously published Multi-Target Correction method [Erlandsson et al., 2006], which itself is an extension of the Müller-Gärtner method [Müller-Gärtner et al., 1992].

The first step in the PVC involves creation of the blurred mask image. In each iteration step, the spill-over effects are corrected between the voxels which are within the volume of interest and background voxels present outside the VOI. This is done by subtracting a background term, which is re-calculated in each iteration. After that, the algorithm corrects for spill-out by dividing by recovery coefficients,

which depend only on the size and shape of the VOI and on the PSF of the system. This follows from the assumption of uniformity.

If a(·) is the true image, the image, b(·), which is blurred by the PSF, can be described as follows:

$$b(x) = \int a(y)h(x,y)dy \tag{4.1}$$

where h(·,·) is the PSF, which is assumed to be position-invariant although this is not strictly necessary, and x and y are 3D spatial coordinates.

If a VOI is defined, called Ω, the STC method can be described as follows in pseudo-code:

$$\tilde{a_0} = b(x) \tag{4.2}$$

$$R(x) = I_\Omega(x) \int_{y\in\Omega} h(x,y)dy + (1 - I_\Omega(x)) \int_{y\notin\Omega} h(x,y)dy \tag{4.3}$$

for k=0 to N-1, begin

$$g_k(x) = I_\Omega(x) \int_{y\notin\Omega} \tilde{a}_k(y)h(x,y)dy + (1 - I_\Omega(x)) \int_{y\in\Omega} \tilde{a}_k(y)h(x,y)dy \tag{4.4}$$

$$\tilde{a}_{k+1}(x) = \frac{1}{R(x)}(b(x) - g_k(x)) \tag{4.5}$$

end

where ã (·) represents the PV corrected image after k iterations. I_a is the indicator function for Ω, R(·) involves the recovery factors to correct for spill-out effects, $g_k(\cdot)$ is the spill-over term that is estimated at iteration, and N represents the total number of iterations used in the correction. Convergence is typically reached after 5-10 iterations. The result is an image, in which all voxels inside Ω have been corrected for PVE, but the correction also extends beyond the boundaries, as far as the width of the PSF.

The main difference between STC and the Müller-Gärtner method [Müller-Gärtner et al., 1992] is that STC does not require prior estimation of the mean value in the background region/regions for the spill-in correction. Instead, this correction term is estimated iteratively on a voxel-by-voxel basis. For this purpose, it is necessary to estimate the spill-over in both directions across the region boundary.

4.4 Experiments with simulations

In order to test the performance of the STC in partial volume correction for IDIF applications, a simulation study was designed to simulate PET images from segmented carotid artery MR data. This simulated PET data were used to check the performance of the STC method on different tracer concentrations. The data were also used in the evaluation of an image-based PSF measurement method.

4.4.1 Generation of simulated data

Segmented carotid arteries from a TOF MR angiography image were used as the ground truth in this simulation work. The segmented carotid arteries was a binary

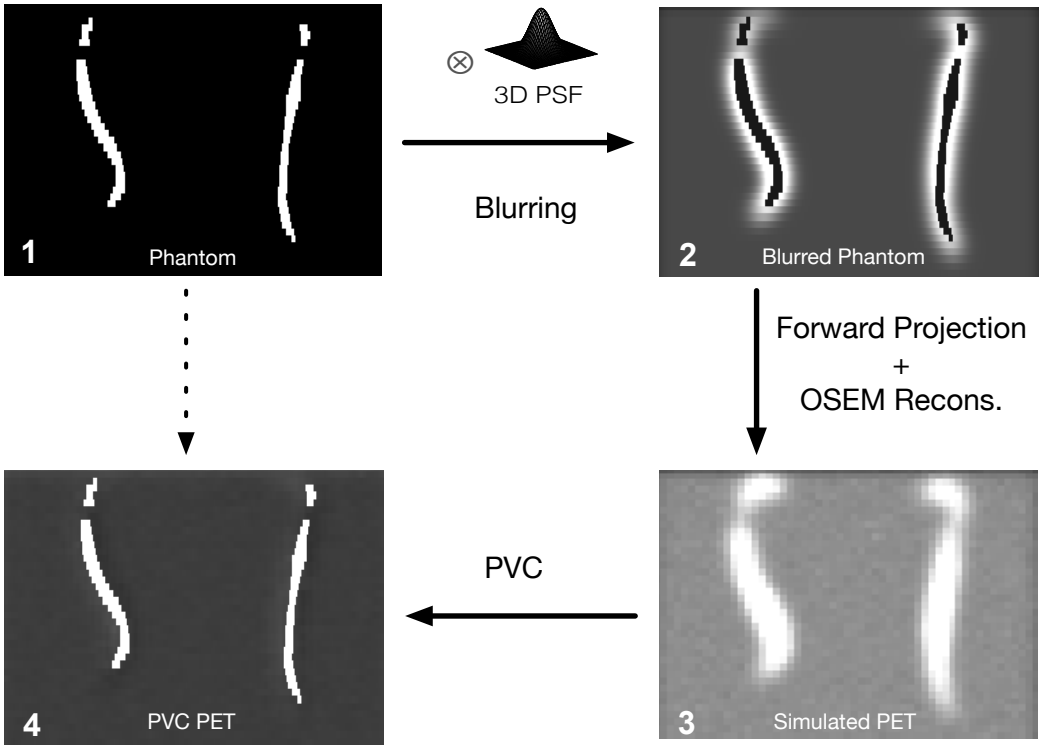

Figure 4.1: Overview of the method used to generate simulated PET data of carotid arteries. Carotid arteries segmented from MRA images are blurred with the PSF and then forward projected and reconstructed using OSEM method to obtain simulated PET images. The PET image is inputted to the PVC method with the segmented arteries to obtain corrected PET image.

image with a voxel size of 0.39 x 0.39 x 1 mm. First, an attenuation map was generated using this true image by assigning an attenuation coefficient value of 0.096 cm^{-1} to the artery region. To generate a digital 3D phantom, emission values were assigned to a uniform background region and inside carotid arteries on the segmented images. Six phantoms were generated with a carotid artery to background ratios of 1/10, 1/5, 1/3, 1/1, 1.5/1 and 2/1. Therefore, it can be said that 3 of these digital phantoms were used to mainly evaluate the performance of spill-out correction, and 2 were used to mainly evaluate the spill-in correction.

Overview of the steps taken to generate simulated data is illustrated in figure

4.1. Each phantom was blurred using an isotropic Gaussian PSF with FWHM of 6.50 mm. Then the blurred phantoms were forward projected using Software for Tomographic Reconstruction (STIR) [Thielemans et al., 2012] to simulate the 3D PET acquisition data. The Siemens Biograph mMR scanner geometry was simulated, taking account of attenuation and scatter. Poisson noise was added to the projected data. PET images were reconstructed using OSEM with 3 iterations and 21 subsets for a 3D matrix with a voxel size of 2.08 x 2.08 x 2.013 mm.

4.4.2 Application of the STC method to the simulated data

PV correction was applied to each reconstructed phantom image and the performance of the PV correction was compared against the true intensities. Firstly, the reconstructed images were resampled to MR angiography space (0.39 x 0.39 x 1 mm) using tri-linear interpolation. The STC PVC was applied on coregistered PET images with 15 iterations and the segmented carotid arteries as the mask image. In order to evaluate the effect of different PSFs in the PVC, STC was applied to each of the reconstructed phantoms with 15 iterations and the errors between the recovered and true carotid activities were computed for different PSFs. The optimal PSF FWHM value was found by minimizing the mean error, averaged across the six phantoms.

An alternative method was also applied with an aim to measure the PSF directly from the reconstructed images. In this method, as illustrated in figure 4.2, the centroids of the left and right carotid arteries in each axial slice were calculated. Next, the carotid arteries were blurred with the 3D PSF and line profiles were drawn

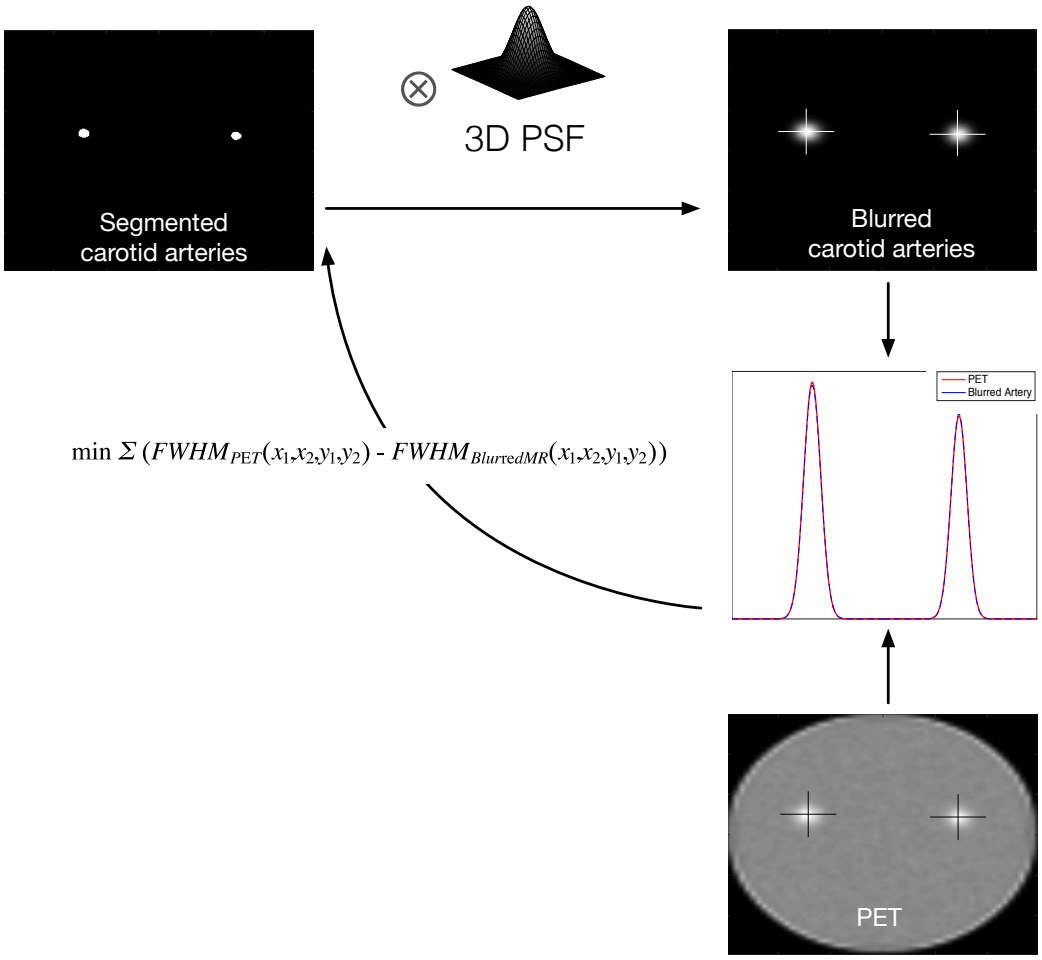

Figure 4.2: Illustration of method used to derive PSF from reconstructed PET images. The difference between FWHM of line profiles drawn through the centroids on PET and blurred MR images was minimized by varying the PSF

in x and y directions through artery centroid locations. The segmented images were blurred using a 3D Gaussian PSF. Line profiles were drawn through centroids of left and right carotid arteries in x and y directions on both PET and blurred segmented MR images. These line profiles were fitted with a Gaussian function and mean FWHMs of Gaussian fits were calculated for PET and blurred MRI data. This was repeated in an optimisation routine to find the optimal PSF, which gave the lowest difference between the mean FWHM of fitted Gaussian functions on PET and blurred segmented MR line profiles. In order to check the effect of errors in

the carotid artery segmentation on the measured PSF values, the experiment was repeated with under-segmented and over-segmented carotid arteries. This was done by eroding and dilating the original carotid arteries by adding or removing one or two voxels to its diameter.

4.5 ^{18}F-FDG Experiments

4.5.1 Materials

All of the datasets presented in this chapter were provided by Department of Clinical Physiology, Nuclear Medicine and PET of University of Copenhagen.Dynamic PET and anatomical MRI images were acquired on 21 healthy male subjects (mean age: 28.3 years, range: 22 to 40 years). All of the subjects had given written informed consent before the scans. The protocol for the experiments was approved by the Danish National Committee on Health Research Ethics (h-4-2012-167) and the studies were conducted in accordance to the Declaration of Helsinki.

Each subject received an intravenous bolus injection of 200 MBq of ^{18}F-FDG over 20 seconds followed by 10 mL of saline flush and underwent a dynamic PET scan on a Siemens Biograph 64mCT scanner (Siemens Healthcare, Erlangen, Germany). The PET scans lasted for 1 hour and 19 PET frames were reconstructed using the following frame durations: 6 x 10 seconds, 2 x 30 seconds, 3 x 60 seconds, 2 x 150 seconds, 2 x 300 seconds and 3 x 600 seconds. The PET images were reconstructed using OSEM with four iterations and 24 subsets and a 4-mm Gaussian filter was applied. The data were reconstructed into a 128 x 128 matrix with a pixel size of 2.5 mm and 74 slices were acquired with a slice thickness of

3mm. Attenuation correction was performed using information from the CT scan. The PET data were corrected for randoms, scatter, attenuation and radioactive decay. In order to stand as a gold standard in the comparison, arterial blood samples for measurement of radioactivity concentration in arterial plasma were drawn from the radial artery at 33 time points with various time intervals. For the early samples, 10 second intervals were used in order to get a good definition of the input function peak. Sampling was performed using vials with internal vacuum over 3 s at the beginning of each time interval. Immediately prior to each measurement, a similar vial was used to rinse residual activity out of the catheter. Plasma radioactivity concentrations were measured in a well-type gamma counter (COBRA 5003; Packard Instruments). Plasma glucose level and haematocrit were also measured for each subject.

The MR scans were acquired on a 3T Philips Achieva MRI scanner (Philips Medical Systems, Best, The Netherlands). A 32-channel phased array head coil was used in all scans. MPRAGE scans were obtained with a 3D T1-weighted turbo field echo sequence (150 slices, FOV=241x180x165 mm3, TE=2.78 ms, TR=6.9 ms, flip angle = 9 degree) and were reconstructed into a 150 x 224 x 224 matrix with a voxel size of 1.1 x 1.1 x 1.1 mm. 3D time of flight MR Angiography images were also acquired (TR=23 ms, TE=3.5 ms, flip angle= 18 degree) from 100 slices covering the lower head and upper neck regions. These slices had a thickness of 1 mm and covered a region of 200 x 200 cm. They were reconstructed to a voxel size of 0.39 x 0.39 x 1 mm. The summary of acquired PET and MR images is shown in figure 4.3.

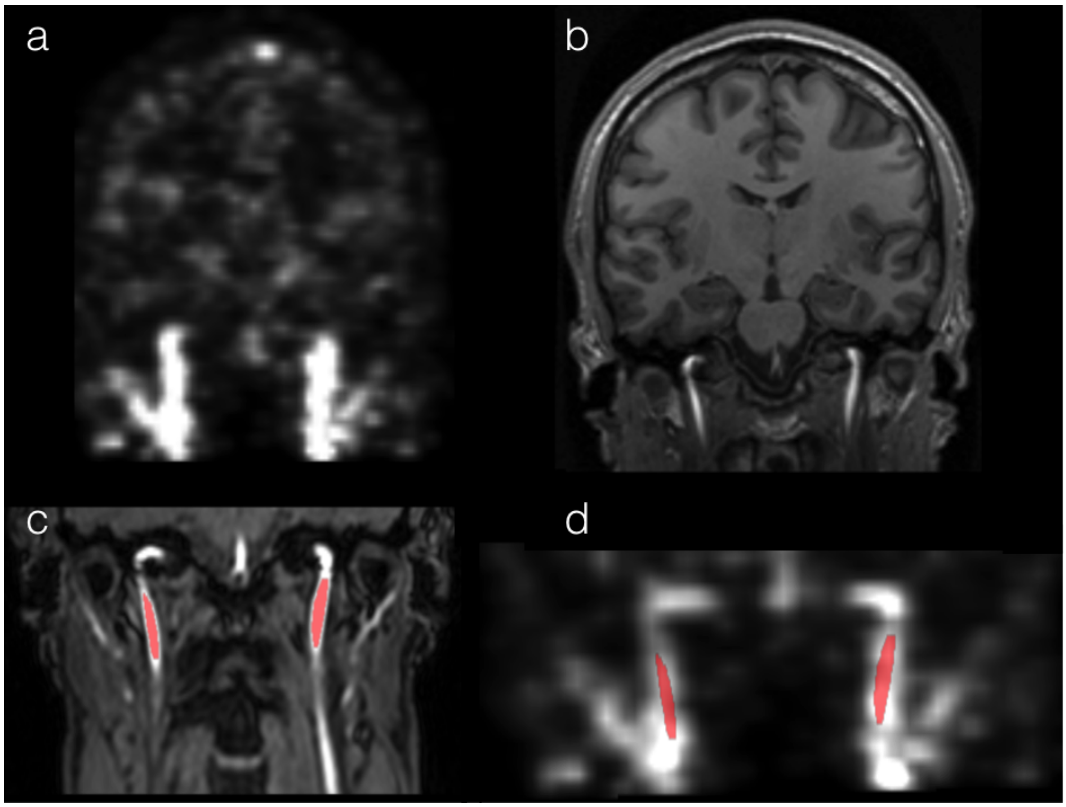

Figure 4.3: Images used in this study: (a) PET frame showing the arteries, (b) MPRAGE image of the brain, (c) TOF MR angiography image of neck region (d) PET frame co-registered to the MR angiography image. Marked voxels show the arterial voxels delineated from the MR angiography image

4.5.2 Data Analysis

Data from 2 of the 21 subjects were not included in the data analysis due to the movement of the head during the dynamic PET scan. Carotid arteries were segmented from MRA images using ITK-SNAP version 3.2 [Yushkevich et al., 2006], which includes an automatic active contour segmentation toolbox. Images were classified into two tissue classes using tissue classification and a region-growing algorithm was applied in the region with the arteries. Because of the different field of view of MRA images compared to the PET images, segmentation was limited to 3 cm below the petrous section of left and right internal carotids arteries (figure 4.3d). Maximum intensity projection image of segmented arteries for one subject is

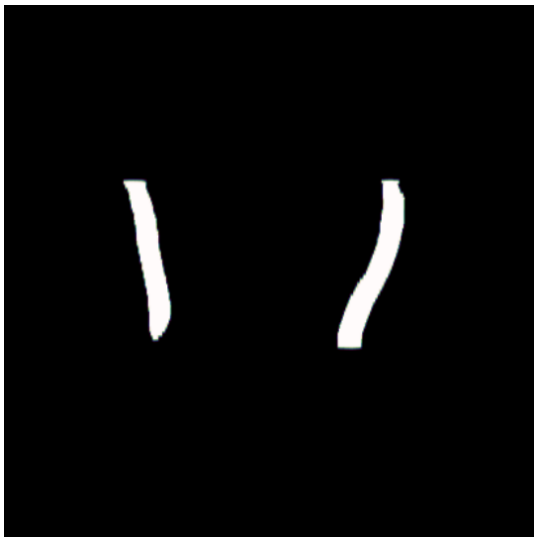

Figure 4.4: Maximum intensity projection of segmented carotid arteries for one subject

shown in figure 4.4.

FSL linear image registration tool [Jenkinson and Smith, 2001b] was used in the PET-MR image registration. Due to the different fields of view of the MRA and PET images, a two-step image registration method was applied where MPRAGE images were also utilised as they have the same field of view as the PET images. Within modality registration, MPRAGE to MRA, was performed using translation (3 parameter) followed by a rigid registration (6 parameter) locally applied to masked carotid arteries. For the intramodal MRI registration, the correlation ratio was used as the cost function. For the cross-modal registration, the sum of earliest 6 PET frames (0-60 seconds) was computed to maximise the intensity in the arteries and was registered to the MPRAGE image using a rigid registration (6 parameter). Normalised mutual information was used to minimise the cost function. The combined matrix of these three transformations was used to resample PET frames onto MRA space. Each registration was visually confirmed by overlaying the segmented

carotid arteries on the registered PET frames.

PV effects in dynamic PET frames were corrected using the STC, where the binary mask of the segmented carotid arteries was used as the region of interest. A three-dimensional position-invariant isotropic Gaussian function with 6.8 FWHM was used to represent the PSF of the scanner. This PSF FWHM value was empirically derived from PET images by implementing the PSF measurement method by fitting a Gaussian function to line profiles across the carotid artery centroid points, as described in the simulation work section of this chapter (section 4.4.2). The method was applied to the two PET frames with highest arterial intensities (20 to 40 s) and the mean FWHM value between frames was calculated. This was repeated for all of the 19 subjects and the mean calculated FWHM is used in the PVC of all subjects (6.800.36 mm, range of 6.05 mm to 7.38 mm). Individual FWHMs are shown in figure 4.5. PVC was applied to each PET frame individually. The PVC algorithm was found to converge in 10 iterations, after which the mean intensity within the carotid arteries stopped changing significantly.

$$C_{blood} = HCT \cdot C_{RBC} + (1 - HCT) \cdot C_{plasma} \tag{4.6}$$

After correcting for PV effects, whole blood TAC was measured by computing the mean intensity within the segmented carotid arteries. In order to obtain the IDIF, whole blood concentration was converted to plasma concentration using a rearranged version of equation 4.6, where HCT represents measured haematocrit and C_{WB}, C_{RBC} and C_P represent the radioactivity concentration in whole blood,

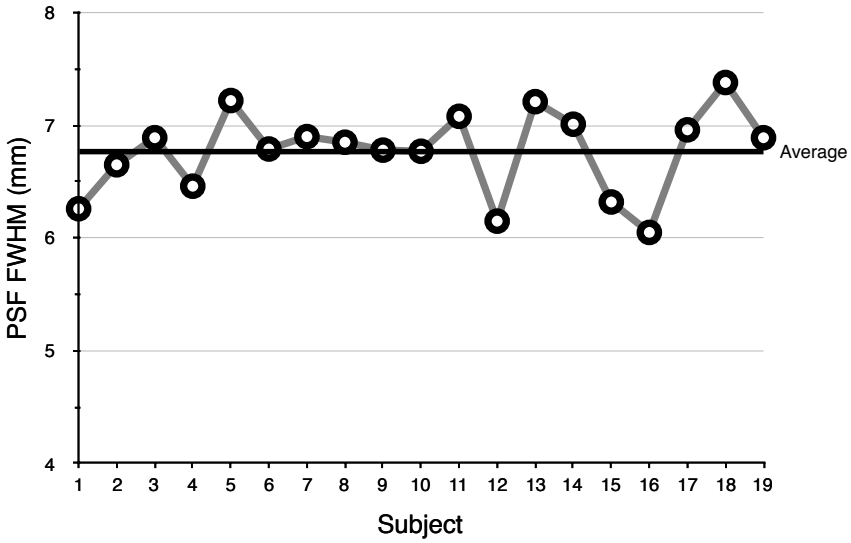

Figure 4.5: PSF FWHMs calculated for each subject

red blood cells and plasma respectively. A population based C_{RBC}/C_P relationship was used in this conversion [Phelps et al., 1979]. An example of derived plasma concentration to whole blood concentration is shown in figure 4.6.

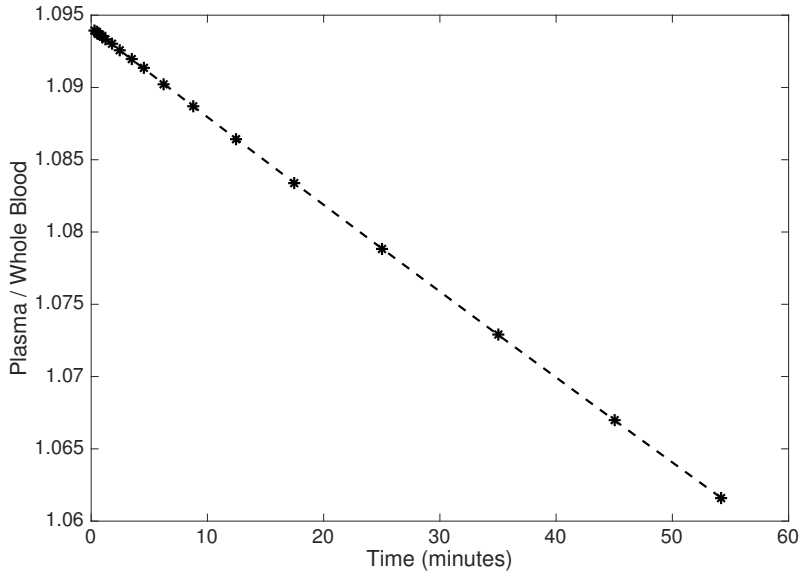

Figure 4.6: Concentration ratio of FDG tracer in blood plasma to that of whole blood for one subject, derived using rearranged version of equation 4.6. The linear curve was sampled for each second

As the arterial blood samples were taken from the radial artery, while the IDIFs

were obtained from carotid arteries, there was a time difference and dispersion between these two input functions. To make a fair comparison against arterial blood samples, delay and dispersion were applied to the measured IDIFs. Delay was added to the IDIF by shifting the curve to later times to match the tracer arrival times of IDIF and arterial samples. Then it was convolved with a monoexponential function to simulate dispersion. This was done in an optimisation to estimate the delay and time constant of dispersion that gave the best match between the subjects IDIF and arterial AIF peak shapes. This was performed for each subject independently and the averaged delay and dispersion values were used in the kinetic analysis. Finally, to see the effect of scaling, the measured IDIF curve with blood samples, the ratio between the mean of the last three arterial blood samples and the mean of the last three IDIF activities were calculated and the uncorrected and PV corrected IDIF curves were scaled using this ratio.

4.5.3 Performance Evaluation of Input Functions

In order to evaluate the performance of the derived IDIFs against the measured arterial input function of each subject, TACs from grey and white matters were fitted using both input functions. All PET kinetic analysis was done using PMOD (PMOD Technologies, Zurich, Switzerland). For each subject, 2 TACs were extracted using average grey matter and white matter activity and these were fitted using the 2-tissue compartment model with 3 rate constants (K_1, k_2, and k_3). The rate constant representing the transfer of tracer from metabolised state back to the unmetabolised state was assumed to be negligible (k_4=0). Cerebral blood volume (V_b) was also

estimated during the curve fitting. Using the estimated rate constants, cMRglc was computed for each input function.

In this analysis, the lump constant (LC) was set to be 0.89 [Graham et al., 2002] (Irreversible FDG model) and C_PG was measured by taking a blood sample from each subject before the PET scan. The input functions derived before partial volume correction ($IDIF_{Uncorrected}$), after partial volume correction ($IDIF_{PVC}$) and from plasma samples ($AIF_{samples}$) were fitted with the Feng input function model which consists of the sum of a gamma-variate function and two exponentials [Feng et al., 1993]. The performance of the proposed method was also tested by comparing the area under curve (AUC) of derived IDIFs to arterial samples. Paired students t-test was used to evaluate the statistical difference between AUC and cMRglc values calculated using $IDIF_{PVC}$ and $AIF_{samples}$ where a significance level of 0.05 was adopted throughout.

4.6 Results

4.6.1 Simulation results

Figure 4.7 illustrates the ratio of recovered intensity after partial volume correction to the true intensity within the carotid arteries for each iteration. The first value (iteration 1) represents the intensities before the PVC is applied and it can be seen that the PV effect increases when the difference between the carotid artery intensity and background intensity is increased. This is caused by the reduced relative spill-in effect from background tissues to the arteries as the intensity within the arteries is increased. When the PSF with 6.50 mm FWHM was used, which is identical

to the PSF used to blur the mask image in the phantom generation, the correction converged to a solution after ten iterations. As can be seen in 4.7a, at least 87.4% of the true intensity was recovered for all of the six phantoms.

PSF with 6.74 mm FWHM was found to give the smallest difference between the recovered and the true intensities across the all datasets. 4.7b shows the results when this optimal PSF was used and it can be seen that a better recovery was reached with this PSF where 92.9% of true intensity was recovered at minimum. A similar PSF FWHM value, 6.72 mm, was obtained when it was measured by drawing line profiles to carotid centroids of the reconstructed PET and MR images and results with this PSF is illustrated in figure 4.7c. At minimum, 92.4% of the carotid artery intensity could be recovered with this PSF.

Figure 4.8 shows the image-derived PSF values when the carotid arteries were under-segmented or over-segmented by one or two voxels in x and y directions. It can be seen that when the arteries were eroded by 2 voxels, a PSF FWHM of 6.91 mm was computed. On the other hand, when the arteries were dilated by 2 voxels in x and y directions, PSF FWHM of 6.38 mm was computed. A polynomial relationship was observed between the calculated PSF FWHM values as the carotid artery diameter was changed. The effect of using these erroneous PSF values on recovery performances of STC was illustrated in figure 4.9. As expected, smaller PSFs resulted in undercorrection of the activity and using PSF FWHM of 6.38 mm recovered only 88.9% of the true activity. On the other hand, using an overestimated PSF FWHM caused overcorrection of the activity where the mean intensity after PVC with PSF FWHM of 6.91 resulted was 105.8% of true activity. An approximately

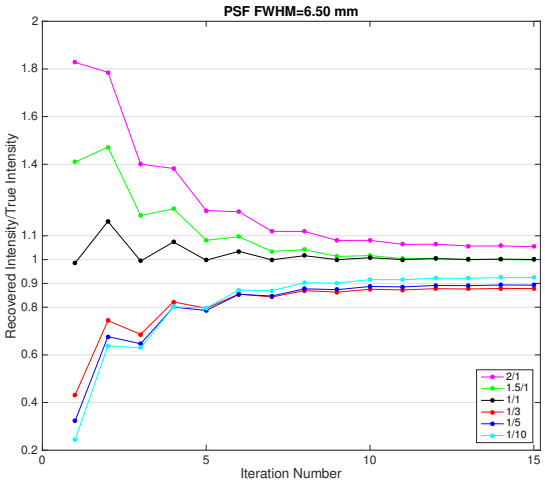

(a) 6.5 mm FWHM

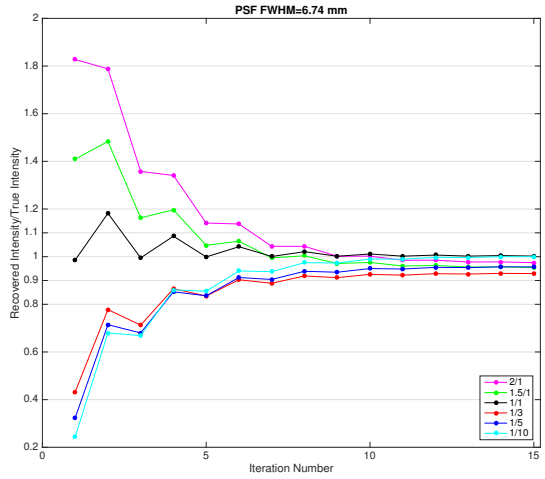

(b) 6.74 mm FWHM

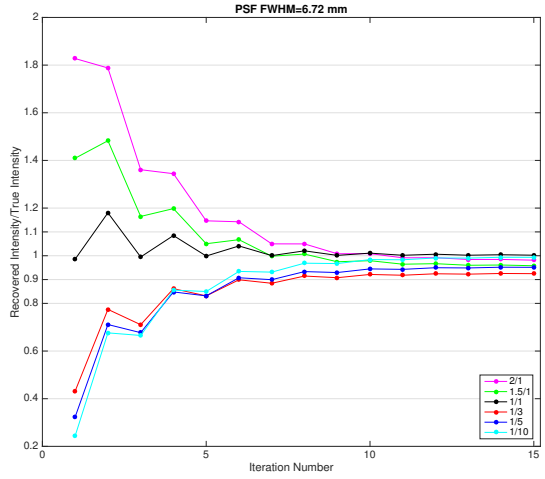

(c) 6.72 mm FWHM

Figure 4.7: Recovered intensity to true intensity ratios for each iteration of partial volume correction. Results are shown for 6 different background to carotid intensity ratios. (a) shows the result when PSF FWHM is 6.5 mm, (b) PSF is 6.74 mm and (c) 6.72mm

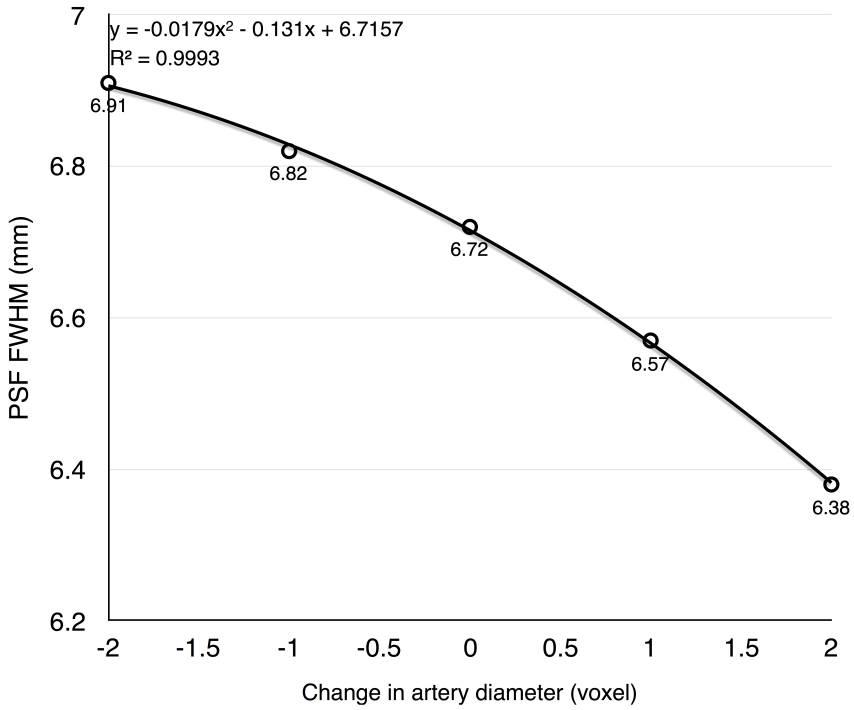

Figure 4.8: PSF FWHM calculated with segmentation errors where carotid arteries are eroded or dilated by adding or removing 1 or 2 voxels to its diameter. Negative changes represents the under-segmented arteries where positive changes represent over-segmentation. Voxel size is 0.391 x 0.391 mm.

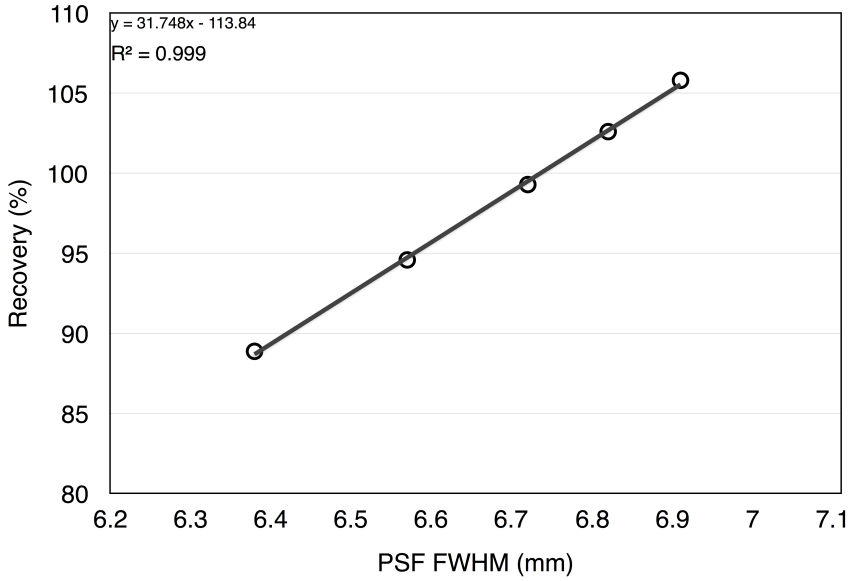

Figure 4.9: Effect of using different PSF FWHM values on the PVC performance. Recovery of true intensity value is shown in percentages

linear relationship was observed between the PSF FWHMs and recovered intensity to true intensity percentage ratios.

4.6.2 ^{18}F-FDG results

The mean value for prescan blood glucose was 5.07 mmol/L (4.3-5.7 mmol/L) and average haematocrit was 41% (36-45%). Figure 4.9 shows the $IDIF_{PVC}$ derived from one subject plotted together with $IDIF_{Uncorrected}$ and $AIF_{Samples}$ as well as $IDIF_{PVC}$ and $IDIF_{Uncorrected}$ scaled with blood samples. It can be seen that application of the PV correction increases the intensities both at early and late parts of the input function. The tail of the $IDIF_{PVC}$ (after 3 minutes) was well matched with $AIF_{Samples}$ which shows that the PVC method worked successfully to recover the accurate intensity values within the carotid arteries. The first frames of the $IDIF_{Uncorrected}$ and $IDIF_{PVC}$ after the delivery of the tracer showed a much higher difference where the PVC increased the peak of the input function by 300% in average. After PVC, a close match between $AIF_{Samples}$ and $IDIF_{PVC}$ peak shapes was observed (figure 3b). The AIFs plotted in figure 4.9 were corrected for delay and dispersion effects. Across the 19 subjects, an average time shift of 9.49 seconds was observed between the peaks of these two input functions. The average dispersion time constant was computed as 4.70 seconds between the carotid artery and radial artery time activity curves.

Comparison of the computed AUC values for each of the three input function curves was illustrated in figure 4.11. The mean and standard deviation of AUC values in MBq.min/mL was 15.5 $\pm$ 2.0 for $IDIF_{Uncorrected}$, 19.7 $\pm$ 2.0 for

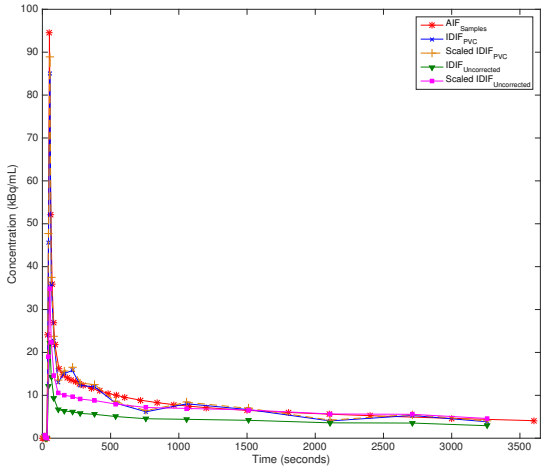

(a)

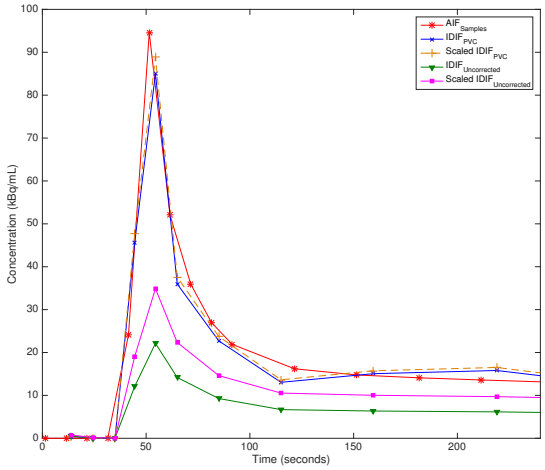

(b)

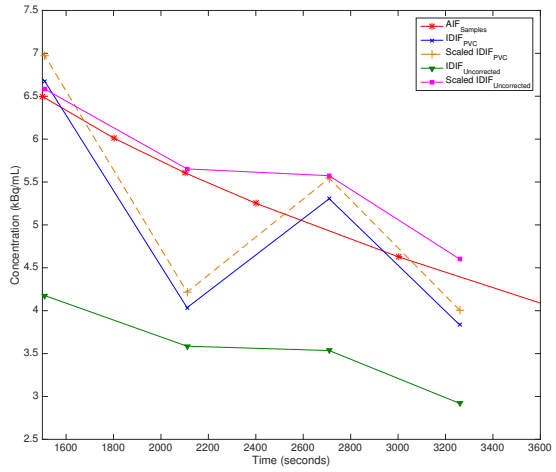

(c)

Figure 4.10: (a) $IDIF_{Uncorrected}$, $IDIF_{Uncorrected}$ scaled with blood samples, $IDIF_{PVC}$, $IDIF_{PVC}$ scaled with blood samples,and $AIF_{Samples}$ plotted together for one subject. (b) Input function curves plotted for first 4 minutes only to show the peaks. Dispersion was added to $IDIF_{PVC}$ and $IDIF_{Uncorrected}$ curves. (c) Input function curves plotted for last 30 minutes.

$IDIF_{Uncorrected}$ scaled with blood samples, 26.0 $\pm$ 2.9 for $IDIF_{PVC}$, 22.7 $\pm$ 2.8 for $IDIF_{PVC}$ scaled with blood samples and 26.8 $\pm$ 2.6 for $AIF_{Samples}$. In all of the 19 subjects, $IDIF_{Uncorrected}$ had significantly lower AUC values (paired t-test, p <0.0001), which confirms the underestimation of the input function due to PV effects. It was seen that applying the PVC brought the area under the IDIF curve to a good agreement with the $AIF_{Samples}$. Comparing the area under the $IDIF_{PVC}$ and $AIF_{Samples}$ for each subject, there was no statistically significant difference between AUC of these curves with a p value of 0.16. AUC of $IDIF_{PVC}$ scaled with late blood samples was also found to be significantly different from $AIF_{Samples}$ (p <0.001).

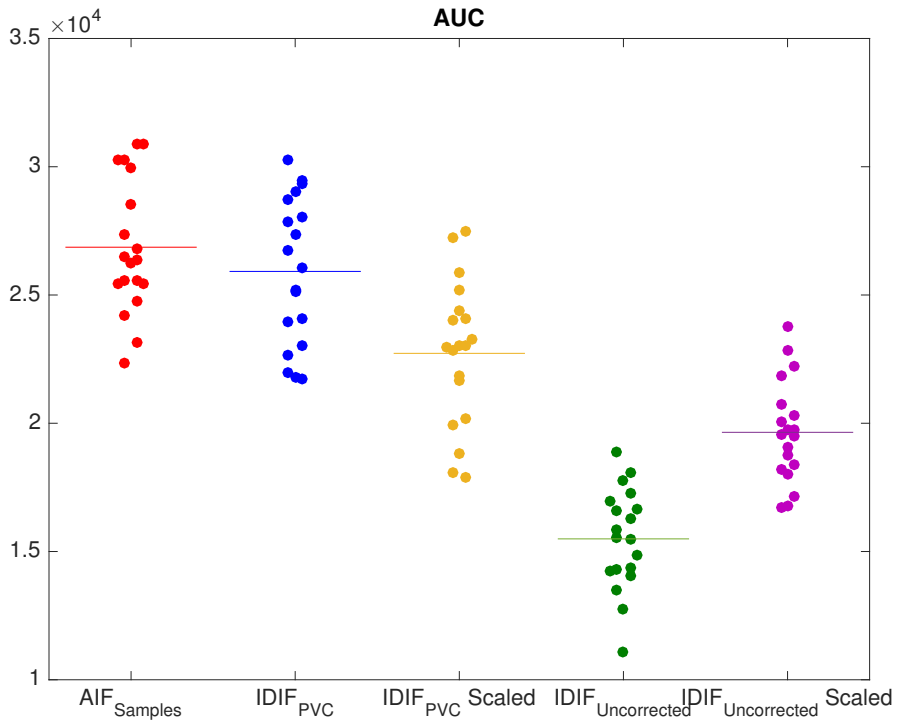

Figure 4.11: Area under curves (AUCs) of $AIF_{Samples}$, $IDIF_{PVC}$, $IDIF_{PVC}$ scaled with blood samples, $IDIF_{Uncorrected}$, and $IDIF_{Uncorrected}$ scaled with blood samples Dots represent individual AUCs and lines represent the mean AUC across the group

Table 1 and 2 lists the summary of the kinetic parameter and cMRGlc re-

sults estimated for grey matter and white matter using $IDIF_{Uncorrected}$, $IDIF_{PVC}$ and $AIF_{Samples}$. When $IDIF_{Uncorrected}$ was used, cMRGlc in grey matter was overestimated by 50.9% on average compared to the estimates with $AIF_{Samples}$. Similarly, cMRGlc in white matter was overestimated by 45.4% when $IDIF_{Uncorrected}$ was used. Using the $IDIF_{PVC}$ largely improved the estimates, bringing the average absolute error to 5.6% and 7.5% respectively. Performing a paired t-test on the results obtained with $IDIF_{PVC}$ and $AIF_{Samples}$ showed no statistically significant difference for both regions ($p=0.12$). Bland-Altman plots of individual cMRGlc estimates for white and grey matter are shown in figure 4.12, illustrating that there was no consistent bias in the produced white matter results. However, there is a statistically significant positive trend in the grey matter cMRGlc results (Pearson correlation, $p < 0.005$). At present, this effect remains unexplained.

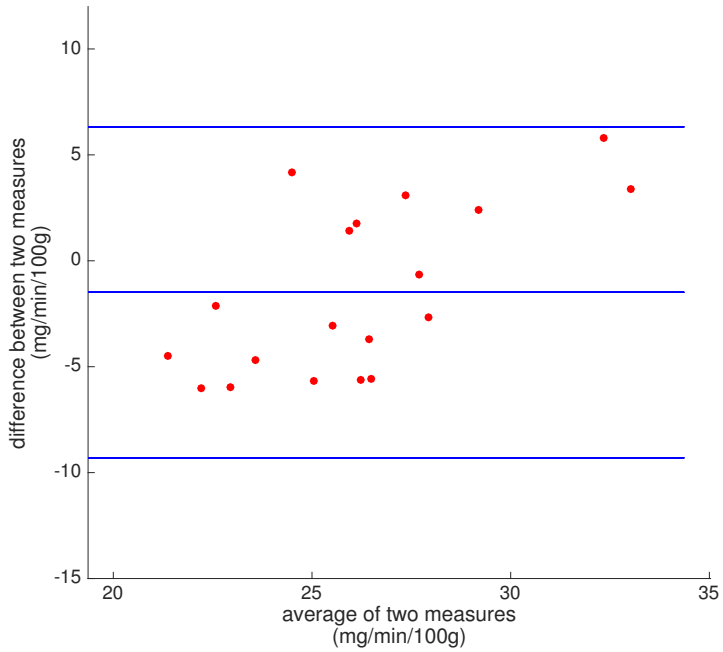

(a) Grey matter

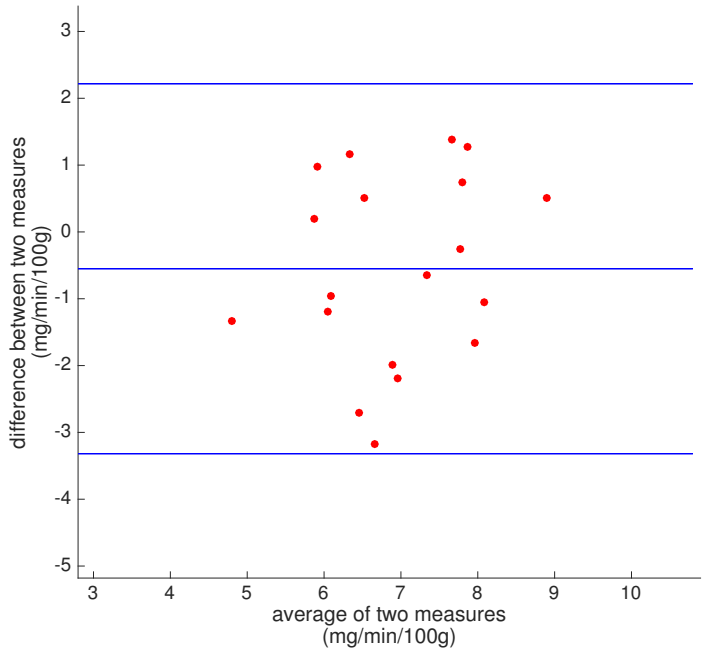

(b) White matter

Figure 4.12: Bland-Altman Plots of cMRglc estimates with arterial blood samples and PV corrected IDIF for (a) grey matter and (b) white matter.

Table 4.1: Mean value and standard deviation of kinetic parameters and cMRglc estimates for grey matter calculated using arterial samples, PV corrected IDIF, PV corrected IDIF scaled with blood samples, uncorrected IDIF and uncorrected IDIF scaled with blood samples for 19 subjects. The symbol * indicates parameters with significant difference to arterial samples (paired t-test, $p < 0.05$).

Grey Matter							
	V_b	K_1	k_2	k_3	K_1/k_2	K_i	cMRglc
Blood AIF	0.059 ± 0.019	0.123 ± 0.014	0.121 ± 0.045	0.079 ± 0.023	1.175 ± 0.581	0.049 ± 0.004	26.88 ± 2.36
PVC IDIF	0.050 ± 0.020	$*0.149 \pm 0.022$	0.124 ± 0.044	$*0.056 \pm 0.025$	1.323 ± 0.490	0.046 ± 0.008	25.38 ± 4.66
Scaled PVC IDIF	0.050 ± 0.020	$*0.166 \pm 0.038$	0.118 ± 0.044	$*0.053 \pm 0.024$	$*1.592 \pm 0.645$	0.049 ± 0.005	26.95 ± 2.92
Uncor. IDIF	$*0.076 \pm 0.015$	$*0.427 \pm 0.098$	$*0.219 \pm 0.063$	$*0.046 \pm 0.007$	$*2.017 \pm 0.429$	$*0.074 \pm 0.009$	$*40.56 \pm 4.82$
Scaled Uncor IDIF	$*0.101 \pm 0.022$	$*0.325 \pm 0.070$	$*0.220 \pm 0.070$	$*0.047 \pm 0.008$	$*1.531 \pm 0.293$	$*0.057 \pm 0.007$	$*31.35 \pm 3.91$

Table 4.2: Mean value and standard deviation of kinetic parameters and cMRglc estimates for white matter calculated using arterial samples, PV corrected IDIF, PV corrected IDIF scaled with blood samples, uncorrected IDIF and uncorrected IDIF scaled with blood samples for 19 subjects. The symbol * indicates parameters with significant difference to arterial samples (paired t-test, $p < 0.05$).

White Matter							
	V_b	K_1	k_2	k_3	K_1/k_2	K_i	cMRglc
Blood AIF	0.029 ± 0.008	0.044 ± 0.009	0.092 ± 0.030	0.040 ± 0.013	0.512 ± 0.125	0.013 ± 0.002	7.22 ± 1.10
PVC IDIF	0.027 ± 0.010	$*0.054 \pm 0.012$	0.101 ± 0.032	$*0.030 \pm 0.009$	0.573 ± 0.136	0.012 ± 0.003	6.68 ± 1.35
Scaled PVC IDIF	0.027 ± 0.008	$*0.061 \pm 0.014$	0.096 ± 0.024	$*0.027 \pm 0.009$	$*0.655 \pm 0.157$	0.013 ± 0.002	7.26 ± 1.07
Uncor. IDIF	$*0.038 \pm 0.008$	$*0.151 \pm 0.037$	$*0.181 \pm 0.040$	$*0.027 \pm 0.006$	$*0.850 \pm 0.180$	$*0.019 \pm 0.004$	$*10.50 \pm 1.89$
Uncor. IDIF scaled	$*0.048 \pm 0.010$	$*0.114 \pm 0.028$	$*0.179 \pm 0.041$	$*0.027 \pm 0.006$	$*0.652 \pm 0.015$	$*0.015 \pm 0.003$	$*8.05 \pm 1.16$

For individual kinetic parameter estimates, using the $IDIF_{Uncorrected}$ overestimated the K_1 parameter by 247.0% on average for grey matter and white matter. This error was reduced to 21.0% and 22.7% after the PVC. There was no statistically significant difference on the k_2 parameter values produced with $IDIF_{PVC}$ and $AIF_{Samples}$ (p=0.98). On the other hand, using the $IDIF_{Uncorrected}$ underestimated k_3 values but $IDIF_{PVC}$ reduced this difference by a factor of two, similar to the improvement seen for k_2 results. $IDIF_{PVC}$ was able to return V_b, k_2 and cMRGlc values with no significant differences.

Using three arterial blood samples to scale the $IDIF_{PVC}$ slightly improved the mean of cMRGlc estimates, with an average absolute percent difference of 0.3% and 1.5% and no statistically significant difference (p=0.93 and p=0.72) against $AIF_{Samples}$ for grey and white matter respectively. Scaling increased the error on the K1 parameter, with 35.0% and 38.6% error against the $AIF_{Samples}$. Similar to $IDIF_{PVC}$ results, scaled $IDIF_{PVC}$ was able to return Vb, k2 and cMRGlc with no significant difference to AIFSamples. Scaling the $IDIF_{Uncorrected}$ with blood caused an improvement on the cMRGlc estimates. However, there was a significant difference between scaled $IDIF_{Uncorrected}$ and $AIF_{Samples}$ cMRGlc estimates ($p < 0.01$). Furthermore, it yielded large errors on the individual kinetic parameter estimates.

4.7 Discussions

Simulated data results showed that STC can be accurately applied to regions with different region-to-background activity ratios and can correct for spill-in and spill-out effects reliably. It was observed that using a PSF with a larger FWHM than the

PSF used in the simulation of datasets resulted in a more accurate PV correction. This indicates that further blurring was caused by the forward-projection, reconstruction and resampling of the data, mainly due to interpolation effects caused by these processes. A PSF FWHM value closer to the optimal value could be accurately measured from the reconstructed PET images and using this PSF resulted in similar recovery performance for all of the datasets. This indicates that a reliable PSF can be measured from reconstructed PET images if the true shape and size of the region of interest is known.

Due to the small diameter of carotid arteries, IDIFs directly estimated from reconstructed PET frames are severely affected by the partial volume effects. Results from this study show that such IDIFs have significantly lower tracer concentration even when the arterial VOIs are delineated from high-resolution MR anatomical images. Errors caused by partial volume effects are especially observed in the early frames, where the peak of the input function is highly underestimated. Performing a partial volume correction greatly improved the recovery of signal intensities within the carotids and a good visual agreement was observed against input function curves acquired from serial arterial sampling. Using the PV corrected IDIFs also yielded a good agreement between the estimated cMRGlc values with the arterial samples. Scaling the PV corrected IDIF with late blood samples resulted in smaller AUC values compared to the arterial samples. This can be due to the variation of the error in the PV correction at different time points as the early frames are more affected from spill-out effects than later time points. Therefore a single scaling constant measured at the latest part of the curve may not be sufficient to calibrate the

whole input function.

In this work, we have used a novel image-based partial volume correction method in the IDIF estimation. This method only requires an accurate segmentation of the region of interest, which is the carotid artery in this application. This eliminates the need for complete parcellation of the image into separate regions, which is a necessary step for most image-based partial volume correction methods to operate [Rousset et al., 1998b] [Erlandsson et al., 2012b], or even definition of representative background regions [Zanotti-Fregonara et al., 2009b]. Therefore, here we have implemented a more practical PV correction method for the purpose of IDIF measurements.

The performance of the presented method highly depends on the accuracy of segmentation, image registration and point spread function estimation. As presented here, time of flight MR angiography images can be easily used to segment carotid arteries as they clearly distinguish signal coming from inflowing blood compared to neighbouring voxels. Typical T1-weighted MPRAGE images have larger voxel size which can affect the accuracy of the segmentation of internal carotid arteries with small diameter. Furthermore, background regions neighbouring the carotid arteries have higher intensity on MPRAGE images and can interfere with the region-growing algorithm. We attempted to apply the same segmentation method on the MPRAGE images but observed discontinuities in the segmented arteries and leakage to background tissues. MR Angiography is now routinely performed in many clinical and research brain imaging studies and a high resolution 3D MR angiography image of the carotid region can be easily acquired.

This method can be also be applied to other body parts where a suitable arterial structure is within the field of view. For instance, the proposed method has been used to derive IDIF in Rubidium-82 colorectal PET studies where the femoral arteries were segmented from higher resolution CT perfusion images [Dickson et al., 2015]. Similarly, STC was applied to correct for the PV effects present on the PET images and IDIF was computed using the proposed technique. The derived AIFs were not compared against the gold standard AIF due to lack of arterial samples, but a significant increase in the IDIF peaks was observed after the PVC was applied. The authors of that work confirmed that application of the proposed method to derive the AIF substantially corrected for spill-in and spill-out effects seen in different PET frames and induced a significant change in the estimated K_1 parameter values.

Mismatches in the PET/MR registration can lead to errors in the measured IDIF curves as they may cause inclusion of signal from non-arterial voxels in the measurement. In order to minimise the errors caused by misregistration, we developed a two-step registration method and alignment of carotid arteries was visually inspected for each dataset. However it is likely that small mismatch errors were present in these data since the PET and MRI images were acquired on separate scanners and patients may have had different head positioning across scans, making the registration step more problematic. Using a simultaneous PET/MRI system is likely to improve the performance of IDIF extraction as it could reduce co-registration errors.

IDIF methods including our proposed method are vulnerable to subject motion during the dynamic PET and MR scans. Subject motion during the MR angiography

acquisition can distort the shape of the arteries and lead to errors both in carotid artery segmentation and registration. Interframe motion in the PET data can cause the carotid arteries to change location between the frames, causing mismatch to the coregistered mask image and hence inconsistence in the measured TACs. Such effects can cause underestimation of the IDIF and lead to overestimation of the cMRGlc parameter. Mourik et al. [Mourik et al., 2011] simulated motion effects and compared IDIFs with motionless IDIFs. Results of this simulation work showed that when patient motion is more than 6° rotation or 5 mm axial translation after the first 10 minutes of the scan, at least 10% overestimation or underestimation of the V_T was observed. Zanotti-Fregonara et al. [Zanotti-Fregonara et al., 2012] evaluated the effects of simulated translational and rotational motion on IDIFs and observed a difference in the AUC of the IDIFs compared to the motionless measurements of up to 19% for rotations and 66% for translations. However, the errors were found to be less than 10% in clinical scans without any motion correction. Authors concluded that motion artefacts only minimally affect IDIF estimation in brain PET imaging. However, in the presence of motion, blood samples could be used to scale the IDIF.

External markers can be placed onto the subject's head to track the possible head movements. However, such methods usually require an external device and require a clear view of the markers placed on the head [Fulton et al., 2002]. With the help of PET/MRI scanners, simultaneously acquired MR data can be used to perform motion tracking and correct dynamic PET frames for motion effects. This can be done by repeatedly acquiring anatomic volumes using fast MRI navigator sequences, such as EPI, and coregistering these images to correct for any motion

which can happen between acquisitions [Catana et al., 2012]. This information can be then utilised to correct motion in the simultaneously acquired dynamic PET data [Keller et al., 2015] [Catana et al., 2011]. Such techniques can enable us to minimize the motion artefacts between the PET frames and the reference MRI image used for the carotid artery segmentation. Application of a reliable motion correction method will hence enhance the accuracy of the proposed IDIF method in the presence of significant subject motion.

One limitation of this study was the arterial blood sampling protocol used to obtain the arterial input function. AIF was sampled for every 10 seconds for the first two minutes, which might cause errors in the definition of the AIF peak. The sampling thereby closely matches the initial framing. However, the measured AIFs and IDIFs were fitted with an analytical input function model in the kinetic analysis which could reduce the negative effects caused by the sampling protocol. During the AIF fitting, we took into account the fact that each blood samples was taken over a 3 second period, while the IDIF represented an average over each PET frame duration. The accuracy of the IDIFs would depend on the accuracy of segmentation, registration and PSF measurement methods, while the AIF could be affected by issues related to the blood sampling. These can be possible explanations for the significantly different K_1 and k_3 parameters.

A small time difference between the peaks of the $IDIF_{PVC}$ and $AIF_{Samples}$ was observed which can be caused by different PET tracer arrival times to the carotid arteries and the radial artery, tubing used in arterial sampling and variation in blood velocity in different arteries. This time difference in AIF peaks may also introduce

errors in the estimated kinetic parameter values. There are several methods present in the literature to correct arterial samples for these time delay and dispersion effects [Meyer, 1989] [Iida et al., 1988], but in this case we have chosen not to modify the gold standard arterial blood sample curve. Therefore, in order to make a fair comparison, time delay and dispersion were applied to the measured IDIFs instead. It could be argued that due to its proximity to brain tissues, an IDIF measured from carotid arteries, corrected for PV effects, might be a more accurate representation of the input function in brain kinetic analysis than arterial samples obtained from a radial artery.

There was a good agreement between $IDIF_{PVC}$ and $AIF_{Samples}$ in terms of the macro-parameter K_i. However, the micro-parameters K_1 and k_3 were significantly different. This may suggest that, when using $IDIF_{PVC}$, the outcome values should be restricted to K_i, in which case it would be possible to use a simple Patlak analysis [Patlak et al., 1983] [Graham et al., 2002], obviating the need for full kinetic modelling. On the other hand it is not entirely clear which set of estimated microparameters are closer to the true values. The K_1, k_2, k_3 and cMRGlc values obtained with our method are well within the range of previously published values for grey matter tissues in healthy subjects (K_1: 0.068-0.161), k_2: 0.071-0.301, k_3: 0.03-0.10, cMRGlc: 28.60 ± 4.73) [Yushkevich et al., 2006].

The ultimate goal of this work is to provide a non-invasive and practical way of measuring the input function from PET images and eliminate the need for arterial sampling in clinical practice. The method was validated in healthy subject ^{18}F-FDG studies but can be extended to analyse patients with various disorders. For

instance, ^{18}F-FDG PET tracer can be used in Dementia studies to calculate the hypometabolism by comparing estimated cMRGlc values to healthy subject values. On average, approximately 12% reduction in cMRGlc values is observed in subjects with dementia [Chawluk et al., 1990] [Ishii et al., 1997] [Mosconi et al., 2009]. Based on the grey matter cMRGlc results presented in this chapter, a sample size of 17 will be required to detect the 12% difference between the control and dementia subject's cMRGLc values with a power of 0.80. On the other hand, 6 subjects will be needed to be included in each of the patient and control groups when blood sample derived AIFs are used.

4.8 Conclusions

In conclusion, the proposed IDIF estimation technique, which uses STC to correct for contamination from neighbouring tissues, only requires the segmentation of the carotid arteries with no separate need for parcellating the background region. The carotid arteries were segmented using MR angiography images with excellent vessel contrast. The proposed method does not require any arterial or venous blood samples to be used in PV correction and curve scaling. Results were validated against AIFs determined from serial arterial blood samples and no significant difference was seen in the area under input function curves and estimated cMRGlc values. Only two of four microparameters could be retrieved with no significant differences. However, the cerebral metabolic rate of glucose consumption (cMRGlc) parameter, which is usually the main parameter of interest in ^{18}F-FDG, was derived accurately with no significant difference to arterial samples. These results

indicate that the proposed method can be used as a practical alternative to measure the blood signal in the carotid arteries with no need for arterial or venous blood sampling.

Chapter 5

Exploiting Prior Information in the PET SIME Method

5.1 Introduction

The simultaneous estimation (SIME) method is a non-invasive image-based method to perform kinetic analysis of dynamic PET data. In this method, the input function is expressed as a mathematical function in which parameters are estimated together with the kinetic parameters. SIME requires time activity curves from different regions with various kinetic behaviours and each region is modelled using a tissue compartmental model. Assuming that the input function is uniform across the regions, the AIF is estimated simultaneously with the kinetic rate constant parameters for each region. SIME usually requires a blood sample, or another scaling factor to normalise the estimated input function and ensure model identifiability. SIME is fully described in detail in the next section.

An accurate measurement of the input function is also essential in the analy-

sis of dynamic-susceptibility contrast (DSC) MRI and dynamic contrast enhanced (DCE) MRI data. In these techniques, the injected bolus of gadolinium-based contrast agent causes a signal drop on T_2 and T_2^* weighted images and a signal rise on T1 weighted images. These signal changes can then be used to derive the concentration of the contrast agent in the plasma. Estimation of the input function can have some advantages in MRI, due to its higher spatial and temporal resolution. For most PET tracers with neglected uptake in the lungs, the early peak of the input function mainly describes the delivery of the PET tracer to the tissue of interest and is dominated by the cardiac output and blood flow. The same applies to the delivery of the Gd contrast agent. Therefore, if the PET data and MRI data are obtained at the same time, similarities are expected to be seen in the early parts of the PET-AIF and MRI-AIF. Hence, the early part of an MRI-AIF can be used to obtain some prior information about the bolus shape of the input function, which can be incorporated in the SIME method. In addition, in cases where IDIF methods can not be used non-invasively to measure the AIF (i.e. due to presence of radiometabolites in blood plasma), the whole blood TAC, which can be noninvasively derived from PET images using the methodology presented in Chapter 4, can be used to obtain prior information regarding the AIF.

This chapter presents details of our approach to utilise prior information within the SIME method. A simulation study was performed to evaluate the effects of injecting this prior information on the accuracy of estimated kinetic parameters. The method was tested with simulated ^{18}F-FDG and results were compared with or without the prior information and different AIF scaling methods against the known true

AIF. An inter-subject analysis was performed by simulating TACs using published kinetic parameters from different studies. Results have shown that incorporating the prior AIF information within the simultaneous estimation significantly improved the bias on estimated K_i values. The overview of the constrained SIME implementation is illustrated in figure 5.1.

5.2 Literature Survey

The SIME method was introduced by Feng et al. in 1997 [Feng et al., 1997], as an alternative method to perform non-invasive quantitative analysis of dynamic PET data. The method was tested using Monte Carlo simulation and it was concluded that a reliable estimation of cMRGlc could be obtained in FDG studies in the presence of at least three ROIs with different kinetics. Wong et al. [Wong et al., 2001] used a modified version of SIME, called simultaneous estimation with post-estimation (SIMEP), where the input function estimated by SIME was used to individually fit each TAC as a second step to obtain the kinetic parameters. The authors showed that the standard deviation of the parameter estimations was improved when SIMEP was used and SIMEP provided similar results to those obtained by arterial samples. Wong et al. also presented another modified version of SIME where they replaced nonlinear least squares with a Monte Carlo method called simulated annealing in the minimisation of the cost function [Wong et al., 2002]. The main benefit of using simulated annealing was to avoid the local minima problems that the nonlinear least squares method can face during optimisation. The method was tested with simulated dynamic SPECT data with ^{99m}Tc-teboroxime which has faster

kinetics compared to ^{18}F-FDG. The authors showed that using simulated annealing improved the accuracy of the estimated input function and physiological parameters, and yielded more similar AIF and kinetic parameter estimates than nonlinear least squares method. The simulated annealing method also was less sensitive to noise than the nonlinear least squares method. It was concluded that simulated annealing can be a better method to use with tracers that are critically dependent on the shape of the input function.

In later work, Guo et. al [Guo et al., 2007] tried to obtain the early peak of the input function during the first 40 seconds, from an image-based PET carotid artery measurement and used this information together with three venous plasma samples obtained towards the end of the study to improve the SIME method. A voxel clustering method was used in their method to obtain TACs from three regions with varying kinetic behaviour. The results showed that their proposed model was able to recover the AIF with good performance. They observed K_i estimates with no significant difference estimated with the proposed method and gold standard arterial samples. In similar work, Sanabria-Bohorques et al. used three arterial samples to calibrate an IDIF derived from [^{11}C]-Flumazenil PET studies [Sanabria-Bohórquez, 2003] and estimated the shape of the early AIF peak using SIME with various TACs from various brain regions. A good agreement with AIFs derived from arterial samples was observed. Both AIFs also yielded correlated V_T estimates.

Ogden et al. [Ogden et al., 2010] used SIME to analyse various PET tracers including ^{18}F-FDG and three [^{11}C] labelled tracers which typically require metabolite analysis. Simulated annealing was used in the optimisation of the cost function.

Their results showed that SIME with simulated annealing was a promising alternative to non-invasively perform kinetic analysis of dynamic PET data for 4 different PET tracers. Similar results to arterial samples were obtained using the proposed method. However, at least one plasma sample was required to ensure the identifiability of the solution. Even though this is more practical than performing full arterial sampling, it still requires the complications of obtaining plasma concentration and correcting for metabolites. In 2005, Zanderigo et al. [Zanderigo et al., 2014] presented an extended version of this method where the need for an arterial sample for AIF normalisation was substituted with a non-invasive measurement. Instead of using a single blood sample, they used an anchor value which can noninvasively computed using multiple linear regression on variables such as injected tracer dose, body mass index and/or body surface area. They observed that using tracer dose and body mass index gave the best performance. The proposed method was able to estimate V_T and binding potentials non-invasively with a comparable performance to full kinetic analysis with arterial blood samples. Their proposed method was successfully validated in CUMI studies [Shrestha et al., 2014] but was claimed to be applicable for other tracers. SIME has also been successfully applied to analyse DCE-MRI datasets [Irving et al., 2013]

5.3 Simultaneous Estimation Method (SIME)

The outline of the SIME method is illustrated in figure 5.1. In this example, three TACs extracted from different brain regions were used and each region was modelled using a two tissue compartment model with 4 rate constants. It is assumed

that the AIF is same across all of the brain regions. The AIF is modelled using a mathematical model, whose parameters define the curve shape.

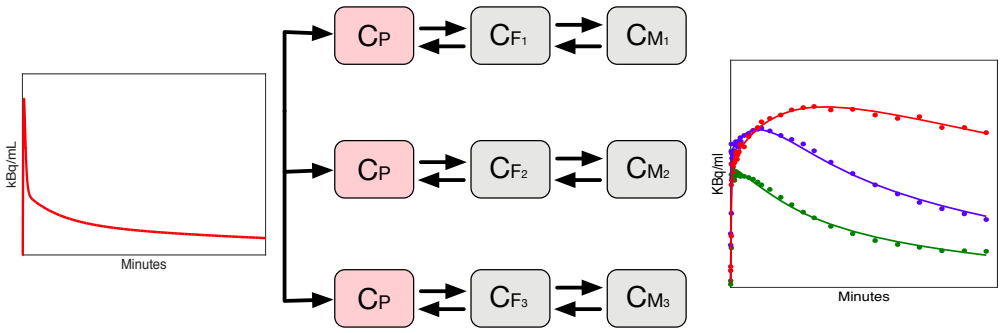

Figure 5.1: Schematic diagram of simultaneous estimation approach using two tissue compartment model. Time activity curves from different ROIs are incorporated together with AIF parameters in the objective function to be optimised.

$$C_p(t) = (A_1 t - A_2 - A_3)e^{-\lambda_1 t} + A_2 e^{-\lambda_2 t} + A_3 e^{-\lambda_3 t} \tag{5.1}$$

In the original SIME method, Feng et al. [Feng et al., 1997] used Feng's input function model [Feng et al., 1993] with 6 parameters as shown in equation 5.1, where λ_1, λ_2 and λ_3 are the eigenvalues of the model and A_1, A_2 and A_3 are the coefficients of the model. This model is the sum of a gamma variate function which describe the bolus of the AIF with two exponentials which represent the late washout phase.

In the kinetic model, the impulse response of 2-TC model was convolved with the AIF model to create the cost function to be optimized, as shown in equation 5.2. K_1,k_2, k_3 and k_4 represent the kinetic rate constants for each region and V_b is the cerebral blood volume for each region, which represents the amount of activity in the vascular space present in that region. The activity in the cerebral blood

volume adds to the signal measured from the tissue of interest and therefore needs to be taken into account during kinetic analysis, which can be performed using the relationship in equation 5.3. Contribution of this activity is linked to the amount of tracer in the whole blood.

$$C_i = \sum_{i=1}^{N} \sum_{i=1}^{M} [C_P(t) \otimes h_i(k_1, k_2, k_3, k_4, V_b; t)] \tag{5.2}$$

$$C_T(t) = (1 - V_b) C_i(t) + V_b C_{wb}(t) \tag{5.3}$$

The 6 parameters of the AIF model and the 5 parameter of each ROI (K_1,k_2, k_3,k_4,V_b) were fitted simultaneously. In SIME, at least one blood sample is often used to normalise the estimated AIF. In the original method [Feng et al., 1997], Feng et al. proposed withdrawing three arterial blood samples towards the end of the study and fit an exponential function through them to get the parameter values of A_3 and λ_3. AIF scaling using the blood samples was shown to improve the robustness of the method.

One drawback of SIME is its computational complexity, as a large number of parameters are estimated at once. As part of this work, we try to incorporate prior information about the early part of an input function which can be derived from another source (i.e. image derived blood signal or MRI-derived AIF) to reduce the number of estimated parameters in the SIME.

Table 5.1: True values of the kinetic parameters used to generate the three time activity curves

	Grey Matter	White Matter	Tumour
K_1 (mL/cm^3/min)	0.041	0.023	0.028
k_2 (1/min)	0.120	0.073	0.087
k_3 (1/min)	0.064	0.034	0.047
k_4 (1/min)	0.0075	0.0098	0.0084
K_i (mL.cm^{-3}/min)	0.0143	0.0073	0.0098
V_b (mL/100g)	5.80	2.50	4.40

5.4 Simulation work

In this section, work done to see the effect of including prior information about the early part of input function derived from another source on the performance of SIME is presented. An experiment is designed with simulated ^{18}F-FDG data and the results are compared to true values used in the simulation. The effect of fixing the λ_1 parameter in the AIF model to its true value is evaluated by studying the bias on the estimated kinetic parameters.

5.4.1 Materials and Methods

The command line interface of Compartment Model Kinetic Analysis Tool (COMKAT) [Muzic and Cornelius, 2001] was used to generate the simulated data, set up the model, and perform the parameter optimisation. COMKAT is a free, open source kinetic modelling software package, written using MATLAB and provides ready-made kinetic modelling functions as well as a graphical user interface to analyse dynamic PET images.

In our model, Feng's parametric input function (eq 5.1) was used with his published average values ($A_1 = 851.1225$, $A_2 = 21.8798$, $A_3 = 20.8113$ in $\mu C_i/mL$ and $\lambda_1 = 4.1339$, $\lambda_2 = 0.1191$, $\lambda_3 = 0.0104$ in 1/min). No time delay was assumed in the arrival of the PET tracer. Kinetic rate constant and cerebral blood volume values from a published brain study were used to generate time activity curves of different brain regions [Hawkins and Huang, 1986] as listed in table 5.1. A two tissue compartment model was used in modelling, hence the total measured PET activity was computed using equation 5.2. The TACs of different regions were sampled at 29 time points, consisting of 6x5 sec scans, 2x15 sec scans, 6x30 sec scans, 3x2 min scans, 2x5 min and 10x10 min scans.

$$\sigma(t) = \sqrt{\frac{\eta^2 x C_T(t)}{\Delta t_k}} \tag{5.4}$$

Gaussian noise was added to TACs using equation 5.4 where C_T is the total measured PET activity, Δt_k is the frame duration and η is the scaling factor used to set the noise level added to the data [Landaw and DiStefano, 1984]. In this work, η was set to 0.5, 2 and 4. This noise model was multiplied with a pseudorandom number generator, using MATLAB's *randn* function, to randomise the generated noise. 50 realisations were created for each of these three noise levels. Examples of resulting TACs for three regions are plotted in figure 5.2 for different noise levels.

The SIME cost function includes common input function parameters between all regions, together with kinetic parameters from different ROIs, which are estimated simultaneously. The cost function can be written as equation 5.5. The *fmin-*

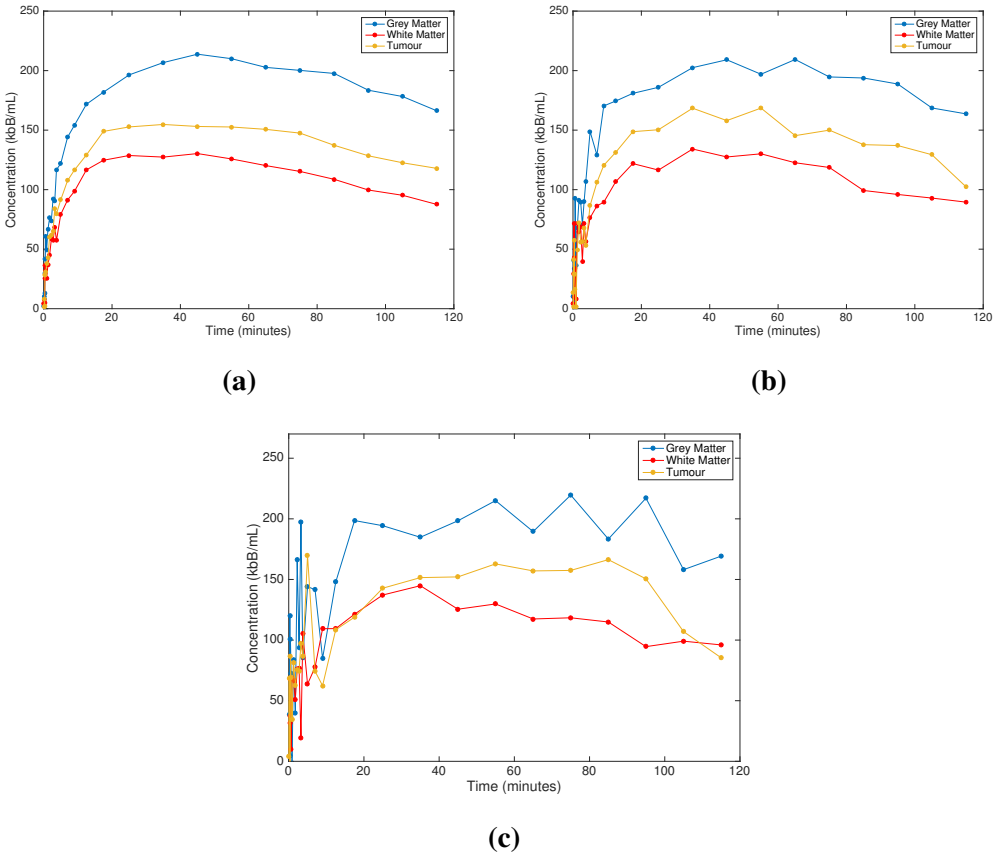

Figure 5.2: Simulated time activity curves for grey matter, white matter and tumour regions. TACs are generated with added Gaussian noise using the noise amplitudes (a) 0.5 (b) 2 and (c) 4 and equation 5.4

con function of MATLAB Optimisation Toolbox was used to minimize this cost function. The optimisation was done using Ordinary Least Squares (OLS). For all cases, tolerances on parameter values (TolX) was set to 10^{-4}, tolerances on the objective function value (TolFun) was set to 10^{-4} and maximum number of function evaluations was set to be 10^4.

$$\phi(p) = \sum_{i=1}^{n} \sum_{j=1}^{m} w \left[E_i(t_j) - M_i(t_j) \right]^2 \tag{5.5}$$

where n is the number of regions, m is the number of time points in each TAC, w is the weighting, E is the measured concentration of the tracer in the region at

time point t_j and M is the model output with parameter vector p, which includes 5 parameters (K_1, k_2, k_3, k_4 and V_b) from each region of interest and 6 parameters ($A_1, A_2, A_3, \lambda_1, \lambda_2, \lambda_3$) from the AIF model. Uniform weighting was applied in this optimisation.

As mentioned previously, one or more arterial or venous blood samples can be used to scale the input function and normalise the estimated AIF. In this work, two different scaling methods were implemented and their performances were evaluated. The first AIF scaling method is in the original SIME work by Feng et. al, where multiple blood samples towards the end of the study were used to aid the recovery of AIF [Feng et al., 1997]. As A_3 and λ_3 dominate the tail of the AIF model, which represents the end of the scanning period, it can be assumed that these parameters can be obtained by fitting two or more blood samples measured near the end of scanning. In this simulation work, parameters A3 and λ_3 were kept fixed to their true values in order to reproduce the effect of this scaling method on the parameter estimates.

An alternative AIF scaling method was also implemented, where only one blood sample is obtained at the end of the scan. Then, the ratio of estimated AIF's endpoint to the actual radioactive tracer concentration obtained by blood sample is used as a factor to scale the whole input function. This was simulated by computing the ratio of true input function endpoint to estimated input function endpoint and multiplying the whole input function with this ratio.

5.4.2 Analysis of parameter estimates

The simulation study was repeated 5 times using the simulated dataset at each of 3 noise levels. The five different experimental scenarios can be listed as following:

1. No prior information, single point AIF normalisation
2. With prior information, single point AIF normalisation
3. No prior information, multiple point AIF normalisation
4. With prior information, multiple point AIF normalisation
5. Input function parameters fixed to their true values

AIF parameters and rate constants, together with the blood background, were estimated for each of 50 noise realisations. In the fifth case, all of the six AIF parameters were fixed to their true values and only the kinetic parameters were estimated. This was done in order to see the accuracy of estimated parameters when the perfect AIF was used.

In order to simplify the analysis of results, influx rate, K_i values of the estimated kinetic parameters were calculated and used in the analysis. A sensitivity analysis on the fixed value of the AIF parameter was performed by deliberately including an error on the fixed λ_1 parameter. This is performed to simulate the situations where λ_1 can not be extracted due to small variations in the AIF peak shapes. We have added $\pm 10\%$ error on the fixed λ_1 parameter values and evaluated its effect on the K_i estimates. All the starting parameters, lower and upper bounds, and optimisation settings were kept identical to the ones used in the previous experiment.

Figure 5.3 illustrates how the AIF changes with different λ_1 values.

$$\mathrm{CV}_{\overline{P}} = \frac{SD_{|P|}}{|\overline{P}|} \times 100\% \tag{5.6}$$

$$\mathrm{Bias} = \left| \frac{P^{\mathrm{true}} - \overline{P}}{P^{\mathrm{true}}} \right| \times 100\% \tag{5.7}$$

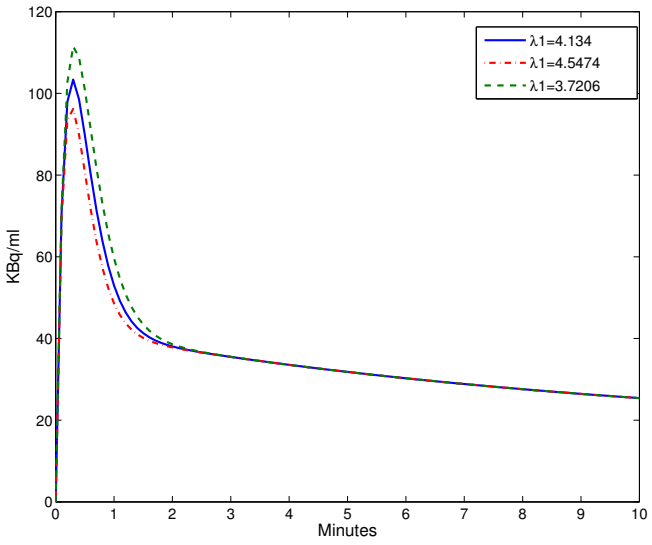

Figure 5.3: Simulated arterial input function with different λ_1 values. λ_1 was set to 4.134 to represent Feng's AIF model. AIFs with $\pm 10\%$ error on λ_1 are also shown to model the effect of error in the AIF.

Finally, in order to further evaluate the performance of the method, the simulation study was repeated with four other sets of rate constants obtained from various published FDG brain tumour studies (group 2 from [Ishikawa et al., 1990] group 3 and 4 from [Kimura et al., 2009], and group 5 from [Spence et al., 2004]). Similar to the first study, rate constants were obtained from grey matter, white matter and

tumour tissue (Range of K_1: 0.023-0.10 mL/cm^3/min, k_2: 0.087-0.162 1/min, k_3: 0.032-0.107 1/min, k_4: 0.001-0.15 1/min, BV: 0.3-0.7 mL$/100g$). TACs were generated using these rate constants and Feng's input function and gaussian noise was added to the generated TACs. Single-blood AIF sampling was performed only.

For each of these runs, absolute bias and coefficient of variation (CV) values were calculated and used in the performance comparison. These were calculated by using equations 5.6 and 5.7 respectively, where $\overline{P}$ represents the mean of parameter over 50 noise realisations, $SD_{\overline{P}}$ represents the standard deviation of $\overline{P}$ and P^{true} is the true value of the parameter.

5.5 Results

Firstly, the effect of fixing one of the AIF parameters to its true value on the bias and coefficient of variation of estimates was explored. The average bias on kinetic parameters of each ROI is shown in figure 5.4 for each of the 5 methods and noise levels used. It can be seen that when no AIF parameter was fixed and AIF scaling with a single blood sample was used, the average bias on the K_i estimates, averaged over three noise levels, was approximately 13.8%. This was reduced to 5.4% when the λ_1 parameter of AIF was fixed to its true value. When the AIF was scaled using the method where the tail was fit to multiple blood samples, the average bias was 13.5% and was reduced to 10.6% after λ_1 was fixed to its true value. The average bias on the estimated K_i was 5.2% when all six parameters of the input function were set to their true values and only values of the kinetic parameters and the vascular fraction for each ROI were estimated. The same trend was seen at all

noise levels. Also the biases of the fits were close to the bias with true input function when one input function parameter was obtained from prior information. However the observed improvement was decreased as the noise level increased.

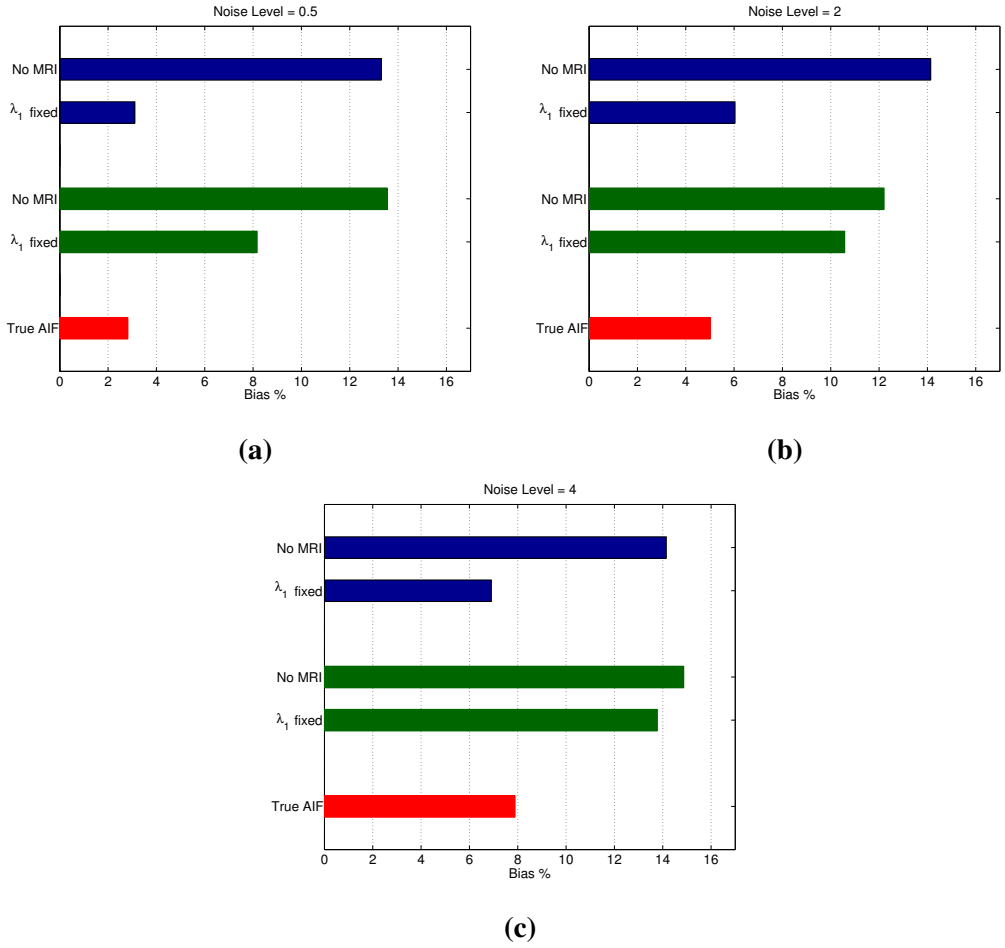

Figure 5.4: Percentage absolute bias on 50 K_i estimates, averaged over three ROIs, when noise level was set to (a) 0.5, (b) 2, (c) 4. Blue bars on top show the bias with the scaling method with one blood sample obtained at the end of the study, green bars show the bias with the scaling method where the tail is fit to the multiple blood samples obtained towards the end of the study and red bars show the bias which would be present when all six parameters of the AIF was set to their true values.

The biases on K_i estimates and average biases of $k_2, k_3, and k_4$ are shown in figure 5.5. It can be seen from these figures that fixing the λ_1 parameter generated the biggest improvement on the K_1 estimates. When the single blood sample AIF

scaling method was used, the bias on K_1 was reduced from 46.3% to 10.3%, averaged over all noise levels. When the alternative AIF scaling method was used, 58.6% bias was seen on K_1 estimates even after the λ_1 parameter was fixed to its true value. The bias of parameters k_2, k_3, k_4 and V_b were comparable across the two AIF scaling methods. Fixing the λ_1 parameter caused much smaller improvements on k_2, k_3, k_4, compared to the K_1 estimates. V_b estimates had 66.8% absolute bias which was reduced to 64.8% when λ_1 parameter was fixed to its true value for the single point AIF normalisation method. However, the high bias on the BV did not affect the accuracy of K_i estimates. This was confirmed by a separate experiment by estimating the K_i with V_b fixed to its true value where only 0.28% increase in overall bias was observed.

Figure 5.6 shows the summary of coefficient of variation of estimated K_i parameters, averaged over three ROIs and plotted for each noise level. These results indicate that both AIF scaling methods yielded K_i estimates with no significantly different CV values. Before the λ_1 parameter was fixed, using the scaling method with single blood sample resulted in K_i estimates with 6.3% CV, which was reduced to 5.7% after fixing the λ_1 parameter. In the case of AIF scaling method with multiple blood samples, this method produced K_i estimates with 6.7% CV and this was improved to 5.4%. Finally, the run with the true input function estimated the influx rate parameter with average CV of 4.0%.

These results shows that fixing the λ_1 parameter of AIF did not result in a significant improvement in CV values of K_i estimates. Both AIF scaling methods produced similar CV values and none was able to match the accuracy of parameter

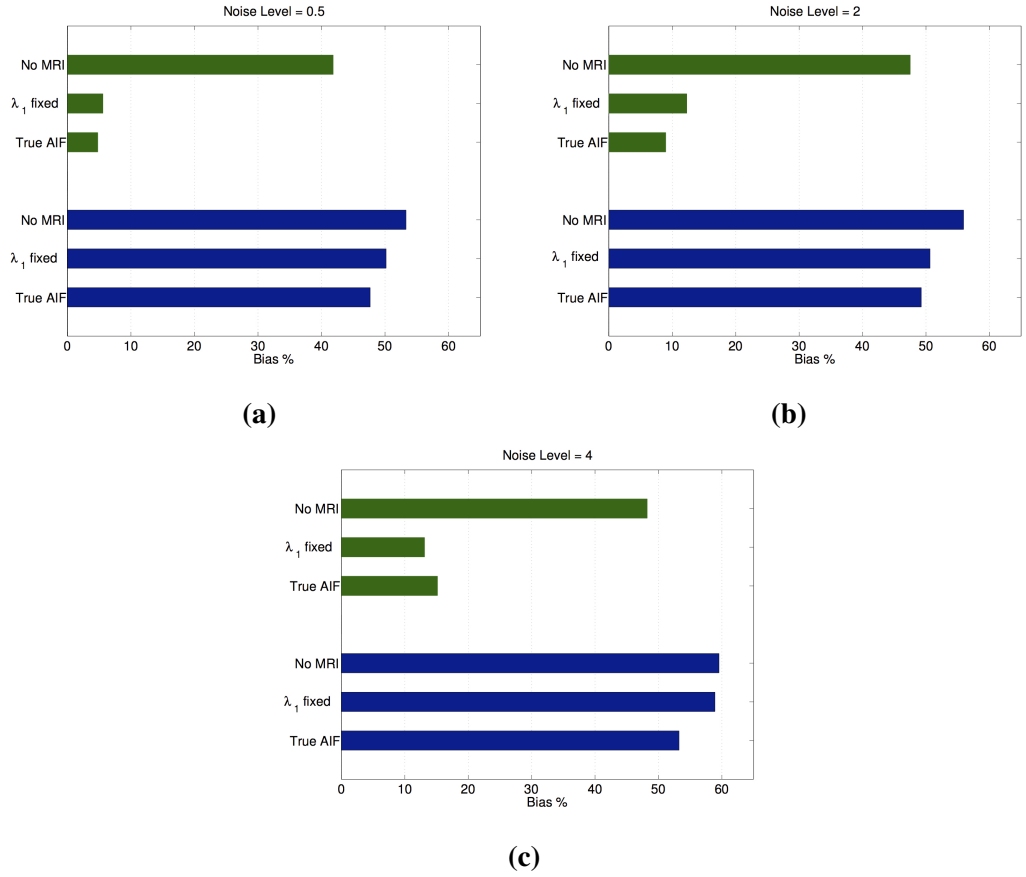

Figure 5.5: Absolute bias on 50 K_1 and an average of the $k_2, k_3, and k_4$ parameter estimates, averaged over three ROIs. Results are shown for noise levels (a) 0.5, (b) 2, (c) 4. Only one blood sample AIF normalisation results are shown. Green bars indicate the bias on K_1 estimates and blue bars indicate the average bias on $k_2 - k_4$ estimates.

estimates with the true AIF. For the single blood sample AIF scaling method, improvement was only seen in the lowest noise level but almost identical CV values were seen with the datasets with higher noise. When the AIF was scaled using multiple blood samples, the CV of estimates was halved when the noise was set to 0.5. The improvement decreased as the noise level was increased.

Figure 5.7 shows the bias on K_i values when the λ_1 is underestimated or overestimated by 10%. Results obtained with the single blood sample AIF scaling method are shown only. Bias on parameter estimates obtained with no λ_1 fixing and when

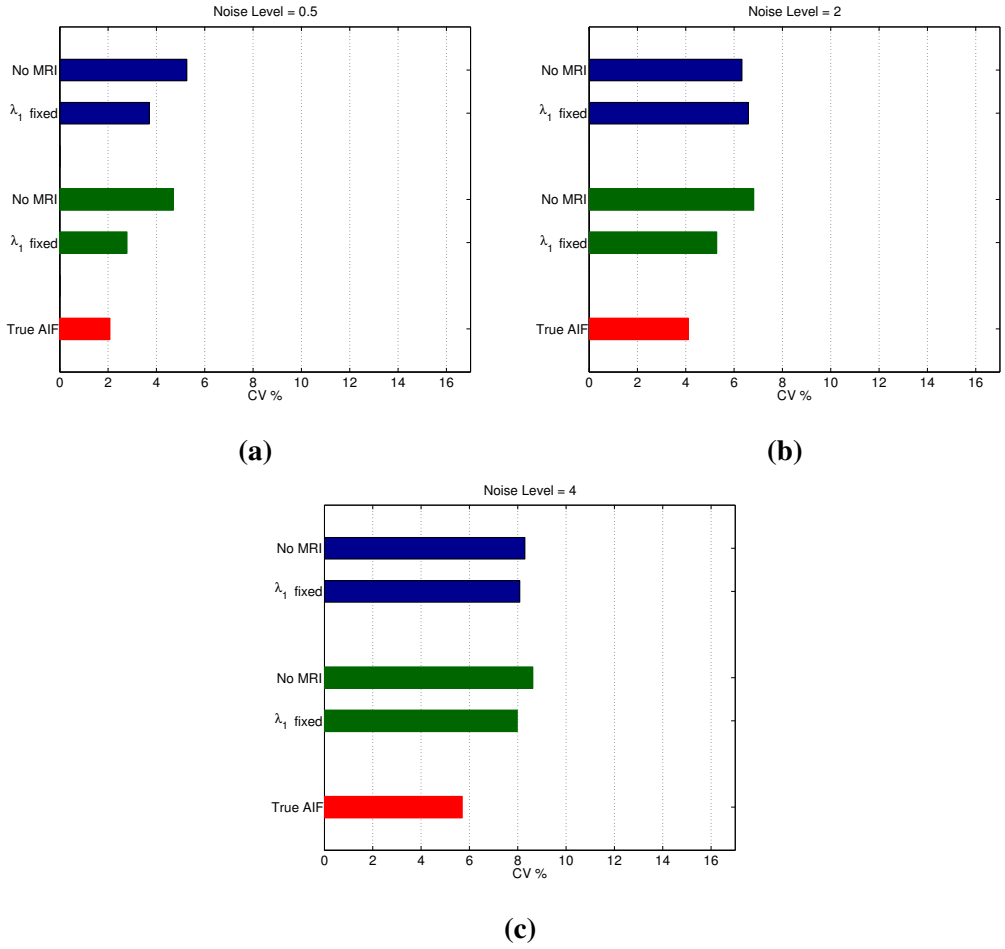

Figure 5.6: Coefficient of variation values over 50 K_i estimates, averaged over three ROIs, when noise level was set to (a) 0.5, (b) 2, (c) 4. Blue bars on top show the CV with the scaling method with one blood sample obtained at the end of the study, green bars show the CV with the scaling method where the tail is fit to the multiple blood samples obtained towards the end of the study and red bars show the CV which would be present when all six parameters of the AIF was set to their true values.

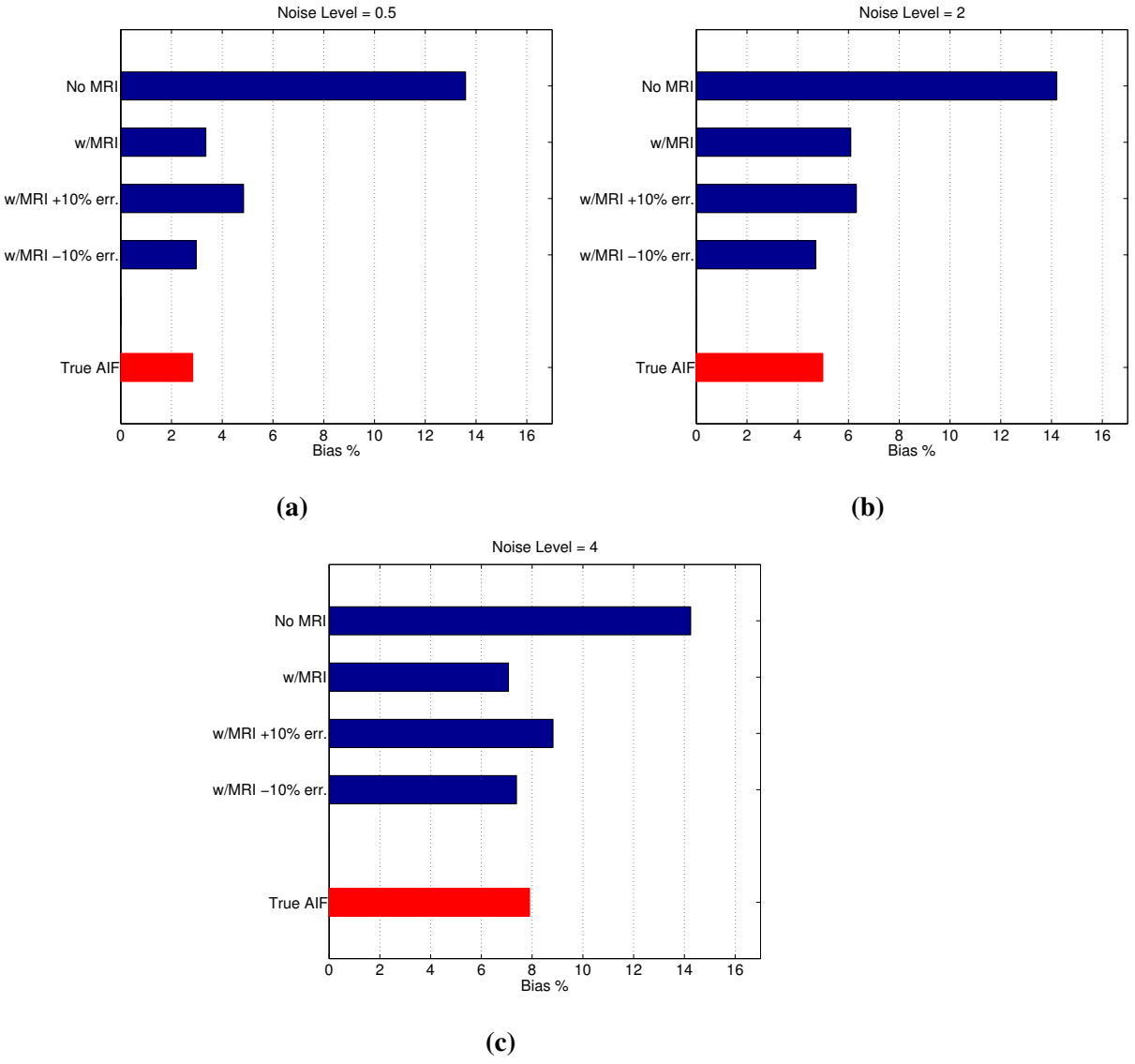

Figure 5.7: Absolute percentage bias on estimated Ki values for low noise data. Blue bars show results without the MRI component, one PET-AIF parameter fixed assuming it can be obtained from MRI-AIF, $\pm 10\%$ error added on the fixed AIF parameter. Red bar shows the bias on estimates when all the AIF parameters were fixed to their true values.

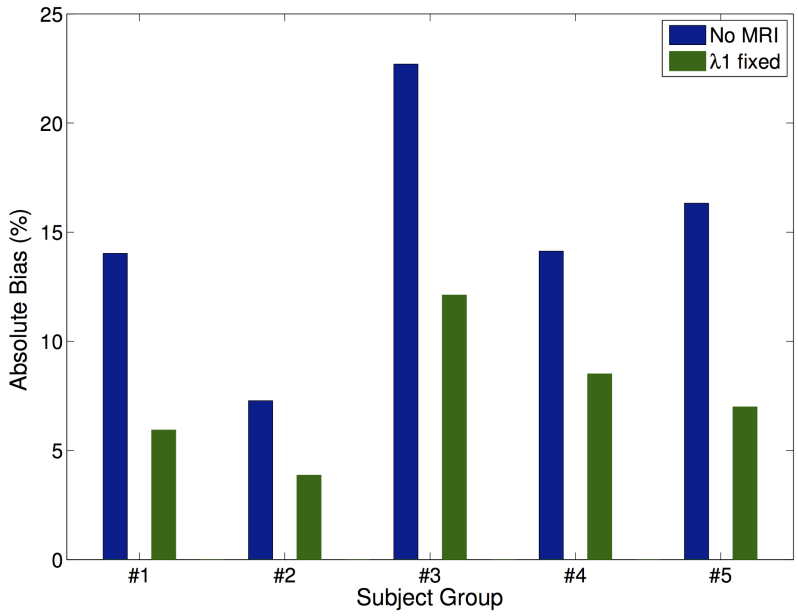

Figure 5.8: Results of the inter-individual variability analysis. Reduction in absolute bias of K_i estimates after fixing λ_1 to its true value are shown for five different simulation studies. Results for noise level 2 and single point AIF normalisation method are shown only. Black bars show the results with no MRI information and grey bars denotes the results with λ_1 fixed.

λ_1 was fixed to its true value are also included in the plot for comparison purposes. These results show that much lower bias values were obtained, compared to the original SIME method with no prior information, even when $\pm 10\%$ error was present in the fixed AIF parameter. The method estimated rate constants more accurately when the λ_1 was underestimated rather than overestimated.

Results of the inter-individual simulation study are shown in figure 5.8. Absolute bias on K_i estimates obtained in 5 different simulation studies with TACs generated with different sets of rate constants are included. Significant reduction in absolute bias of estimates was obtained by fixing λ_1 to its true value in all of the 5 different simulation studies. It can be seen that including the prior AIF information reduced the bias in the range of 3.4% to 12%.

5.6 Discussion and Conclusions

In this chapter, we proposed a novel approach for improving AIF estimation and hence kinetic parameter estimation in dynamic FDG-PET studies with the SIME method by utilising prior information for the early part of the input function. We used simulated data to compare estimated parameters with and without the prior AIF information. With the single-point AIF normalisation method, the bias in the K_i values was reduced by 77%, 57% and 51% respectively for each noise level using the proposed method, to a level similar to that obtained with fully know AIFs. For single blood sample AIF normalisation method, utilising the prior information gave slightly better results than true AIF results at the highest noise level. A similar behaviour was also seen for the K_1 estimates. A paired t-test comparison of the absolute error in individual k_2 estimates obtained with both methods showed that the difference in both sets of estimates is not statistically significant, with p values of 0.09, 0.37 and 0.23 for the three ROIs.

The improvement in K_i biases was insensitive to small errors in the fixed values of λ_1 ($\pm 10\%$). The bias-reduction was much lower when the more complex normalisation procedure was used, which involves collecting multiple blood samples in practice. The biggest improvement was seen in the K_1 estimates. The variance in K_i was reduced only in the low-noise case. The reduction was slightly larger with the more complex normalisation.

One way of obtaining prior information regarding the early part of the AIF can be utilising an MRI derived AIF. The AIF measured from a DCE-MRI or DSC-MRI with a Gd based contrast agent will give accurate results regarding the peak of

the input function due to its high temporal resolution. In a simultaneous PET/MRI study, the blood flow and cardiac output, which dominate the early part of an AIF, are expected to be similar between the PET and MRI studies. Hence, if it is assumed that there is negligible PET tracer uptake by the lungs, it can be expected to see high degree of similarities between the peak shapes of the PET-AIF and MRI-AIF. This assumption was shown to be valid in preclinical studies [Poulin et al., 2013] [Evans, 2015]. We also evaluate this hypothesis in Chapter 6 with clinical PET and MRI AIFs.

In addition to FDG studies, the SIME method is a promising approach to analyse other tracers (i.e. [Wong et al., 2001] [Ogden et al., 2010]). As the parametric AIF measured using this method will be free of metabolite products, it can potentially be used to study tracers with metabolites present in the blood. This is further explained and tested in Chapter 7.

In conclusion, we have shown that the accuracy of kinetic parameter estimation by the SIME method can be improved by introducing prior information about the AIF. Prior AIF information was used to fix some of the parameters of the parametric AIF to their true values which reduced the bias on the estimated kinetic parameters. The method requires a single blood-sample at the end of the scan for AIF normalisation and can be used to avoid the need for collecting multiple blood samples.

Chapter 6

Comparison of PET and MRI derived input functions

6.1 Introduction

An accurate measurement of the AIF is also necessary in the kinetic analysis of dynamic Magnetic Resonance Imaging (MRI) with paramagnetic contrast agents like Gadolinium (Gd) chelates. In MRI, the arterial input function can be measured by withdrawing arterial samples but it is usually avoided in practice due to its invasiveness. Population based AIFs [Parker et al., 2006] [Orton et al., 2008] [Shukla-Dave et al., 2009] are commonly used in dynamic MRI analyses but are limited in their accuracies due to inter-subject variations. DCE-MRI and DSC-MRI techniques can also be used to provide personal estimation of the AIF by measuring the effect of Gd-based contrast agent on T_1, T_2 and T_2* signals. Using DSC-MRI to measure the AIF can have some advantages over PET. This biggest benefit of using MRI it its higher temporal resolution which can be used to detect the rapid changes during the

first passage of the contrast agent.

For most PET tracers with no or minimal uptake in the lungs, the early peak of the input function mainly describes the delivery of the PET tracer or MRI contrast agent to the tissue of interest and is dominated by the cardiac output and blood flow [Calamante et al., 1999]. Therefore, if the PET data and MRI data are obtained at the same time, similarities are expected to be seen in the early parts of the PET-AIF and MRI-AIF. However, the peak shape of an input function also depends on the injection duration which are usually different in PET and MRI. PET tracers are usually injected with a slow injection rate due to low temporal sampling of PET scanners. On the other hand, a fast injection rate is favoured in the administration of MRI contrast agents to get the highest signal intensity possible [Aerts et al., 2008]. The difference in bolus shapes caused by different injection duration make an AIF comparison and/or an AIF conversion more difficult. In this chapter, we propose an input function model which addresses this problem and accounts for injection duration in the AIF fitting. PET-AIFs and MRI-AIFs were fitted using this input function and bolus shapes were visually compared after necessary corrections. It is also checked if fitting the PET-AIF and MRI-AIFs with the same input function produced similar model parameters and if a parameter conversion can be reliably performed.

6.2 Literature Review

There have been multiple attempts to compare PET derived and MRI derived AIFs and to investigate if an AIF conversion can be done from one modality to the other.

The majority of these studies were performed in preclinical studies where it was attempted to introduce a mixture of Gd-DTPA contrast agent and the PET tracer in a single injection. A brief summary of these studies including some human studies is presented in this section.

In 2005, Ibaraki et. al [Ibaraki et al., 2005] presented their work where AIFs derived from DSC-MRI studies were compared to AIFs from ^{15}O-water PET studies. In order to make a comparison possible, bolus injection duration of the PET tracer and MR contrast agent were kept the same (around 3 seconds). PET and MR data were acquired using separate scanners. PET-AIFs were determined using arterial blood samples and were corrected for delay and dispersion effects. For seven healthy volunteers, they observed similar shapes between PET-AIF and MRI-AIF pairs. Average time to peak values were identical for PET-AIF and MRI-AIF, 15.1 $\pm$ 2.0 sec and 14.9 $\pm$ 2.2 sec respectively. Similarly, both PET-AIF and MRI-AIF had similar average peak widths, 6.5 $\pm$ 0.4 sec and 6.7 $\pm$ 1.1 respectively. As the ^{15}O-water is a freely diffusible tracer, similar tail shapes were also observed between the AIF tails.

In 2013, Poulin et. al [Poulin et al., 2013] proposed a method to convert an arterial input function derived from Gd-DTPA in MRI, into a ^{18}F-FDG AIF in PET. In their study they performed PET and MRI experiments on seven healthy rats using separate scanners. During the dynamic PET study, a solution of ^{18}F-FDG and Gd-DTPA was injected using an automatic injection pump. Blood samples were collected at seventeen different time points to determine plasma concentrations of ^{18}F-FDG and Gd-DTPA in each of the samples. A second MRI-AIF was also mea-

sured from the DCE-MRI images, where a separate contrast agent injection was performed with a similar protocol. Peaks of PET-AIF and MRI-AIF curves were normalised to one and then fitted with convolution of a rectangular function, representing the injection, with a bi-exponential representing the elimination. For 7 rats, PET-AIFs and MRI-AIFs were fitted using this model and population based ratios (Gd-DTPA/FDF) for each parameter was computed. These population based ratios were used to convert PET-AIF to MRI-AIF or vice versa in normalised concentration. A single blood sample at the maximum concentration of ^{18}F-FDG/Gd-DTPA is used to scale the curves in mM or kBq/μL. However, it was also shown that a normalisation factor calculated from the relationship of injected dose to the maximum concentration of ^{18}F-FDG or Gd-DTPA can be alternatively used instead of the blood sample. For all of the rats, similar peak shapes were observed between the PET-AIF and MRI-AIF pairs but tails showed major differences due to different uptake and clearance rates. After the normalisation, fitting, conversion and scaling steps, the MRI-AIFs, both derived from the blood samples and DCE-MRI, could be used in PET and MRI kinetic analysis. These AIFs produced consistent estimates of the cMRGlc, tumour metabolic rate of glucose, as well as K^{trans}, v_e and V_b parameters.

In similar work by Evans et al. [Evans, 2015], a combined bolus injection of Gadovist MR contrast agent and ^{18}F-FDG was performed to 12 wild type Wistar rats in a MRI scanner. The PET-AIF and MRI-AIF were measured by withdrawing serial arterial blood samples. Similar to the work done by Poulin et. al [Poulin et al., 2013], MRI-AIFs were measured from DSC-MRI images as well as the ar-

terial samples. However, in this study, the blood sampling was performed in the MR scanner so no separate contrast agent injection was performed. An automatic AIF determination algorithm was applied to derive the AIF from DSC-MRI images [Evans et al., 2012]. Following the DSC-MRI data acquisition, DCE-MRI images were also obtained which were used to normalise the tail of the DSC-MRI AIF to absolute contrast agent concentrations. The method proposed by Poulin et al [Poulin et al., 2013] was used to perform AIF conversion on this data. Blood sample scaling was performed on three different points, at the peak, midpoint and the endpoint of the AIF. The peak-injected dose scaling method was also tried after the conversion. High similarity in the AIF peak shapes were observed between the PET-AIFs and MRI-AIFs. After the first pass, differences were seen in the AIF tails. It was also seen that the some of the MRI-AIFs derived from the DSC-MRI images had different lower peaks than the blood samples, which could be a cause of the used temporal resolution. It was concluded that even though the blood sampled contrast agent AIFs can be reliably converted to FDG PET-AIFs, the DSC-MRI image derived AIFs had a worse performance in the conversion. Similar to the results presented by Poulin et al, a linear relationship between the AIF peak and the injected activity was observed.

In 2015, Poulin et al. presented their method where they performed dual kinetic modelling of ^{18}F-FDG PET and DCE-MRI data [Poulin et al., 2015]. Arterial blood samples were withdrawn to measure the PET-AIF and MRI-AIF. Tumour and reference region TACs were extracted by placing ROIs on the tumour and tongue, which was chosen as a suitable reference region due to its large size and conve-

nient location. A reference region AIF (RRAIF) was measured from the tongue, where a linear relationship between its peak concentration and arterial samples AIF peak concentration was observed. This relationship was used to scale the underestimated bolus of the RRAIF to arterial sample concentrations. The AIF conversion method described above [Poulin et al., 2013] was used to convert the RRAIF to PET-AIF. Results from 10 Fisher rats showed that tumour metabolic rate of glucose consumption (tMRGlc) could be estimated using the AIF converted from the corrected RRAIF with no significant difference to PET-AIF ($p<0.05$). This work showed that a PET-AIF can be converted from a reference region measurement in DCE-MRI when certain correction factors are applied.

6.3 Accounting for different injection rates

Similar peak shapes between the input function derived from PET and MRI studies are expected if the differences which can be caused because of the different injection durations are avoided. As described in the literature review of this chapter, some of the previous research studies avoided this by injecting the MR contrast agent and the PET tracer in a single combined injection, completely eliminating any discrepancies which can be caused by the injection duration. However, this technique is not yet validated in human studies. Instead, Ibaraki et al. [Ibaraki et al., 2005] used the same injection protocol (i.e. injection rate) in separate injections of the Gd-DTPA contrast agent and the PET tracer. However, this is not usually the case in clinical practice as a fast injection of the contrast agent is usually favoured to increase the signal in the MR images [Aerts et al., 2008] and the PET tracer is usually injected

with a slower injection duration due to low temporal sampling capabilities of the PET scanners.

In their method, Poulin et. al fitted the AIF curves using a convolution of a rectangular function, representing the tracer/contrast agent injection with a bi-exponential representing the elimination [Poulin et al., 2013]. The limitation of this model is the convolution of a rectangular function with an exponential, resulting in a triangular peak which tends not to fit the bolus well. Instead of this, we have used a 10 parameter ((τ_1, τ_2, P_1, P_2, β_1, β_2, β_3, κ_1, κ_2 and κ_3)) AIF model which is shown in equation 6.1 and illustrated in figure 6.1. This model consists of a double Butterworth function convolved with a tri-exponential function, where the double Butterworth function represents the injection of the tracer or contrast agent and the tri-exponential represents its wash out and clearance phase. The AIF bolus shape can be modelled to represent a slower or faster injection by increasing or decreasing the width of the double Butterworth function, ($\tau_2 - \tau_1$ or $\delta\tau$) respectively. A normalisation factor (ψ) is used to keep the injected volume constant when the injection duration is changed.

$$C_p = \frac{1}{\psi}\left(1 - \frac{1}{1+(\frac{t}{\tau_1})^{P_1}}\right)\left(\frac{1}{1+(\frac{t}{\tau_2})^{P_2}}\right) \otimes \left(\beta_1 e^{-\kappa_1 t} + \beta_2 e^{-\kappa_2 t} + \beta_3 e^{-\kappa_3 t}\right) \quad (6.1)$$

where,

$$\psi = \int_0^{\infty}\left(1 - \frac{1}{1+(\frac{t}{\tau_1})^{P_1}}\right)\left(\frac{1}{1+(\frac{t}{\tau_2})^{P_2}}\right) dt$$

AIF fitting was performed using MATLAB's *lsqcurvefit* function, using the trust-region algorithm. The average of each time frame was used in the optimisation. Curve fitting was performed in two stages: Firstly, the tail of the AIF, for instance the last 10 time points, was fitted using equation 6.1 and the estimated parameters were used as starting points in the second stage, where the whole AIF curve was fitted.

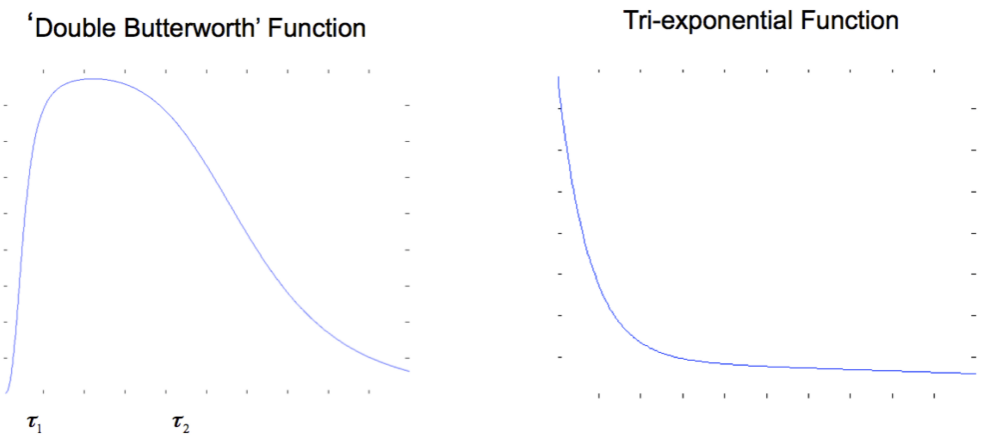

Figure 6.1: Illustration of the two components of the double Butterworth function with 10 parameters. This function is a combination of a Butterworth function with two different legs, representing the injection of the tracer/contrast agent, with a tri-exponential function representing the washout.

Due to the high number of estimated parameters in this AIF model, it is likely that the optimisation can get stuck in a local minimum during the curve fitting. In order to avoid that, MATLAB's *multistart* function was used with 500 iterations. This function runs the optimisation in iterations with various combinations of starting parameters and outputs the parameters which fits the data points with lowest sum of squares error.

6.4 Materials and Methods

6.4.1 Validity of the proposed AIF model

The validity of the proposed AIF model was assessed by fitting whole blood curves derived from ^{18}F-Cho and ^{18}F-FMISO studies. Details about ^{18}F-Cho data acquisitions was reported in section 6.4.3 of this chapter. ^{18}F-FMISO acquisitions were performed on a GE Discovery VCT PET/CT scanner with an injection of 330 MBq of ^{18}F-FMISO. The time frame for the dynamic acquisition was 12x10 sec, 6x20 sec, 6x60 sec, 4x120 sec. Institutional Review Board permission, MHRA approval and informed patient consent were obtained for all studies. The blood TACs used in this validation were derived from dynamic PET frames utilising MR information where the PV effects were corrected using iterative Yang method [Erlandsson et al., 2012a].

The proposed AIF model shown in equation 6.1 was used to fit 8 whole blood TACs derived from ^{18}F-Cho studies and 10 whole blood TACs derived from ^{18}F-FMISO studies. The same whole blood TACs were also fitted using the commonly used Feng's input function model [Feng et al., 1993], which is the sum of a gamma variate function with two exponentials. The goodness of fit of each model was compared using an F-test, accounting for different number of estimated parameters used in each of the AIF models. The F-test quantifies the relationship between the relative change in the sum of squares error (SSE) and the relative change in the degrees of freedom DF and is calculated using equation 6.2.

$$\mathrm{F-TEST} = \frac{(\mathrm{SSE}_1 - \mathrm{SSE}_2)/(\mathrm{DF}_1 - \mathrm{DF}_2)}{\mathrm{SSE}_2 - \mathrm{DF}_2} \tag{6.2}$$

In order to better understand the behaviour of the proposed AIF model, the relationship between the width of the fitted double butter worth function and the injection duration used tracer/contrast agent administration is studied. Published data from a study performed by Holt et. al [Holt et al., 2011] were used where the impact of the injection duration on the AIF shapes and estimated K^{trans} values were evaluated. In this study, DCE-MRI scans with Gd-DOTA contrast agent were performed on 24 patients with prostate cancer. The subjects were separated into 6 groups which represent the 6 different injection durations used in this study: 5 sec, 7.5 sec, 10 sec, 15 sec, 20 sec, and 30 sec. For each subject, AIFs were extracted from a straight part of the femoral arteries (10 slices) using MR phase images. AIFs of each of these six groups were averaged and group-averaged phase AIFs were used in the further analysis.

6.4.2 Simulated Input Functions

^{18}FDG AIFs were simulated using Feng's parametric input function with their published averaged values (equation 6.3) [Feng et al., 1993]: A_1=851.1225, A_2=21.8798, A_3=20.8113 in $\mu C_i/mL$ λ_1=4.1339, λ_2=0.1191 and λ_3=0.0104 in 1/min. MRI-AIFs were simulated using Parker's input function model (equation 6.4 [Parker et al., 2006] with the following published values: H_1=0.809, H_2=0.330 in mmol/min, y_1=0.17046, y_2=0.365, z_1=0.0563, z_2=0.132 in min, u=1.050 mmol, rho=0.1685 1/min, s=38.078 1/min and v =0.483 min.

$$\mathrm{AIF}_{\mathrm{Feng}}(t) = (A_1 t - A_2 - A_3)e^{-\lambda_1 t} + A_2 e^{-\lambda_2 t} + A_3 e^{-\lambda_3 t} \tag{6.3}$$

$$\mathrm{AIF}_{\mathrm{Parker}}(t) = \sum_{n=1}^{2} \frac{H_n}{z_n\sqrt{2\pi}} e^{-(t-y_n)^2/2z_n^2} + \frac{ue^{-\rho t}}{1+e^{-s(t-v)}} \tag{6.4}$$

No time delay was applied to the simulated PET-AIF and MRI-AIFs. MRI-AIFs were simulated by sampling for every 4 second. The PET-AIF was simulated using the following framing: 13 x 10 sec, 4 x 30 sec, 6 x 60 sec, 4 x 120 sec, 8 x 300 sec. The simulated PET-AIF and MRI-AIF can be seen in figure 6.3.

6.4.3 Clinical Data

Dynamic ^{18}F-Fluoroethylcholine (^{18}F-Cho) and DSC-MRI scans were performed on four children with histologically proven astrocytic tumours. The ^{18}F-Cho and the MRI scans were performed as part of their diagnostic assessments. The subjects were placed into the scanner and were injected with an average of 250 MBq (^{18}F-Cho). Dynamic PET acquisition was performed for 45 minutes. The PET tracer was injected manually by a radiographer present in the scanning room with an unknown injection duration. Two of the dynamic PET scans were acquired on a GE Discovery VCT (GE Medical Systems, Milwaukee, Wis, USA) PET/CT system and the other two were acquired on a Siemens Biograph mMR scanner (Siemens Healthcare, Erlangen, Germany). For the PET scans performed in the PET/CT scanner, the map from the CT data was used for the attenuation correction whereas for the

PET/MR scans, the UTE derived attenuation maps were used. The images were reconstructed to a 128x128x51 image space with a voxel size of 1.953 x 1.953 x 3.27 mm. Iterative OSEM 3D reconstruction was used to reconstruct the dynamic PET data to 23 frames with the following durations: 1 x 35 seconds, 8 x 12 seconds, 2 x 27 seconds, 2 x 60 seconds, 3 x 90 seconds, and 7 x 300 seconds.

^{18}F-Cho is a PET tracer which is metabolised to form of radiometabolite side products by the cell membranes. These metabolites can return back to the blood plasma and contribute to the blood signal measured by the PET scanners. This limits the non-invasive measurement of AIF using image-based methods and requires collection of arterial blood samples to measure the parent tracer concentration. However, due to the lack of facilities available, no arterial blood samples were obtained as part of this study.

All of the MRI data were acquired on the Siemens Biograph mMR system. Anatomical T_1 weighted MPRAGE images were acquired in saggital direction and were reconstructed into a 192 x 227 x 512 image space with a voxel size of 1 x 1 x 0.508 mm. The MRI protocol also included a DSC-MRI scan with a Gd-DOTA contrast agent (0.2 mL/kg). The contrast agent was administered using an automatic injector with an injection rate set to 4 ml/sec. Images were acquired for 3.50 minutes and reconstructed with a voxel size of 1.1 x 1.1 x 1.1 mm.

MRI-AIFs were extracted using Perfusion Mismatch Analyzer [Kudo et al., 2007], and its automatic arterial pixel selection algorithm. For each subject, nine best pixels were selected and their mean intensities over time were calculated. MR images were used to improve quantification of the blood concentration measure-

ment from PET images using a similar method to the methodology presented in chapter 4. Post-contrast T1-weighted MPRAGE MR images were used to perform 3D segmentation of carotid arteries. PET frames were coregistered and resampled to MPRAGE space using rigid body registration. PVC was performed on these co-registered PET frames using the iterative Yang method [Erlandsson et al., 2012a], where the reference MPRAGE image was used to create the brain mask for different anatomical regions. Finally, the mean intensity over the defined arterial voxels was computed to determine the whole blood concentration for each PET time frame. The PET-AIF and MRI-AIF curves were fitted independently using our proposed 10 parameter AIF model.

6.5 Results

6.5.1 Validity of the proposed AIF model

The proposed AIF model was able to fit all of the ^{18}F-Cho and ^{18}F-FMISO whole blood TACs with no visible artefacts. Results of F-test showed that the proposed AIF model fit all of the ^{18}F-Choline whole blood TACs and nine out of ten FMISO whole blood TACs significantly better than Feng's model ($p < 0.05$). These result show that our proposed 10 parameter AIF model was able to fit the ^{18}F-FMISO and ^{18}F-Cho blood TACs with a good degree of accuracy and can be regarded as a valid model to be used in AIF fittings.

The proposed 10 parameter AIF function was also able to fit the averaged MRI-AIFs of each group used to assess the relationship between the injection duration and the AIF shapes. The AIF curves and the fitted functions are illustrated in figure

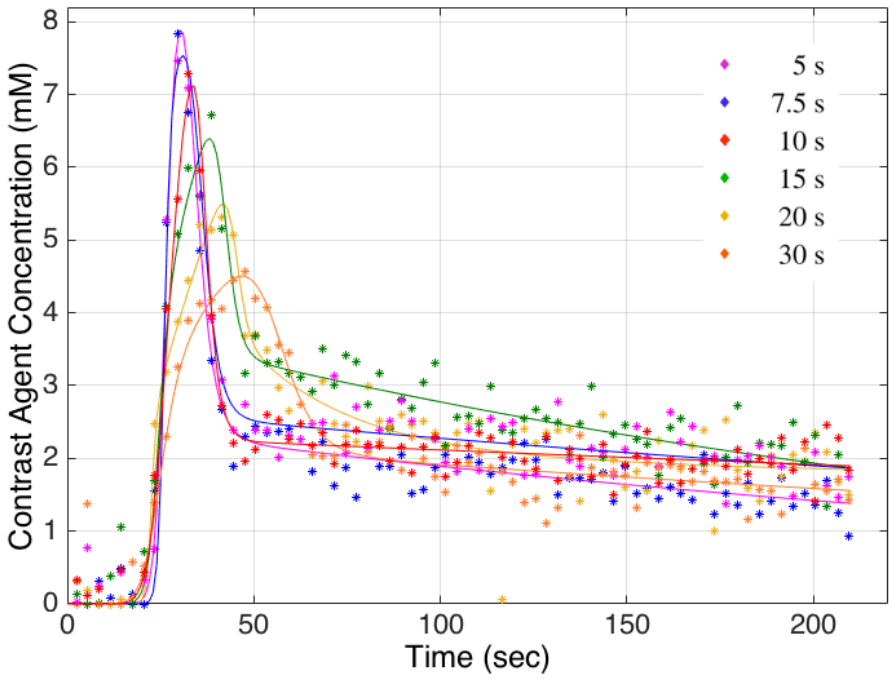

Figure 6.2: Illustration of arterial input functions with 6 different injection durations

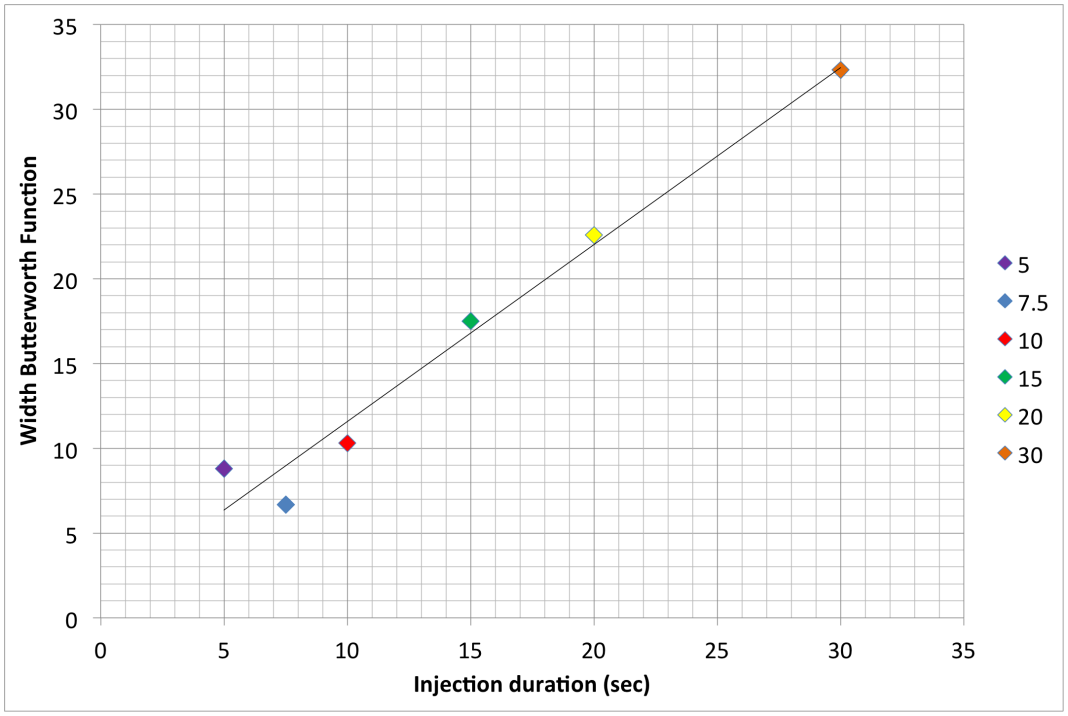

Figure 6.3: Relationship between the injection duration and fitted $\Delta\tau$ values.

6.2. It can be seen that all of the AIF curves were fitted with a good accuracy, regardless of the injection duration and the peak shape. The width of the AIF peak increased as the injection duration was prolonged. As a result of this, the maximum peak height decreased with the tracer arriving to the arteries with a smaller velocity.

Table 6.1: Comparison κ_1, τ_1, τ_2 parameter values for AIFs with different injection duration when fitted with the 10 parameter AIF Model

AIF	κ_1	τ_1	τ_2	$\Delta\tau$
5 sec	27.2	26.4	35.2	8.8
7.5 seconds	26.4	26.0	32.7	6.7
10 seconds	26.7	25.9	36.2	10.3
15 seconds	27.4	24.4	41.9	17.5
20 seconds	29.3	22.5	45.1	22.6
30 seconds	28.7	24.9	57.2	32.3

The injection duration and the width of the fitted AIF peak ($\Delta\tau$) is plotted in figure 6.3 for each of the 6 input functions. This plot shows that the width of the AIF peak or the double Butterworth function increases as the injection is further prolonged. A linear relationship between the injection duration and the width of the double Butterworth function is observed when a straight line is fitted through the data points (R^2=0.97). The estimated values of τ_1, τ_2, and κ_1 parameters of the AIF model are included in table 6.1. It can be seen from this table that the fitted κ_1 values, which is the exponential rate of the washout phase, do not vary much between the fitted AIF groups and range between 26.4 and 29.3. This indicates that the differences seen in the AIF peak shapes are mostly caused by the differences in the fitted τ_2 parameters, hence the difference in the injection duration.

6.5.2 Simulated and Clinical AIF Fits

The proposed model was used to fit simulated PET and MRI AIFs, as well as clinical ^{18}F-Cho and DSC-MRI derived whole blood TACs. The simulated AIFs and their fits are shown in figure 6.4. It can be seen that the peak of the PET-AIF is wider than the peak MRI-AIF, which shows the effects of the slower injection durations used in PET tracer injection.

After the curves were fitted, τ_2 parameter of the double Butterworth function was modified to change the injection duration and the modified AIFs were visually compared. For both PET and MRI AIFs, increasing the τ_2, hence the $\Delta\tau$, caused shorter and wider AIF peaks, which is what we would expect to observe with a slower tracer injection. On the other hand, with smaller $\Delta\tau$ values, taller but narrower peaks were seen. Results for MRI-AIFs with modified τ_2 parameter values are shown in figure 6.5.

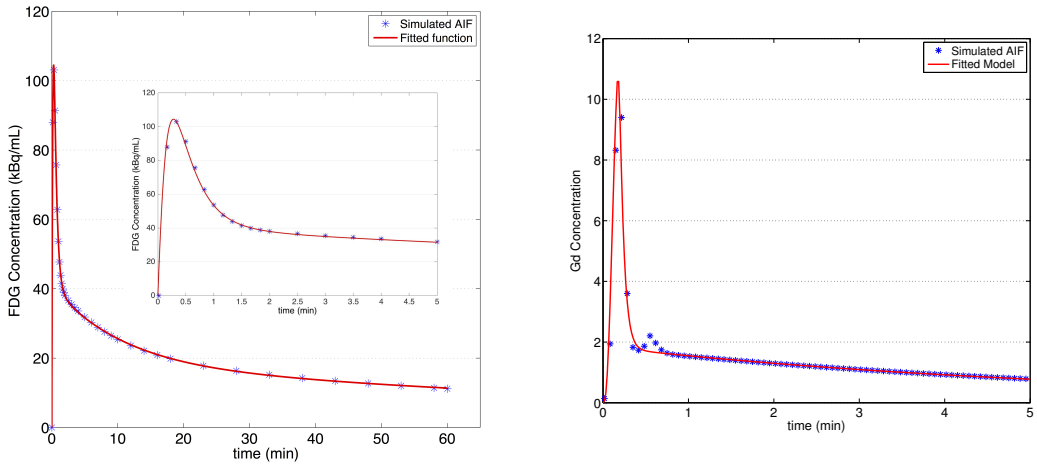

(a) **(b)**

Figure 6.4: 'Double Butterworth' function fitted to (a) population based PET-AIF [Feng et al., 1993] plotted together with a subplot illustrating the peak only (first two minutes) and (b) population based MRI-AIF [Parker et al., 2006].

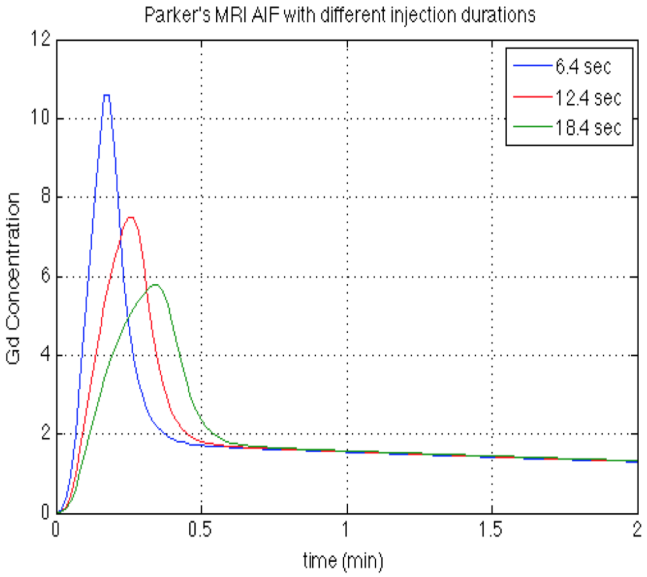

Figure 6.5: Simulated MRI-AIFs using Parkers population-based input function refitted with the developed function. AIF shapes with different injection durations, $\Delta\tau$ are illustrated.

The four ^{18}F-Cho image derived whole blood TACs and DSC-MRI derived AIFs were also fitted with our 10 parameter AIF model. In order to account for different injection durations used during the PET tracer and MR contrast agent injections, the τ_2 parameter of the MRI-AIF was increased to simulate a longer injection duration. The remaining 9 parameters of the fitted AIF were not changed in this process. This was performed within an optimisation procedure until the best match between the modified MRI-AIF and PET-AIF was obtained.

PET-AIFs and adjusted MRI-AIFs of the four patients are shown in the figure 6.6. The peak of the MRI-AIF is scaled to match the peak of the PET-AIF. For all of the four subjects, similar bolus shapes between PET-AIF and MRI-AIF were seen after modifying the MRI-AIFs injection duration. These similarities were observed for approximately the first 20 seconds from the time of administration of the

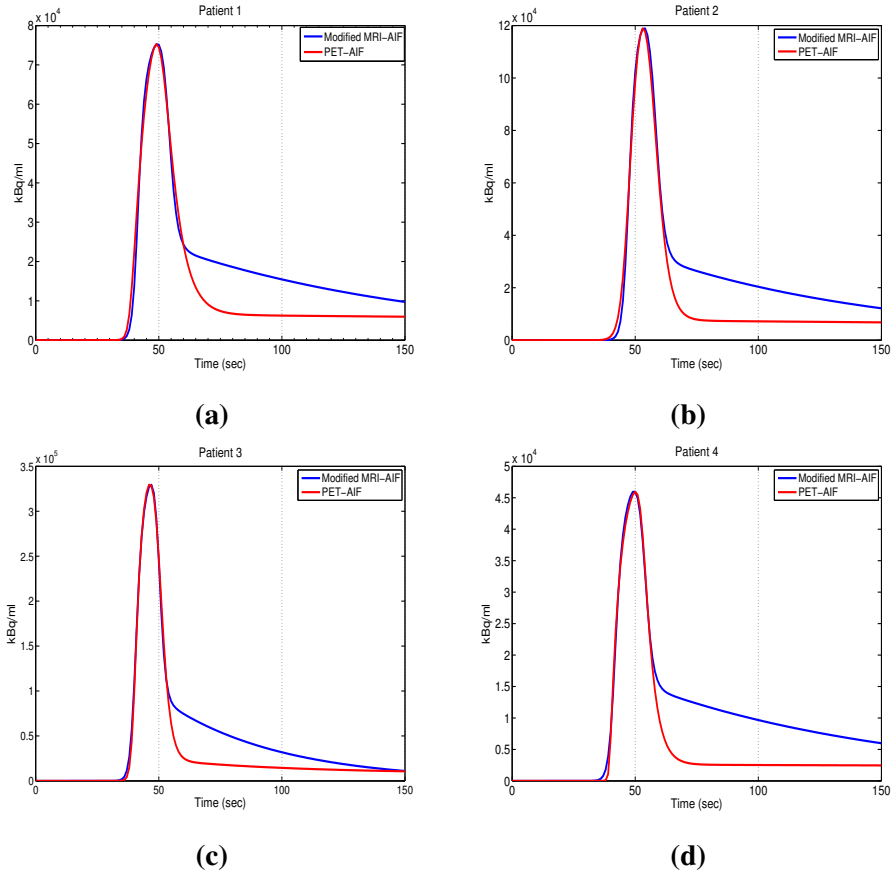

Figure 6.6: Fitted PET-AIFs and MRI-AIFs, adjusted for injection duration, of 4 patients. The MRI-AIFs were scaled to match the peak of the PET-AIF.

tracer/contrast agent. After that, the curves started to deviate as the ^{18}F-Cho and Gd-DOTA have different clearance characteristics.

Table 6.2: Comparison of fitted κ_1 values when fitted with the 10 parameter AIF Model

	PET	MRI	Percentage Error (%)
Patient 1	48.2	45.0	6.6%
Patient 2	62.5	66.1	-5.8%
Patient 3	47.8	45.1	5.6%
Patient 4	46.4	44.7	3.7%

In order to further validate this similarity in early AIF curve shapes, fitted parameters of the PET-AIF and MRI-AIF were compared. We focus on the values

of the κ_1 parameter of the 10 parameter AIF model, the decay constant of the first exponential, as it describes the early wash-out decay of the input function. κ_1 values for fitted PET and MRI curves are listed in table 6.2. These results show that similar estimates were obtained in all of the AIF pairs. It can be stated from these 4 subjects that the value of κ_1 parameter of the PET-AIF can be determined from an MRI-AIF with a maximum error of 6.6%.

Table 6.3: Comparison of fitted λ_1 values when fitted with 6 parameter Feng AIF Model

	PET	MRI	Percentage Error (%)
Patient 1	0.188	0.190	1.06%
Patient 2	0.209	0.204	-2.39%
Patient 3	0.227	0.235	3.52%
Patient 4	0.196	0.196	-0.26%

In addition, the PET AIFs and modified AIFs were fitted using the 6 parameter Feng input function model [Feng et al., 1993], shown in equation 6.3. Similarly, the fitted values of the gamma variate function's decay constant,λ_1, were compared. Results are shown in table 6.3. Similar to the previous 10 parameter AIF fit results, very minor differences were seen between between the λ_1 parameters fitted in AIF pairs, verifying that λ_1 of the PET-AIF could be obtained from the MRI-AIF with an average absolute error of 1.81% and maximum error of 3.52% for this group of patients.

6.6 Discussions and Conclusions

We proposed an AIF model which could fit ^{18}F-Cho and ^{18}F-FMISO derived AIFs with a good accuracy. This AIF model consist of convolution of a double But-

terworth function, which represent the injection of the tracer/contrast agent, with a tri-exponential function which represent its clearance. The width of the double Butterworth function can be increased or decreased to represent longer or shorter injection durations respectively. Fitting this AIF model to MRI-AIFs obtained using different injection durations showed a linear relationship between the width of the double Butterworth function and the injection duration. This linear relationship can be utilised to obtain prior information regarding some of the parameters of the AIF model when the injection duration is known.

Results of this work showed that ^{18}F-Cho derived input functions and DSC-MRI derived input functions have similar peak shapes in the early part of the input function, during the first pass bolus, when accounted for different injection durations used in the administration of the ^{18}F-Cho and Gd-based contrast agent. These similarities are due to the fact that the early part of an AIF is mainly dominated by the subject's blood flow and vascular characteristics, which are expected not to vary during PET and MRI acquisitions in a simultaneous PET/MRI scan. The PET derived and MRI derived AIFs started to differ approximately 20 seconds after the injection.

It was also seen that when fitted with our 10 parameter AIF model, κ_1 parameter of a PET-AIF can be obtained from a corresponding MRI-AIF with minor errors. Similarly, both AIFs yielded similar λ_1 values when corrected for different injection durations and fitted with Feng's input function model. These results can further be used to reduce the number of estimated AIF parameters in the simultaneous estimation method, described in chapter 5. If the injection duration of the PET tracer

is known, then the linear relationship between the injection duration and the width of the double Butterworth function can be used to estimate the width(τ_1-τ_2) of the PET-AIF.

In conclusion, we have shown that similar peak shapes between PET-AIF and MRI-AIF can be obtained even when different injection rates are used. This similarity can be used to derive some of the PET-AIF parameters from an MRI-AIF, which can be utilised to reduce the computational complexity of the PET simultaneous estimation method.

Chapter 7

Application of Constrained SIME to ^{18}F-FDG and ^{11}C-SB207145 tracers

7.1 Introduction

As described in detail in Chapter 5, SIME is a non-invasive image-based method to perform kinetic analysis of dynamic PET data without any need for a prior measurement of the input function. It requires input of multiple TACs from different brain regions and an involves estimation of the AIF together with the kinetic parameters. This method is computationally complex due to the large number of parameters estimated simultaneously and usually requires one or more arterial samples for AIF normalisation. We have previously shown with simulated ^{18}F-FDG data that the performance of SIME can be improved by introducing experimentally obtained prior information about the early part of the AIF [Sari et al., 2014].

In this chapter, the constrained SIME method with some prior AIF information is evaluated with clinical ^{18}F-FDG and ^{11}C-SB207145 [Marner et al., 2009] datasets

and is validated against the gold standard arterial blood sample derived AIFs. ^{11}C-SB207145 is a radioligand used in quantification of 5-HT$_4$ receptors in serotonin studies involved in memory and learning. During its metabolism, ^{11}C-SB207145 gets converted into metabolite products that recirculate in blood plasma. Therefore, it traditionally requires arterial blood sampling and metabolite analysis in order to measure the fraction of the parent compound for use in the kinetic analysis [Marner et al., 2009]. Results from pig studies have shown that ^{11}C-SB207145 distributes consistently in the brain regions with known 5-HT$_4$ densities, in the striatum, thalamus, cortical regions and cerebellum [Gee et al., 2008]. In this study, we used these regions within the SIME with and without prior AIF information and reported the results in this chapter. The aim of this work was to utilises prior AIF information to reduce the complexity of the SIME method and develop a methodology to analyse PET tracers non-invasively when radiometabolites are present in the blood plasma.

7.2 Materials and Methods

7.2.1 ^{18}F-FDG data

Data from the ^{18}F-FDG data study presented in Chapter 4 is used in this experiment. All of the studies were performed in Rigshospitalet, Copenhagen, Denmark and they were conducted in accordance to the Declaration of Helsinki. To briefly summarise the acquisition of the datasets, dynamic ^{18}F-FDG data were acquired using a Siemens Biograph 64mCT PET/CT scanner (Siemens Healthcare, Erlangen, Germany). Dynamic PET data were acquired for 1 hour and 19 PET frames were reconstructed using the following frame durations: 6 x 10 seconds, 2 x 30 seconds,

3 x 60 seconds, 2 x 150 seconds, 2 x 300 seconds and 3 x 600 seconds. 33 arterial blood samples were collected during the scan and AIF was measured from these samples as the gold standard AIF. For the early samples, 10 second intervals were used in order to get a good definition of the input function peak. The MRI scans were performed on a 3T Achieva MRI scanner (Philips Medical Systems, Best, The Netherlands) using a 32-channel phased array head coil. Acquisitions included MPRAGE and TOF-MRA sequences to obtain high resolution anatomical images.

Data from 10 subjects were included in the ^{18}F-FDG analysis. As also described in detail in chapter 4, carotid arteries were segmented from TOF-MRA images using ITK-SNAP v. 3.2 [Yushkevich et al., 2006]. The segmentation algorithm included a tissue classification pre-processing step followed by a region growing algorithm using evolving snakes. The segmented arteries covered the lower head and upper neck regions to match the field of view of the PET datasets. Dynamic PET frames were coregistered and resampled to MR angiography space using a two-step rigid registration with an intermediate registration to MPRAGE space. Coregistered PET frames were corrected for PV effects using the Single Target Correction (STC) method [Sari et al., 2016]. The mean activity in carotid arteries for each PET frame was computed to derive the C_{WB}

The Simultaneous estimation model was implemented to perform kinetic analysis of multiple brain regions, simultaneously estimating the AIF. For each subject, TACs from cerebellum, striatum, grey matter and white matter were extracted by manually placing ROIs on the PET images. An example of used TACs derived from one subject is illustrated in figure 7.1.

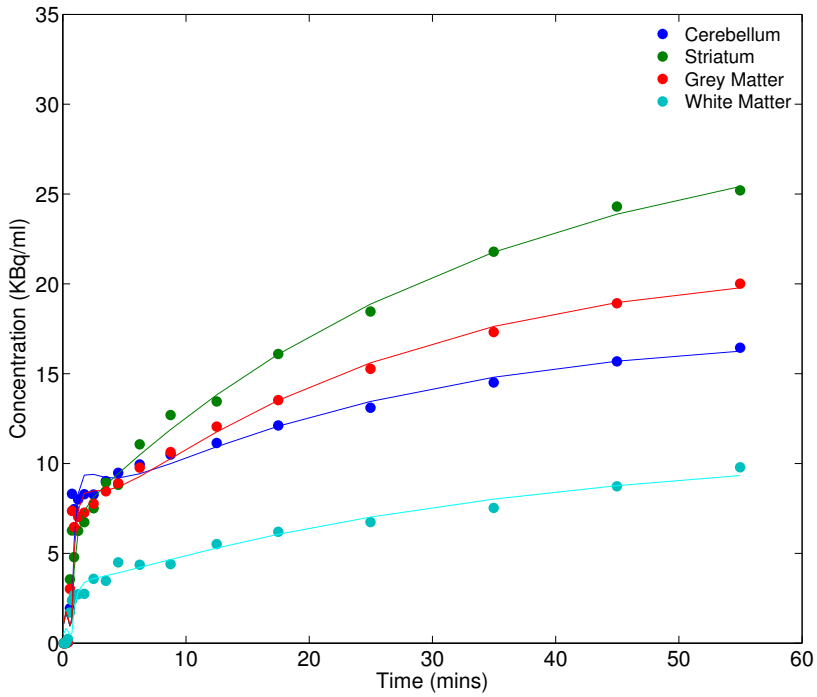

Figure 7.1: TACs used in the constrained ^{18}F-FDG SIME analysis. Cerebellum, striatum, grey matter, and white matter regions were used to derive the TACs.

All of the regions were modelled using a 2 tissue compartment model with 4 kinetic parameters (K_1, k_2, k_3, k_4) and cerebral blood volume (V_b). SIME was modelled using command line functions of COMKAT [Muzic and Cornelius, 2001] in MATLAB and parameter optimization was performed using the Ordinary Least Squares method with uniform weighting. The AIF was modelled using Feng's AIF model which consists of the sum of a gamma variate function with two exponentials [Feng et al., 1994] as in equation 7.1.

$$C_p(t) = (A_1 t - A_2 - A_3)e^{-\lambda_1 t} + A_2 e^{-\lambda_2 t} + A_3 e^{-\lambda_3 t} \tag{7.1}$$

Prior information regarding the early part of the AIF was obtained by fitting the PV corrected C_{WB} using the model shown in equation 7.1 and from the fitted A_1 and λ_1 values. The estimated values of these two parameters were used as an input to SIME model to reduce the number of estimated parameters. This was done by fixing the A_1 and λ_1 parameters of the SIME to the values obtained by fitting the C_{WB} curve. C_{WB} was also used in the estimation of V_b, as this parameter represents the fraction of the whole blood signal present in the volume of interest. We call the SIME with prior information derived from PV corrected C_{WB} the constrained SIME.

The SIME was also run with no existing prior information for comparison. In this model, V_b was linked to the AIF as the absence of whole blood concentration was assumed. AIF estimated using SIME and constrained SIME were used to fit the 4 brain TACs individually as performing this second fitting was previously shown to reduce the variation in the estimated parameters [Wong et al., 2002]. The 4 TACs were also fitted with the gold standard $AIF_{Samples}$. The influx constant (K_i) was computed for each region using the estimated microparameter values $(K_i{=}K_1k_3)/(K_2{+}k_3)$. Estimated K_i values were used in the comparison of SIME, constrained SIME and $AIF_{Samples}$.

7.2.2 [^{11}C]-SB207145 PET data

All of the scans of this test-retest study were performed at Copenhagen University Hospital, Rigshospitalet, Copenhagen, Denmark. This study was approved by the Ethics Committee for Copenhagen and Frederiksberg ((KF)01-274821). These data

have been collected for work previously published by Marner et al. [Marner et al., 2009].

Six healthy volunteers (3 males and 3 females, age range 21-44 years) were included in this test-retest study. The PET scans were performed on a 18-ring GE Advance scanner (GE Healthcare, Milwaukee, Wisconsin, USA). Each subject received an intravenous administration of the [^{11}C]-SB207145 tracer with a mean activity of 572 MBq (range of 512-601 MBq), with high specific activity (mean 48.4 GBq/μmol, range 34.2-71.0 GBq/μmol). A Dynamic PET scan was started before the administration and 3D PET data were acquired for 2 hours. Frames were binned using the following durations: 6x5s, 10x15s, 4x30s, 5x2min, 5x5min, 8x10min. 2D filtered back projection (6 mm Hann filter and 8.5 mm axial ramp filter) was used in the image reconstruction and the PET images were reconstructed on a 128 x 128 x 25 volumes with a voxel size of 2.0 mm x 2.0 mm x 4.25 mm. A CT scan was used for the attenuation correction. PET data were also corrected for randoms, scatter and deadtime.

Arterial blood samples were collected at 46 time points with 5 seconds interval in the early part of the scan to get a good definition of the bolus shape. Whole blood and plasma radioactivity concentration were measured in a well counter (COBRA 5003, Packard Instruments, Meriden, CT, USA). In addition, 7 arterial samples were withdrawn at times 3.5, 10. 17.5, 32.5, 55, 85, and 115 mins to measure the concentration of metabolites. The parent fraction was measured using a column-switching HPLC method [Gillings et al., 2007]. Subjects also had structural MRI scans on a 3T Siemens Trio Scanner (Siemens Healthcare, Erlangen, Germany). 3D T1-

weighted MPRAGE images of the whole head were acquired in saggital planes for each subject.

As high resolution TOF-MR Angiograms of carotid arteries were not collected as part of this study, T1 weighted MPRAGE images were used to segment the carotid arteries. One of the subjects had no blood signal on the MPRAGE image and it was excluded from the analysis as a reliable carotid artery segmentation was not possible. For the rest of the subjects, carotids were segmented using ITK-SNAP [Yushkevich et al., 2006]. As part of the segmentation preprocess, MPRAGE images were thresholded to keep the intensities above one third of the maximum image intensity. This step was performed to separate the carotid arteries from background regions with relatively high MR signal and replaced the automatic tissue classification method used in Chapter 4. Using tissue classification as preprocessing step did not yield acceptable results, possibly due to the proximity of carotid arteries to tissues with relatively high T1 signal. Once the MPRAGE images were thresholded, a region growing algorithm was applied to delineate the arterial voxels.

The dynamic PET frames were registered to the MPRAGE MR images using 6-parameter rigid registration. The first 10 frames (90 seconds) of the dynamic PET data was added together to have a summed image with high activity in carotid arteries. This summed image was used in the image registration. Image registration was performed using FSL Linear Image Registration Tool (FLIRT) [Jenkinson and Smith, 2001]. The resulting transformation matrix was used to coalign all of the PET frames to the MPRAGE image. PET frames were resampled to MR space using tri-linear interpolation. The coregistered PET images were corrected for PV effects

using the STC method with the segmented carotid artery mask as the region of interest. An empirically derived PSF FWHM of 6.8 was used in the PV correction. This PSF was derived using the image-based PSF derivation method [Sari et al., 2016] also presented in Chapter 4 of this thesis. The mean intensity in carotids for each PV corrected PET frame was computed to derive the C_{WB}.

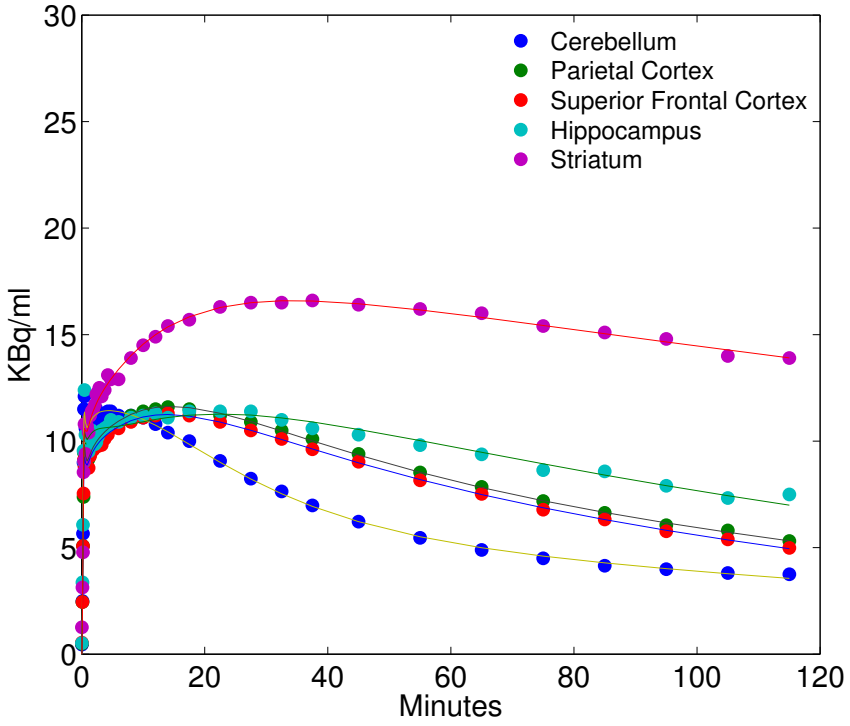

Figure 7.2: TACs used in the constrained [^{11}C]-SB207145 SIME analysis. Cerebellum, parietal cortex, superior frontal cortex, hippocampus and striatum were used to derive the TACs.

All of the brain TAC extraction work was performed at Rigshospitalet, Copenhagen, Denmark [Marner et al., 2009]. The T1 weighted MPRAGE image of each subject was coregistered to the 5th frame of the PET data and was parcellated into 19 different regions in left and right hemispheres automatically using Pvelab software package (www.nru.dk/downloads/software) [Quarantelli et al., 2004]. The derived

ROIs were applied to the PET data to extract the TACs. In our implementation, TACs from 5 different brain regions: cerebellum, parietal and frontal cortici, hippocampus and striatum were used in the SIME as they reflect low, moderate and high binding regions. These 5 TACs are illustrated in figure 7.2.

7.2.3 [^{11}C]-SB207145 Constrained SIME model

The [^{11}C]-SB207145 tracer can convert into metabolite side products once it is metabolised, making an AIF derived from PET images erroneous if it is used in the kinetic analysis without any separate metabolite correction. The original SIME model can be modified to perform this correction without any need for arterial samples. In traditional metabolite correction methods, a few arterial samples are collected during the PET scan and these are analysed to measure the concentration of metabolite products at different time points and hence derive the parent fraction. The obtained parent fraction can be modelled using a parametric function, such as a Hill function or constrained bi-exponential function and used to convert the plasma concentration to metabolite free parent concentration [Tonietto et al., 2016]. The Hill function can be written as equation 7.2.

$$f_{Hill}(t) = 1 - \frac{(1-a)t^b}{c+t^b} \tag{7.2}$$

In the presence of multiple brain TACs with varying kinetic behaviours, the SIME method can give an accurate estimation of metabolite free AIF by simultaneously fitting the TACs. However, due to its computational complexity and possible bias in the estimated parameters, SIME has to be complemented with a few plasma

samples obtained towards the end of the study. Arterial and venous samples obtained towards the end of a scan include a high fraction of radiometabolites and still require manual work to derive metabolite free concentrations. The constrained SIME method with prior image derived information regarding the A_1 and λ_1 of the AIF function can be used to reduce the complexity of the model and make a more reliable AIF estimation. The cost function of the constrained SIME can be written as following:

$$\phi(p) = \sum_{i=1}^{m} \sum_{j=1}^{n} w \left[E_i(t_j) - M_i(t_j)\right]^2$$

and

$$E_i = (1 - V_b) C_P(t) \otimes h_i[K_1, k_2, k_3, k_4] + V_b C_{WB}$$

where E_i is the estimated output, M_i the measured PET activity and h_i is the impulse response of the 2-TC compartmental model. Parameter m represent the number of TACs to be fitted, n represents the number of samples for each TAC and w is the weight, which was set to 1 to apply uniform weighting.

This model was implemented to analyse the [^{11}C]-SB207145 datasets and fit the 5 TACs derived from multiple brain regions. Image derived C_{WB} curve is fitted using Feng's AIF model [Feng et al., 1994] and fitted A_1 and λ_1 values were used to fix these parameters in the constrained SIME method. The remaining 4 AIF parameters and kinetic parameters of each region was simultaneously estimated using OLS optimisation. This method was further extended by introducing a second step

with an additional constraint by fitting the estimated parent fraction using the Hill function. The ratio of the SIME estimated C_P and the image derived C_{WB} was computed to determine the SIME derived parent fraction which was fitted using the Hill function. Then, the final AIF was estimated using equation 7.3.

$$C_P(t) = C_{WB}(t) f_{Hill}(t) C_{ratio}(t) \tag{7.3}$$

Where f_{Hill} is the fitted Hill function and C_{ratio} is the ratio of plasma to whole blood concentration as a function of time. In this study, a population based C_{ratio} was used to convert the whole blood concentration to plasma concentration. In order to derive this population based ratio, C_{ratio} of each dataset was computed by fitting a straight line through the plasma to whole blood concentrations derived from arterial samples. The mean of fitted ratios was computed to be used as the population based C_{ratio}. This ratio and the variance between subjects is illustrated in figure 7.7.

The constrained SIME method which was described above can be further simplified by combining the two steps into a single optimisation step. If the C_{WB} can accurately be measured from PET images, the relationship expressed in equation 7.3 can directly be incorporated into the SIME where the 3 parameters of the Hill function is estimated by simultaneously fitting the TACs. In other words, instead of modelling the AIF by estimating 6 parameters, 3 parameters of the Hill function can be estimated to derive the AIF utilising additional prior information. In our implementation, as illustrated in figure 7.4, the 5 TACs were simultaneously fitted by estimating the Hill function parameters (a, b, c) which is multiplied with image

derived whole blood concentration and a population based plasma to whole blood tracer concentration ratio to derive the actual AIF.

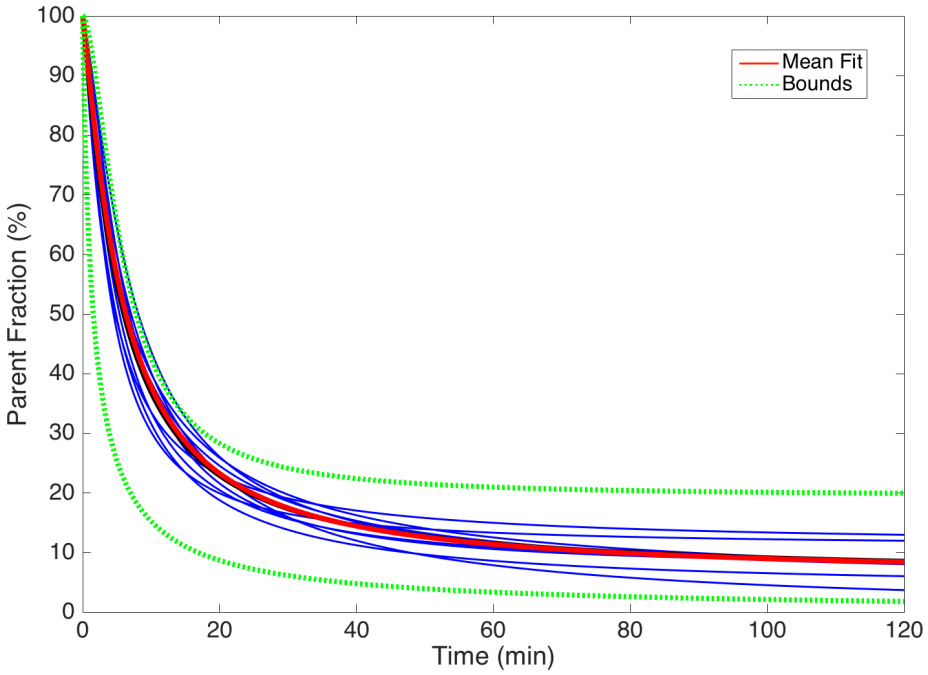

Figure 7.3: Parent fractions of 10 subjects fitted with the Hill function. The red curve represents the average of all fitted curves and green curves represent the bounds in 4 standard deviations.

Parent fraction curves derived from blood samples of each subject were fitted using the Hill function. The mean value of the 10 parent fractions was calculated and used as the starting point of the Hill function in the SIME optimizaton (a=0.0591, b=1.1816, c=7.7934). Upper and lower bounds of Hill function parameters were set to be within 4 standard deviations of the mean Hill function. The mean Hill function and the bounds used in this analysis is illustrated in figure 7.3.

$$V_T = \frac{K_1}{k_2}\left(1+\frac{k_3}{k_4}\right) \tag{7.4}$$

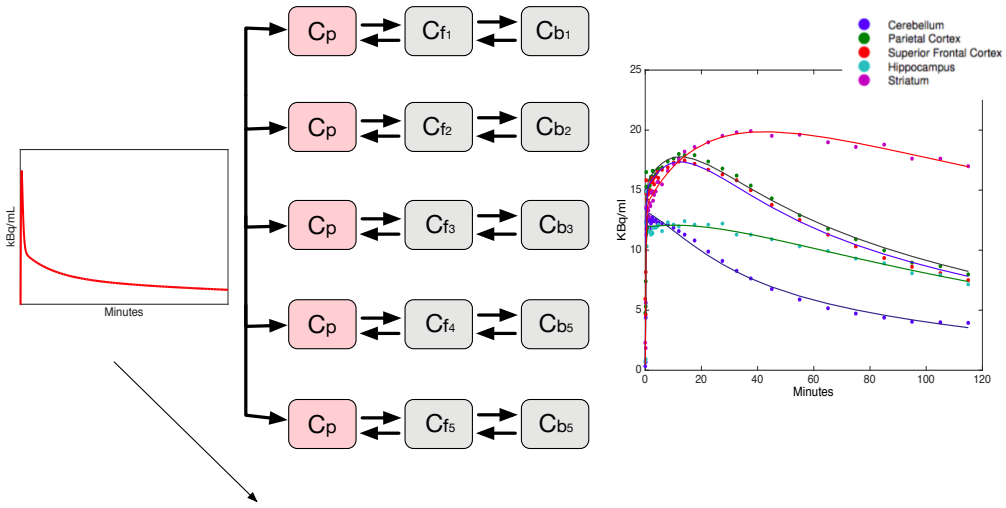

$$C_P(t) = C_{WB}(t)\left(1 - \frac{(1-a)t^b}{c+t^b}\right)C_{ratio}$$

Figure 7.4: Constrained SIME model used to analyse [^{11}C]-SB207145 tracer. The AIF was modelled as product of C_P, plasma to whole blood ratio and Hill function. 3 parameters of the Hill function (a, b, c) were optimised simultaneously by fitting 5 TACs measured from different brain regions. C_{WB} is derived from PV corrected PET images and population based plasma to whole blood ratio, C_ratio is derived by measuring the average plasma to whole blood concentration ratio across test and retest studies of 10 subjects

This AIFs derived using the original SIME, the constrained SIME and the simplified constrained SIME were used to fit each TAC individually to obtain the kinetic parameters, K_1, k_2, k_3, and k_4. Volume of distribution (V_T) in each region was computed using equation 7.4. The gold standard AIF derived from metabolite corrected arterial samples was also used to perform kinetic analysis of each region. Kinetic parameter and V_T estimates obtained using each AIF were used in comparing methods and validation against arterial samples.

Since results were present from test and retest studies, reliability of the proposed methods could be quantified by computing the intraclass correlation coefficient (ICC) between these studies, which was done using:

$$\mathrm{ICC} = \frac{\mathrm{BMS} - \mathrm{WMS}}{\mathrm{BMS} + \mathrm{WMS}} \tag{7.5}$$

where BMS is the mean sum of squares between subjects and WMS is the mean sum of squares between the test and retest studies for each subject. Equation 7.5 produces a score between -1 and +1 which represent minimum reliability and maximum reliability respectively.

Finally the identifiability of the proposed method was tested in terms of the number of different ROIs and the kinetic variation between the extracted brain TACs. This was done by running the experiment in an ideal scenario where the errors in image derived whole blood extraction and plasma to whole blood ratio were minimized. Different combinations of TACs were generated by utilizing TACs from cerebellum, hippocampus and superior frontal cortex and SIME with fitted Hill function was performed with these TACs. Whole blood concentration and plasma to whole blood ratio were derived from arterial samples to minimize potential errors which could be caused by PV correction and use of population based plasma to whole blood ratio. Accuracy of estimated V_T values were compared against V_T estimates using the gold standard arterial sample derived AIFs.

7.3 Results

7.3.1 ^{18}F-FDG Results

The results of the ^{18}F-FDG analysis are summarised in this section. Figure 7.5 illustrated the results for K_i macroparameter averaged across 10 patients. Results are

plotted for each brain region and each method: The original SIME method with no prior AIF information, the constrained SIME method with prior information from an image derived AIF, and arterial blood samples. The results show that introducing the prior AIF information improved the accuracy of the results for all of the four regions and brought the K_i estimates closer to the values estimated using the gold standard arterial samples. The SIME method yielded K_i estimates with 29.7% error for cerebellum, 38.8% for Striatum, 48.6% for grey matter and 47.9% for white matter. Introducing the prior AIF information reduced these errors to 4.4%, 5.1%, 6.6%, and 5.1% for each region respectively. These averaged results show that the constrained SIME slightly overestimated K_i for striatum, grey matter and white matter but slightly underestimated for cerebellum. The original SIME method overestimated the $K_i$for all of the regions.

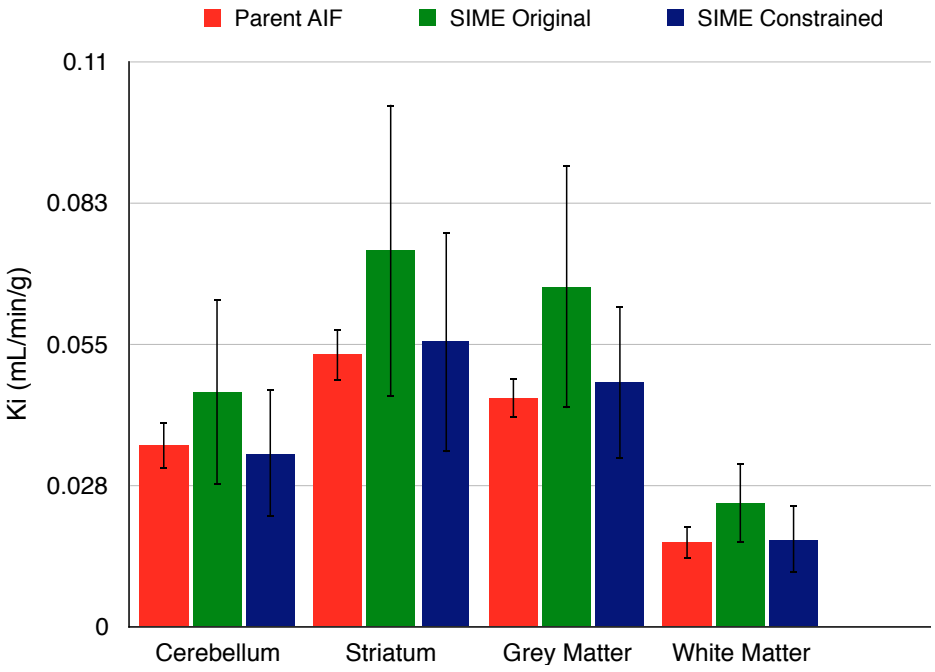

Figure 7.5: K_i parameter values estimated using SIME, Constrained SIME and arterial blood samples. Averaged results are illustrated for cerebellum, striatum, grey matter and white matter.

Results for individual kinetic parameters, K_1, k_2, k_3 and k_4 are shown in figure 7.6. A similar trend to K_i results was observed for K_1 parameters and the errors in parameter estimates were reduced for all of the regions with the introduction of prior AIF information. Using the SIME with no prior information estimated the K_1 parameter with the following percentage errors: 26.5% for cerebellum, 21.0% for striatum, 27.2% for grey matter and 34.9% for white matter. Using the constrained SIME reduced these errors to 12.5% for cerebellum, 5.8% for striatum, 19.1% for grey matter and 16.9% for white matter. Similarly, an improvement in the k_2 parameter estimates was observed with the introduction of the prior information where the absolute percentage error in estimates was reduced from 28.6% to 11.3% for cerebellum, 40.8% to 23.5% in striatum, 27.2% to 5.3% for grey matter and 14.3% to

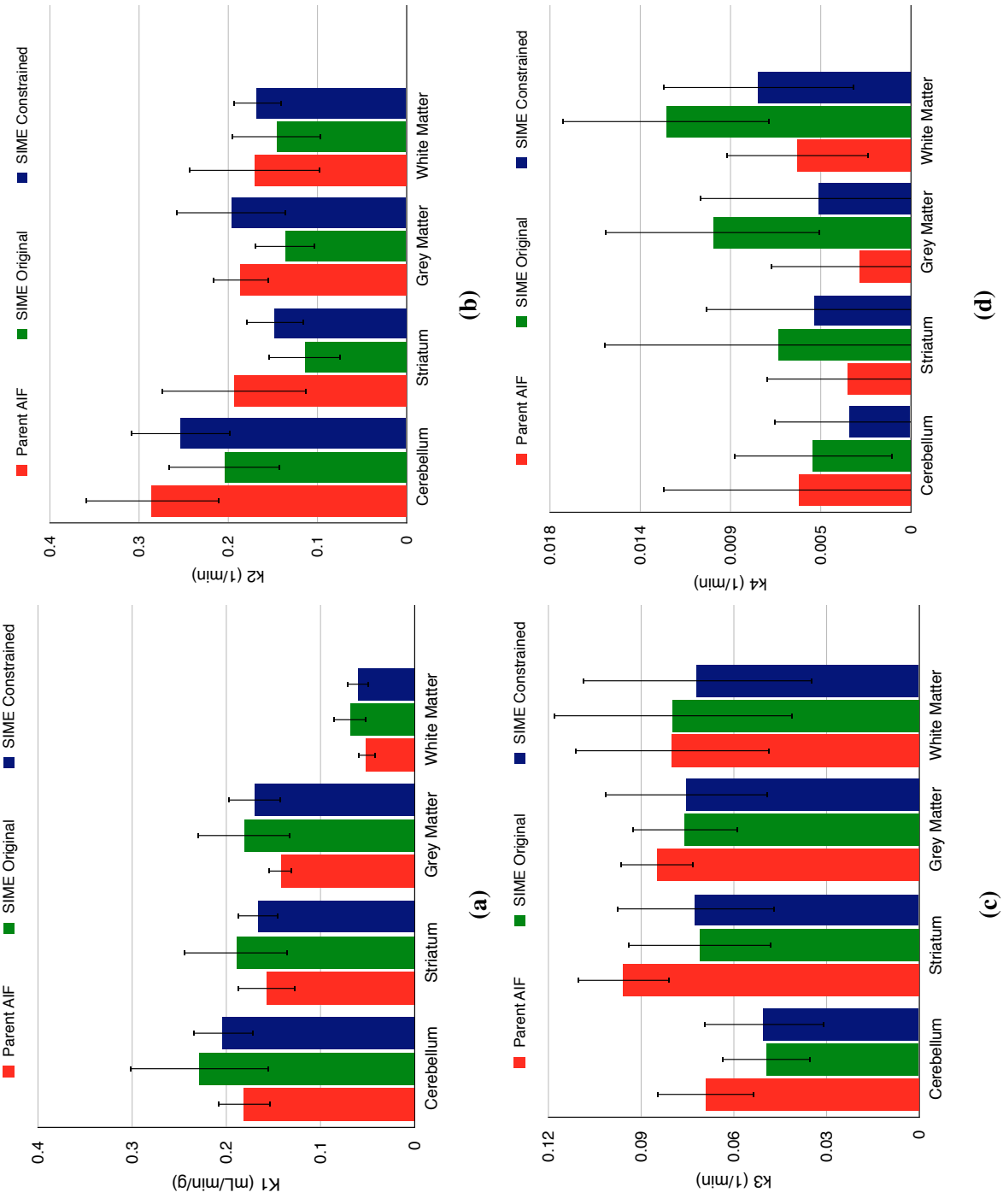

Figure 7.6: Individual kinetic parameter values estimated using SIME, Constrained SIME and arterial blood samples. Averaged results are illustrated for cerebellum, striatum, grey matter and white matter.

1.6% for white matter.

SIME and Constrained SIME methods yielded similar k_3 estimates with almost identical errors against arterial samples for cerebellum, striatum and grey matter. For white matter, the original SIME estimated k_3 with a very small error (0.4%) where constrained SIME produced underestimated k_3 with an average percentage error of 10.1%. Finally, constrained SIME reduced the percentage error in k_4 estimates compared to the SIME in 3 of the 4 regions (111.4% to 54.5% for striatum, 287.8% to 80.7% for grey matter and 117.8% to 35.6% for white matter). For cerebellum, the SIME method underestimated k_4 with 12.6% error where constrained SIME underestimated this parameter with 44.8% error averaged across 10 subjects.

7.3.2 [^{11}C]-SB207145 Results

In this section, results of the [^{11}C]-SB207145 are reported and performances of different methods used to derive the AIF and fit the brain TACs are compared. Throughout this section, the AIF derived from metabolite-corrected arterial samples is referred as $\text{AIF}_{\text{Samples}}$, the original SIME method with no prior information as SIME, the constrained SIME with image derived prior information regarding the two AIF parameters is referred as $\text{SIME}_{\text{Constrained}}$, the constrained SIME method with the second constrain using the Hill function is referred as $\text{SIME}_{\text{Constrained2}}$ and finally, the SIME method where the Hill function parameters are estimated instead of AIF parameters is referred as $\text{SIME}_{\text{Hill}}$.

The plasma to whole blood ratio of arterial samples of each dataset is plotted in figure 7.7 together with fitted straight lines for each dataset. The average of

all fitted lines was computed and is also plotted on the same figure. A reasonable variance was observed among the datasets which can be reliably represented using the averaged line. The fitted plasma to whole blood concentrations varied between 0.9 and 1.1 during the two-hour scan for 8 of the datasets whereas two datasets had steeper slopes, representing faster changes happening between plasma and whole blood concentrations.

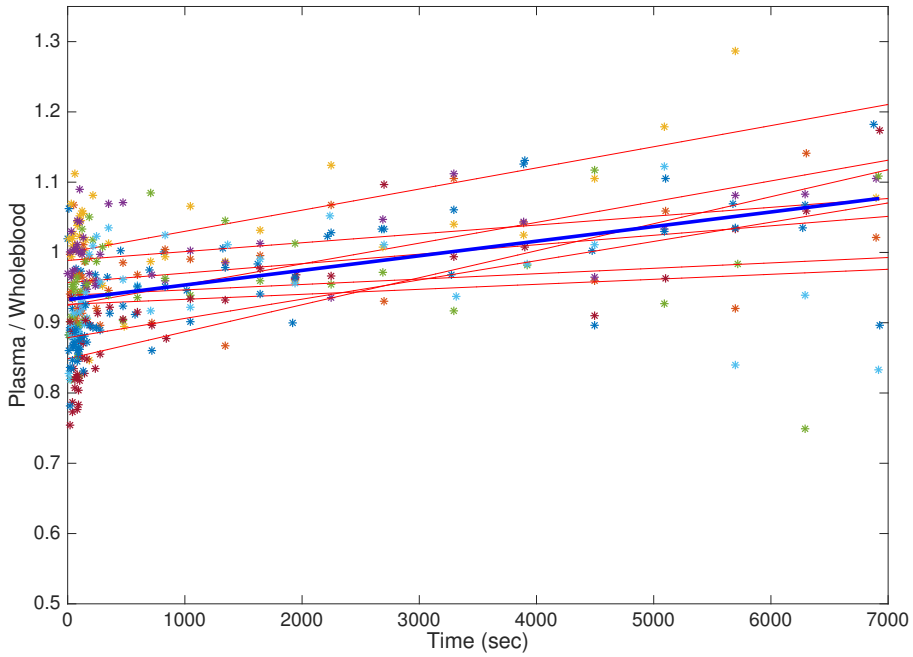

Figure 7.7: The population based plasma to whole blood ratio used in [^{11}C]-SB207145 analysis derived by averaging the plasma to whole blood ratio of each dataset fitted using a straight line. The red lines represent the fitted plasma to whole blood curve of each dataset and the blue line represents the mean ratio which is used in the data analysis.

The accuracy of the image derived whole blood TAC measurement was assessed by comparing the AUCs between image derived whole blood curves (WB_{ID}) and blood sample derived whole blood curves ($WB_{Samples}$). Examples of these two curves are illustrated in figure 7.8. Figure 7.9 shows the comparison of AUCs be-

tween whole blood curves derived using both methods. A good agreement between the WB_{ID} and $WB_{Samples}$ was observed in 9 of 10 subjects. In one subject, the WB_{ID} had half AUC compared to the $WB_{Samples}$. The reason for this is unknown but may be due to errors propagated from segmentation and coregistration steps.

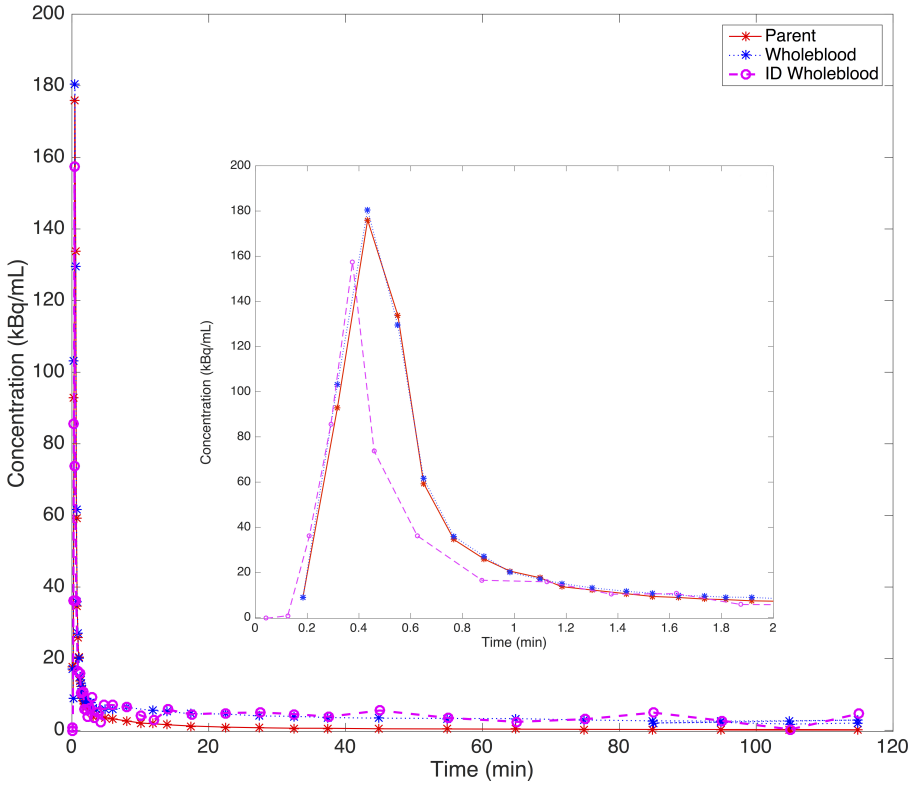

Figure 7.8: Comparison of image derived and blood sample whole blood curves for one subject plotted together with the metabolite free parent AIF derived from blood samples. The first two minutes were also separately plotted to zoom on the curve peaks

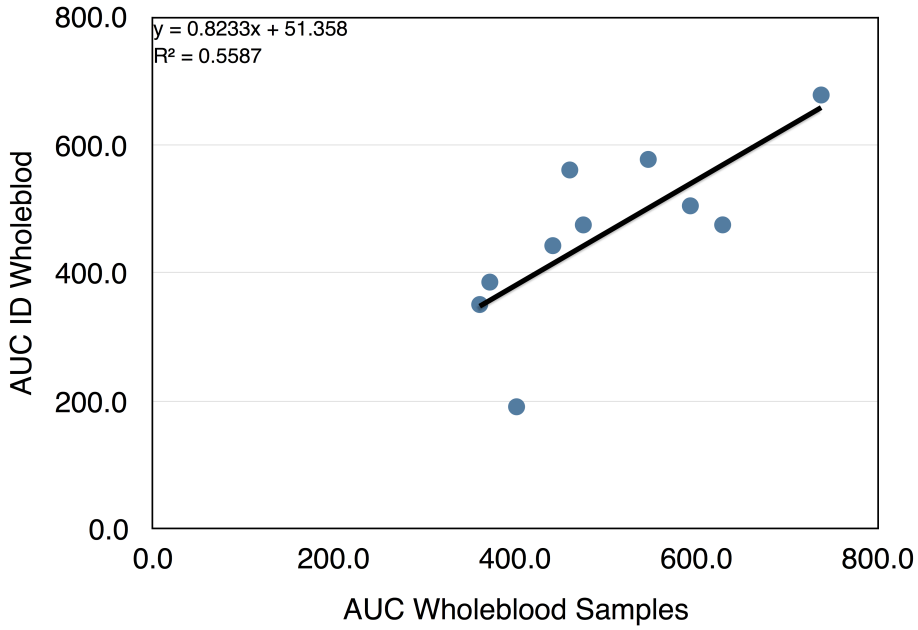

Figure 7.9: Comparison of area under curves between image derived and blood sampled derived whole blood curves.

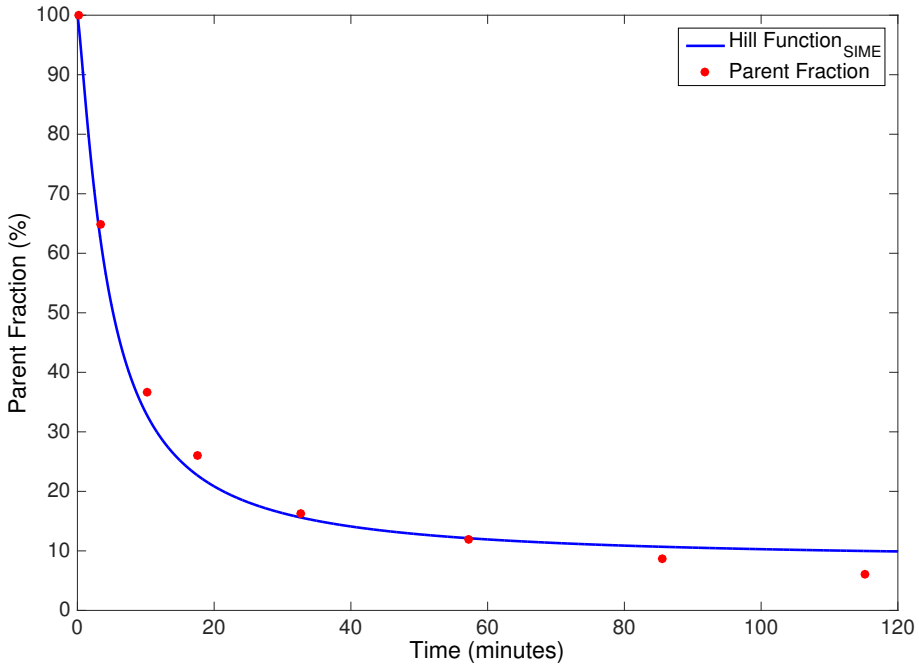

Figure 7.10: Average of the parent fractions estimated using $\text{SIME}_{\text{Hill}}$ plotted together with averaged parent fraction derived from plasma samples. The curves are mean of parent fractions measured for each of the 10 datasets

The $SIME_{Hill}$ was applied to optimise the parameters of the Hill function which was used together with image derived whole blood TAC to derive the metabolite free AIF. Figure 7.10 illustrates the mean of the fitted Hill functions plotted together with the blood sample derived parent fractions averaged across 10 datasets. A good agreement was observed in the early part of the this pair of averaged parent fraction curves. The curves started to deviate approximately 60 minutes after the injection. The fitted Hill functions overestimated the tail of the parent fraction curve which might cause higher AUC under derived AIFs.

$SIME_{Constrained2}$ was used to estimate the metabolite free AIF, utilising information from the WB_{ID} curve, a separate Hill function constrain and a population based plasma to whole blood ratio. The AUC of these estimated AIFs were calculated and compared to the AUC of metabolite corrected AIFs derived from arterial blood samples. This comparison is illustrated in figure 7.11 and it can be seen that AUC of AIF pairs in all of the 10 datasets correlated linearly, including the one dataset where a difference was previously observed between image derived and blood sample derived whole blood curves.

After the metabolite free AIF was computed using the listed methods, TACs derived from cerebellum, parietal cortex, superior frontal cortex, hippocampus and striatum were individually fitted using a 2-tissue compartmental model and the derived AIFs. The mean V_T results are illustrated in figure 7.12 and averaged kinetic parameter results obtained using the three different methods are shown in figure 7.13.

Figure 7.12 illustrates volume of distribution values for each region, averaged

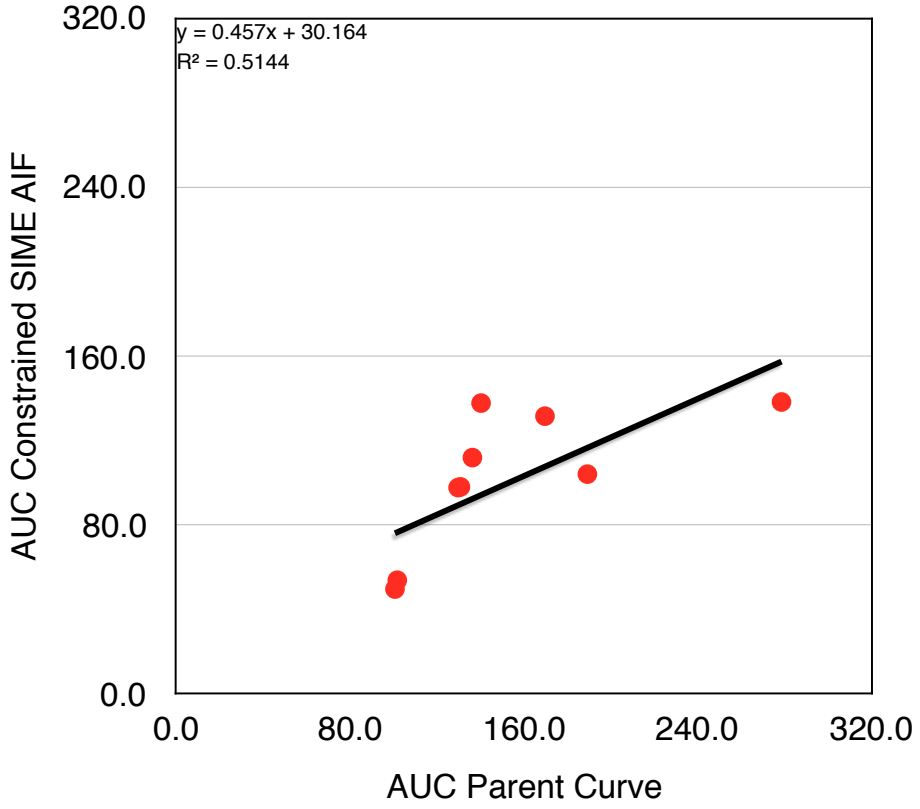

Figure 7.11: Comparison of area under curves between constrained SIME derived and blood sampled derived parent AIF curves.

across 10 datasets, estimated using each of the different AIF estimation techniques. It is shown that SIME with no prior information produced V_T estimates with largest difference to arterial samples for all of the 5 regions. The SIME yielded estimates with 60% error for cerebellum, 49% for parietal cortex, 41% for superior frontal cortex, 52% for hippocampus and 65% for striatum. Introducing the prior information for the A_1 and λ_1 parameters reduced this percentage error to to 42% for cerebellum, 31% for parietal cortex, 31% for superior frontal cortex, 20% for hippocampus and 51% for striatum. $\text{SIME}_{\text{Constrained2}}$ with two fixed parameters and an additional constrain applied by fitting a Hill function yielded more accurate V_T estimates, further reducing the percentage error to 13%, 11%, 17%, 12% and 25% for

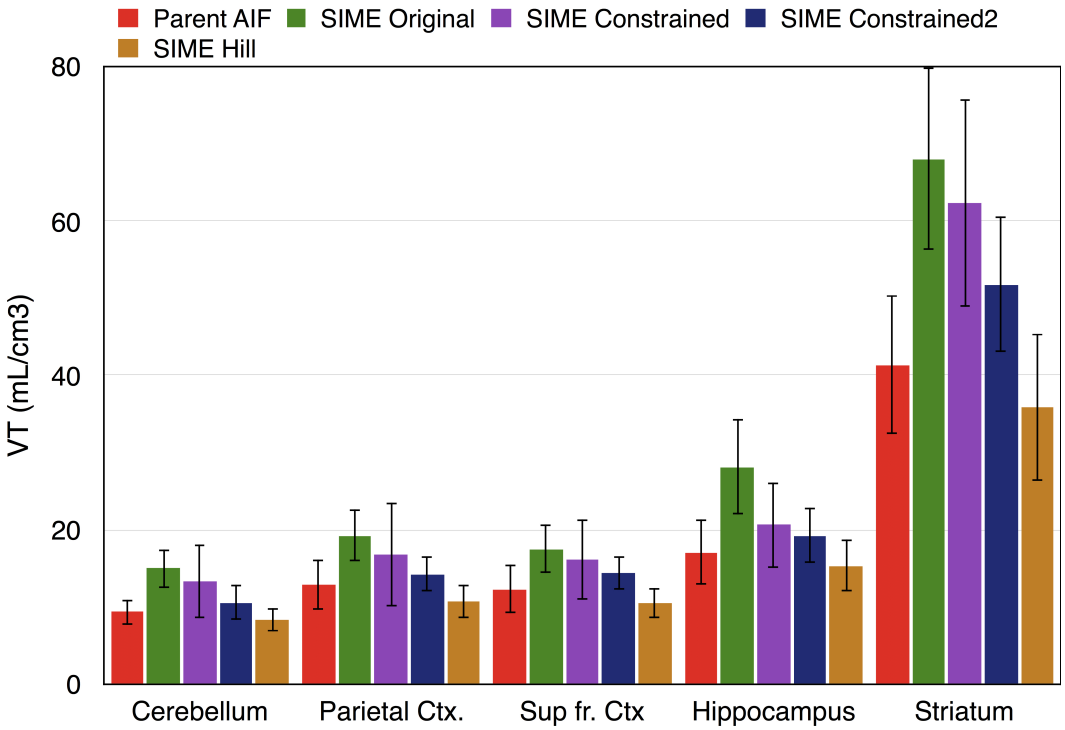

Figure 7.12: V_T estimated for each of the 5 regions using the AIFs derived from arterial samples, SIME, $\text{SIME}_{\text{Constrained}}$, $\text{SIME}_{\text{Constrained2}}$, and $\text{SIME}_{\text{Hill}}$. The bars represent the averaged V_T estimates across 10 datasets and error bars represent the standard deviation between the datasets.

these regions respectively. $\text{SIME}_{\text{Hill}}$ estimated V_T with a comparable performance to $\text{SIME}_{\text{Constrained2}}$, with absolute percentage errors of 10% error for cerebellum, 16% for parietal cortex, 15% for superior frontal cortex, 10% for hippocampus and 13% for striatum. It was observed that $\text{SIME}_{\text{Hill}}$ underestimated the V_T parameter in all of the 5 regions where the other methods produced overestimated V_T values.

As can be seen in figure 7.13, a similar improvement in K_1 estimates was observed between SIME, $\text{SIME}_{\text{Constrained}}$, and $\text{SIME}_{\text{Constrained2}}$ as more prior information was introduced. Even though $\text{SIME}_{\text{Constrained2}}$ showed the best performance among these three methods, it still yielded K_1 estimates with a percentage error of 14% for cerebellum, 22% for parietal cortex, 14% for superior frontal cortex, 19% for hippocampus and 12% for striatum. However, the less complex $\text{SIME}_{\text{Hill}}$

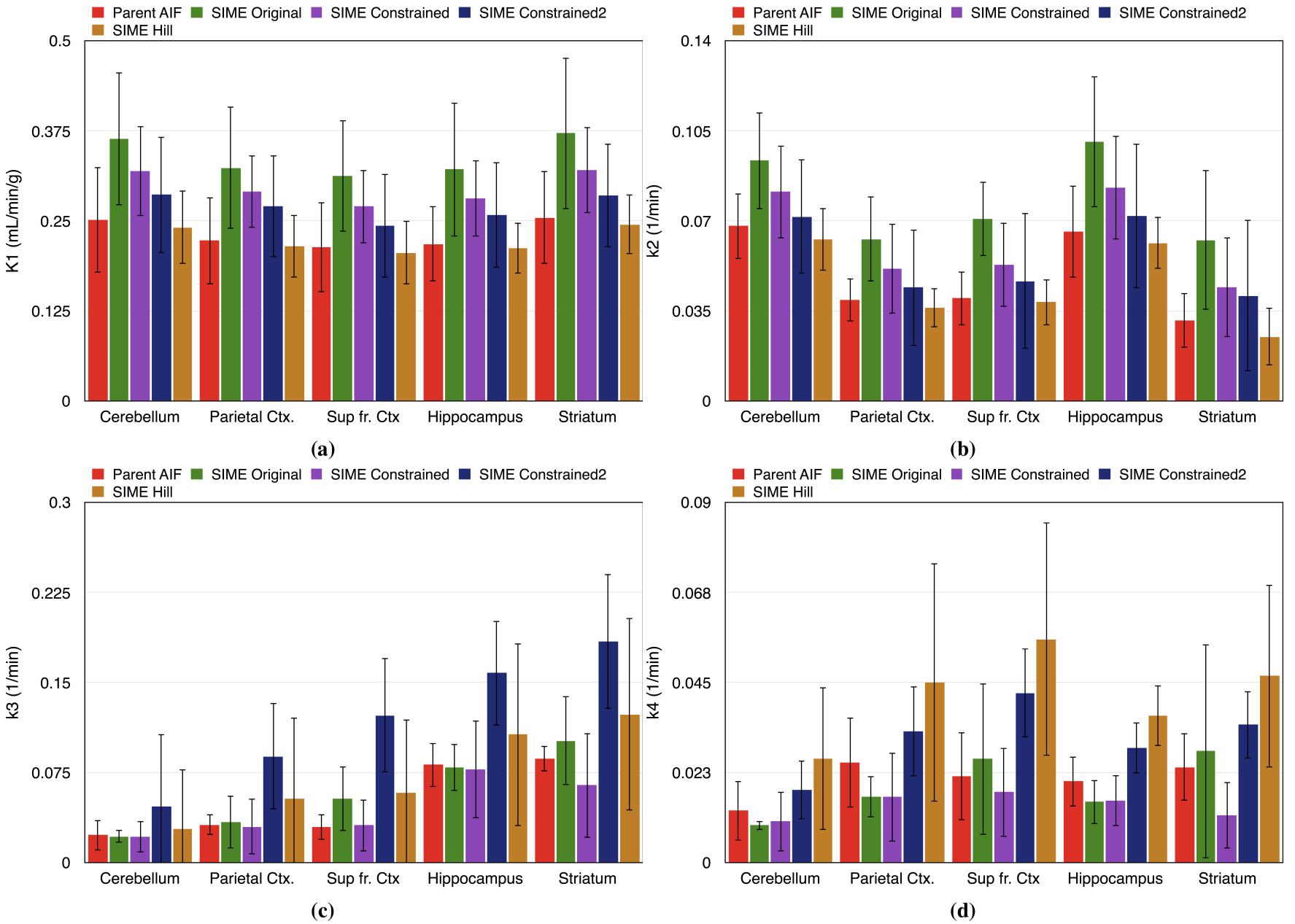

Figure 7.13: Kinetic parameters estimated for 5 brain regions using SIME, $\text{SIME}_{\text{Constrained}}$, $\text{SIME}_{\text{Constrained2}}$, and $\text{SIME}_{\text{Hill}}$. The bars represent the kinetic parameter values averaged across 10 subjects and error bars represent the standard deviation.

method yielded the most accurate K_1 estimates among all these methods where the percentage error improved notably and dropped to 4% for cerebellum, parietal cortex, superior frontal cortex, and striatum and 3% for hippocampus. Similar to V_T results, $SIME_{Hill}$ produced underestimated K_1 values whereas the SIME, $SIME_{Constrained}$ and $SIME_{Constrained2}$ overestimated this parameter in all regions.

Figure 7.13b shows that $SIME_{Hill}$ produced most similar k_2 estimates to arterial samples followed by $SIME_{Constrained2}$ and $SIME_{Constrained}$ whereas SIME with no prior information had the parameter k_2 with largest error. It was seen that $SIME_{Hill}$ underestimated this parameter with absolute percentage errors of 8% for cerebellum and parietal cortex, 3% for superior frontal cortex, 7% for hippocampus and 20% for striatum whereas $SIME_{Constrained2}$ was able to recover this parameter with 5%, 12%, 17%, 9%, and 30% percentage errors respectively. Similar to V_t and K_1 results, $SIME_{Hill}$ was the only method to underestimate k_2 parameter in average. Figure 7.13c illustrates that SIME and $SIME_{Constrained}$ estimated the k_3 parameter accurately in overall, whereas $SIME_{Constrained2}$ and $SIME_{Hill}$ produced estimates with greater errors. $SIME_{Constrained2}$ particularly estimated this parameter with a large error where the k_3 values estimated using this technique had a large percentage error (greater than 100%) for all of the regions with a large standard deviation. $SIME_{Hill}$ was also not able to recover the k_3 parameter accurately and yielded estimates with a percentage error of 23% for cerebellum, 70% for parietal cortex, 95% for superior frontal cortex, 31% for hippocampus and 42% for striatum. Finally, SIME and $SIME_{Constrained}$ showed the best performance in estimating the k_4 parameter where a comparable performance were observed in all of the regions apart from striatum.

Table 7.1: Estimated V_Ts using different number and variations of TACs. Results obtained using AIF samples are present to stand as the true ground. The percentage errors against the gold standard V_T for each method and each region are included. The following TACs are removed to generate the different TAC sets: 4 TACs: sup. fr. cortex, 4 TACs 2: cerebellum, 3 TACs: cerebellum and sup. fr. cortex, 3 TACs 2: cerebellum and hippocampus, 2 TACs: cerebellum, sup. fr. cortex, and hippocampus.

	Striatum		**Par. Ctx.**		**Sup. Fr. Ctx.**		**Hippocampus**	
	V_T	% Error	V_T	% Error	V_T	% Error	V_T	% Error
AIF Samples	42.14	-	13.77	-	12.62	-	17.07	-
5 TACs	37.19	11.7	12.23	11.2	10.66	15.5	15.89	6.9
4 TACs	39.35	4.2	11.89	13.6	-	-	15.33	10.2
4 TACs 2	35.74	15.2	11.36	17.5	10.22	19.0	-	-
3 TACs	29.07	31.0	10.05	27.0	8.89	29.6	-	-
3 TACs 2	25.39	39.7	8.25	40.1	-	-	10.91	36.1
2 TACs	28.33	32.8	9.24	32.9	-	-	-	-

Introducing further prior information regarding the parent fraction caused the k_4 to differ more compared to arterial samples. $\text{SIME}_{\text{Constrained2}}$ produced estimates with 51% overestimation averaged across 5 regions whereas $\text{SIME}_{\text{Hill}}$ overestimated this parameter by 103% averaged across 5 regions.

Table 7.1 shows the effects of using different number of TACs and TACs with different kinetic variation on the performance of the $\text{SIME}_{\text{Hill}}$ method. It can be seen from '4 TACs' that removing the superior frontal cortex TAC, which has similar kinetics to parietal cortex, has improved the V_T estimates in Striatum and reduced the percentage error from 11.7% to 4.2%. This percentage error increased to 15.2% when TAC derived from hippocampus was removed instead (shown as 4 TACs 2). Similar results were observed for parietal cortex, where the percentage error was 13.6% when TAC from cerebellum was included compared to 17.5% where TAC from superior frontal cortex was included instead. Using 3 TACs in the analysis increased this percentage error to the range of 27% to 40.1%, significantly worse

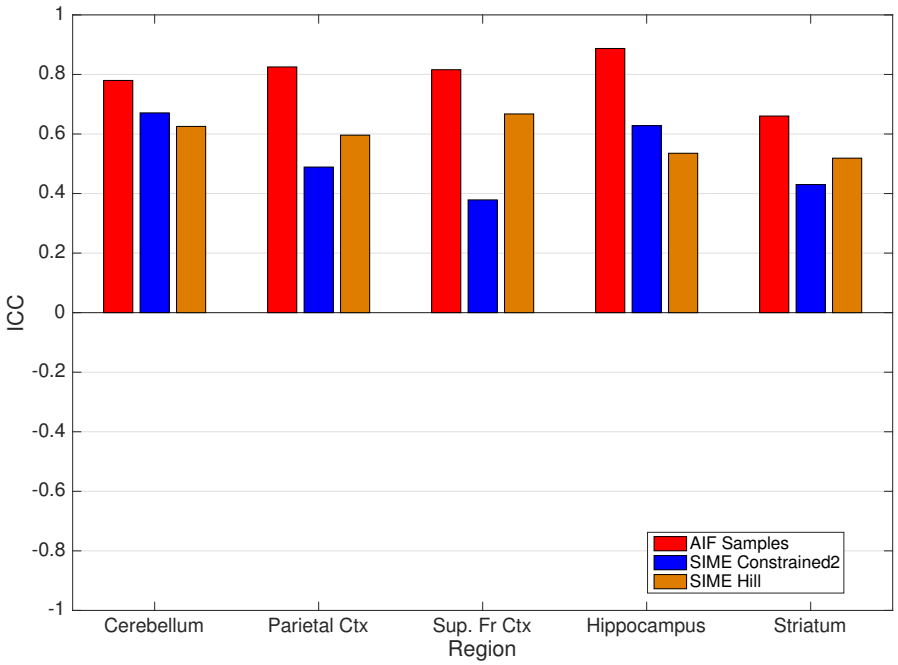

Figure 7.14: Intraclass Correlation Coefficient (ICC) of V_T estimates showing the reliability of the V_T according to test-retest results. Maximum reliability is represented as +1 where minimum reliability is represented by -1.

than results obtained using 4 TACs. Similar to the previous results, using 3 TACs with a larger kinetic variation yielded more accurate estimates than 3 TACs with poorer kinetic variation ('shown as 3 TACs 2'). Using 2 TACs with different kinetics produced estimates significantly better than 3 TACs with similar kinetics and with comparable accuracy to 3 TACs with different kinetics. Overall, these results indicate that using 4 or more regions in the analysis improved the performance of the $\text{SIME}_{\text{Hill}}$ method whereas increasing the kinetic variation between the TACs further improved the accuracy of the estimates.

The intraclass correlation coefficient (ICC) results shown in figure 7.14 indicates the reliability of the $\text{SIME}_{\text{Constrained2}}$ and $\text{SIME}_{\text{Hill}}$ by comparing the V_T estimates obtained in test and retest studies. The SIME and $\text{SIME}_{\text{Constrained2}}$ were

not included in this analysis as previous results had shown that these two methods produced less accurate V_T estimates. In this figure, positive 1 represents the maximum reliability whereas the negative 1 represents the minimum reliability. The ICC results of these two methods were compared against the ICC score of V_T estimates calculated using $AIF_{Samples}$. It can be seen that both $SIME_{Constrained2}$ and $SIME_{Hill}$ had positive ICC values in all of the 5 regions, showing that these methods had reliable performances, yielding similar results between test and retest studies. However, both of these SIME methods produced estimates with lower reliability compared to gold standard arterial samples. It can be said that $SIME_{Constrained2}$ and $SIME_{Hill}$ had comparable performances in overall as they had similar ICC scores in 4 of the 5 regions. $SIME_{Hill}$ had noticeably higher ICC score in superior frontal cortex compared to $SIME_{Constrained2}$

7.4 Discussions and Conclusions

In this chapter, our work to incorporate prior image-derived AIF information in the SIME analysis of dynamic PET is presented. Different methods with various amount of prior information were evaluated and results were presented. Anatomical MR images were used with the Single Target Correction PVC method to get a good measurement of whole blood TAC. Results in Chapter 4 had showed that this method could reliably be used to obtain the image derived input function in ^{18}F-FDG studies. In this chapter, a similar method was used to derive the whole blood concentration in [^{11}C]-SB207145 tracer studies and results indicated that the proposed method could return an accurate measurement of the whole blood concen-

tration with similar results to gold standard arterial samples.

The Constrained SIME approach with prior information derived from IDIF or whole blood concentrations was implemented to analyse ^{18}F-FDG and [^{11}C]-SB207145 studies. For the ^{18}F-FDG analysis, the method was used to derive the AIF by fitting TACs from cerebellum, striatum, grey matter, and white matter. The derived AIF was used to perform kinetic analysis of these ROIs individually to derive kinetic parameters (K_1-k_4) and calculate the influx constant, K_i. Results indicated that the original SIME approach with no prior information overestimated the K_i in all of the ROIs compared to the K_i values estimated using arterial samples. Introducing the prior information derived from the IDIF reduced this error and improved the accuracy of K_i estimates. The greatest improvement was seen in the K_1 andk_2 parameter estimates whereas less improvement was observed in the k_3 and k_4 estimates.

An adapted version of the constrained SIME was used to analyse [^{11}C]-SB207145 serotonin receptor studies. Kinetic analysis of this tracer requires information about concentration of metabolite products which is traditionally done using arterial sampling. SIME method could be a non-invasive alternative to analyse such tracers but it was observed that it produced large amount of errors in the estimated parameters when no blood sampling was performed to normalise the AIF. Using prior AIF information derived from PV corrected whole blood curves improved the K_1, k_2 and more importantly V_T estimates which is one of the main sought parameters in the analyses of this tracer. It was also observed that modelling the parent fraction during the optimisation also helped to further improve the performance of

the SIME, bringing results closer to gold standard arterial samples.

We also presented a simplified version of the constrained SIME, called $\text{SIME}_{\text{Hill}}$ which can be used to analyse tracers with radiometabolites. Instead of fitting the estimated parent fraction separate to SIME, the parent function model was incorporated into the SIME cost function and its parameters were estimated simultaneously with kinetic parameters of multiple ROIs. This method has the advantage of having less parameters than constrained SIME method as it fits three parameters of the Hill function, which is a parametric function of the parent fraction, rather than six parameters of the AIF. The fitted Hill function was multiplied with the image derived whole blood TAC and a population based plasma to whole blood concentration to derive the metabolite free AIF. Results showed that $\text{SIME}_{\text{Hill}}$ was able to recover the AIF correctly and was able to estimate V_T , K_1, and k_2 with good accuracy. The two latter are the parameters which are directly linked to AIF which be the reason behind these findings. The intraclass coefficient results showed that both $\text{SIME}_{\text{Constrained2}}$ and $\text{SIME}_{\text{Hill}}$ had reliable performance in estimating V_T in test and retest studies. In overall it can be said that $\text{SIME}_{\text{Hill}}$ had a slightly better performance compared to $\text{SIME}_{\text{Constrained2}}$ and can be favoured in practice as it has reduced number of parameters to estimate within the SIME cost function.

The proposed $\text{SIME}_{\text{Hill}}$ requires an accurate measurement of the whole blood curve from PET images and knowledge of a model which can be used to define the parent fraction which can be specific to the used tracer [Tonietto et al., 2016]. Results of this work showed that the percentage error on V_T estimates was halved when a 4th TAC was added. This percentage error was further reduced when the

4th TAC had a different kinetic behaviour from the rest of the TACs. Therefore, it can be conluded that at least 4 TACs are required for accurate V_T estimates and reliability of the method can be improved as the differentiability between the TACs is increased.

In this work, we presented results using the Hill function which had been previously shown as a suitable function to fit blood sample derived parent fraction curves in [^{11}C]-SB207145 studies. Constrained bi-exponential curves with 3 parameters is also an alternative function which can be used to analyse [^{11}C]-SB207145 [Marner et al., 2009]. An accurate definition of the plasma to whole blood ratio can be essential for the analysis of some tracers, where large amount of binding occurs in red blood cells. The errors present in the population based plasma to whole blood ratio used in this work could be one of the reasons for the observed differences between SIME derived and blood sample derived AIFs.

The constrained SIME method can be an alternative method to estimate the kinetic parameters in ^{18}F-FDG PET studies without any need for blood sampling. It requires presence of a suitable carotid artery in the field of view and a high resolution anatomical MR image of head and neck region to perform a reliable artery segmentation. However, as we are able to derive an IDIF in ^{18}F-FDG PET studies, the constrained SIME can be a more complex and less practical way of estimating kinetic parameters. The constrained SIME can be particularly useful if the tail of an IDIF is affected by motion artefacts or high amount of noise in the reconstructed PET images. In such cases, an accurate definition of the AIF peak can be adequate to derive an accurate definition of kinetic parameters using the constrained SIME.

In addition, the AIF derived from a SIME method will be free of delay and dispersion whereas an IDIF derived from a common carotid artery might slightly suffer from these effects.

The constrained SIME, or more practical $SIME_{Hill}$ can be used to eliminate the need for arterial sampling for the analysis of PET tracers with radiometabolite products present in the blood plasma. In order to use these methods, the dynamic PET acquisition had to be complemented with anatomical MR images such as T1 weighted MPRAGE, or preferably TOF-MR angiograms to be used in artery segmentation. This method can potentially be used to analyse other PET tracers where the binding to red blood cells is slow and tracer concentration in plasma and whole blood are similar in the early part (first 60 seconds) of the scan upon tracer injection. A slow formation of the metabolite products is also essential to use this method in derivation of the parent AIF. For instance, if a PET tracer uptake is present in the lungs, radiometabolite products can rapidly form and return to blood plasma during the first pass of the tracer, causing differences in the early parts of parent AIF and whole blood TACs. An AIF derived from a dynamic MRI study can be also be used to derive information regarding the early part of the AIF, which will not be affected by these changes in parent plasma and whole blood PET tracer concentrations. Dynamic MR techniques also benefit from their high temporal resolution abilities to produce a more accurate definition of the AIF peaks. Similarities between PET derived and MR derived AIFs were presented in chapter 6 and but use of an MRI derived AIF in PET SIME is still needs to be validated in clinical studies.

In conclusion, this chapter present a method which can be used to non-

invasively analyse dynamic PET data, even in the presence of radiometabolites. Anatomical MR images were used with STC PVC method to get a good measurement of whole blood TAC. The parent fraction of the tracer in the plasma was modelled using a parametric equation with parameters estimated using constrained SIME. The product of whole blood TAC, constrained SIME derived parent fraction and population derived plasma to whole blood relationship was computed to obtain the AIF. The proposed method was able to derive V_T, K_1 and k_2 parameters accurately. Parameters k_3 and k_4 could be derived with larger errors.

Chapter 8

Conclusions and future work

8.1 Conclusions

As a result of growing interest in the PET community to use novel tracers in neuroreceptor studies as well as to quantify the tumour diagnosis in oncology studies, increasing attention is being given to using dynamic studies which can provide a more detailed quantification of the system of interest compared to traditional Standard Uptake Value measurements. Dynamic PET data can be analysed using kinetic modelling techniques where an accurate measurement of the arterial input function, the concentration of parent tracer in plasma over time, is required. The gold standard method to obtain the AIF requires withdrawal of multiple arterial samples during the course of the PET scan which are further analysed to measure the concentration of tracer in plasma for each sample. Due to its invasiveness and the labouring work it requires to obtain the AIF, arterial sampling is often avoided in clinical practice.

There has been an increasing amount of work to develop less invasive and

more automatic methods which can measure image derived input functions from PET images. In the presence of a suitable artery or vascular structure in the PET field of view, the changing concentration of tracer in the blood can be measured by placing a volume of interest and measuring the activity for each PET frame. However, accuracy of a such measurement directly from PET images is restricted by the low spatial resolution and high statistical variance of the PET data. Furthermore, radiometabolites, which are radioactive side products which can form in the body organs and return to blood plasma contributing to the blood signal, can make measurement of an IDIF more challenging.

With the commercial availability of the hybrid PET/MR scanners, excellent soft tissue contrast and high spatial resolution of MR images can be easily acquired and used to complement the quantitative information obtained from PET data. In this work, we used time of flight MR Angiography images with high blood signal contrast to perform an accurate segmentation of the common carotid arteries from lower head and upper neck region. Dynamic ^{18}F-FDG PET frames were registered to MRA space and partial volume correction of PET images was performed using Single Target Correction method. The STC method can be a practical way of performing PVC for IDIF measurement applications as it only requires the segmentation of carotid arteries and does not require additional parcellation of background regions. The performance of the implemented IDIF measurement method was compared to gold standard arterial samples in ^{18}F-FDG studies and results have shown that the proposed method was able to recover the AIF accurately and obtain cMRGlc estimates with no statistically significant difference to arterial samples. The

proposed method was also applied to measure the wholeblood TAC from [^{11}C]-SB207145 PET images and an accurate TAC could be measured in the vast majority of the datasets.

Kinetic analysis of dynamic MRI data also requires a reliable measurement of the AIF, which represents the concentration of Gadolinium based contrast agent in the blood plasma. We studied the presence of any mutual information between PET derived and MR derived AIFs and tested if a reliable AIF conversion between modalities can be performed. The different injection durations used in the administration of PET tracer and MRI contrast agent had to be accounted for before an AIF conversion can be made. We proposed an AIF model which can model the effects of the used injection duration on the AIF bolus shapes and allows the adjustment of PET and MRI AIFs to same injection durations. We have analysed 4 pairs of AIFs derived from [^{18}F]fluorocholine PET and DSC-MRI datasets using this model and observed similar bolus shapes in the early part of the AIFs once the differences caused by different injection durations were elimiated. The early part of the input function is dominated by blood flow and vascular characteristics, which are expected to be similar if the PET and MRI acqusitions are performed simultaneously or on the same day. The two AIFs started to deviate after the recirculation as the PET tracer and Gadolinium contrast agent have different clearance and washout characteristics. Results showed that parameters representing the early part of the AIF could be converted reliably from PET to MRI or vice versa. It can be argued that using an MRI technique with a high temporal resolution over PET with limited temporal sampling abilities can be advantageous since the rapid changes happening

in the early part of the AIF can be defined more accurately.

Simultaneous estimation method is another image-based method which can be used to derive the AIF simultaneously by fitting multiple TACs from different tissue regions. This method has the ability to recover a metabolite-free AIF in the presence of metabolites in the blood but often suffer from computational complexity due to large number of parameters estimated at once. SIME is usually accompanied by one or more blood samples to normalize the estimated AIF. It can be hypothesised that information derived from a reliable image-based blood measurements with PV correction or from an MRI derived AIF can be used as prior information to decrease the number of parameters simultaneously estimated in the SIME method, reducing the computational complexity. We showed that the early part of a parameterised PET-AIF can be accurately measured from an MRI-AIF and this information can be used to fix some of the AIF parameters to priorly measured values. Results from analysis of simulated ^{18}F-FDG data showed that incorporating the prior information highly improved the parameter estimation and reduced the bias on the estimated K_i values.

The wholeblood curves which can be measured with a good accuracy using the proposed IDIF extraction method was also used to reduce the difficulties faced in the SIME method. For the PET tracers with negligible uptake in the lungs and red blood cells, the radiometabolites start to build in the blood plasma after the first recirculation. Hence, it can be said that early peak of a wholeblood curve will be minimally affected for these tracers and similar shapes between wholeblood TAC and parent AIF boluses are expected to be seen. We have utilised this phenomenon

to developed a constrained SIME, called $SIME_{constrained}$ and where fitted image derived wholeblood TACs were used to fix two of the AIF parameters in the SIME. As a proof of concept, this method was firstly tested on ^{18}F-FDG data obtained from healthy volunteers. Similar to results of the simulations study, introducing prior AIF information improved the AIF recovery and the accuracy of the parameter estimation. The constrained SIME method was also used to noninvasively analyse dynamic [^{11}C]-SB207145 PET datasets which traditionally requires arterial blood samples for metabolite correction. Similar to ^{18}F-FDG analysis results, using constrained SIME with less parameters improved the accuracy of estimated parameters. It was also observed that introducing additional constrains by modelling the parent fraction, the ratio of metabolite free parent tracer concentration to plasma concentration, using a parametric model further improved the SIME performance.

As results indicated that modelling the parent fraction yielded more accurate kinetic parameter and volume of distribution estimations, we developed a simplified version of the $SIME_{constrained}$ called $SIME_{Hill}$. In this model, the parent fraction was modelled using a parametric model called the Hill function with three parameters. Instead of directly estimating the AIF parameters in the SIME, parameters of the Hill function were estimated by fitting multiple TACs from different brain regions. The product of the image derived wholeblood curve, SIME fitted Hill function and a population based wholeblood to plasma curve was computed to derive the metabolite free AIF. It was observed that using this AIF was able to estimate V_T, and 2 of the 4 microparameters, K_1, and k_2, accurately with similar results to arterial samples. The results showed that the proposed method with prior information derived

from image derived wholeblood curve and modelled parent fraction can be used as an alternative noninvasive method to perform kinetic analysis of tracers with metabolite products.

8.2 Future work

In this section, several recommendations to extend the work reported in this thesis are listed.

- Due to the lack of availability of arterial blood samples together with dynamic PET and dynamic MRI data, the constrained SIME method with MR derived prior AIF information was never fully validated. Since an MR-compatible serial blood sampling equipment, such as Swisstracer [Alf et al., 2013] was not available, we were not able to design an in-house experiment to perform dynamic PET acquisition, dynamic MR acquisition and arterial blood sampling to measure the PET tracer concentration for gold standard AIF measurements. [^{18}F]fluorocholine PET and DSC-MRI datasets were used to study the similarities between PET and MRI derived AIFs but this work was not extended to be analysed using SIME since [^{18}F]fluorocholine has limited uptake in the brain which prevents extraction of multiple TACs and hence use of SIME for the analysis of this tracer. Future work can include design of a more comprehensive experiment with simultaneous dynamic PET and MRI acquisitions complemented with an arterial blood sampling protocol to evaluate the incorporation of MRI-AIF derived information into analysis of dynamic PET data using constrained SIME approach and validate the results against gold

standard arterial sample derived AIFs.

- The SIME method requires input of at least 3 TACs with varying kinetic behaviours for a reliable performance. In this work, we used both manual and automatic method to extract TACs from different brain regions. However, the TACs were examined manually to choose regions with different kinetics. This can be extended by implementing a clustering algorithm to automatically choose TACs with different uptake and binding patterns. A similar technique was presented by Guo et. al [Guo et al., 2003], where a distance measurement was applied to cluster voxel derived TACs. A similar technique was also applied to automatically extract a suitable reference region in brain PET studies [Yaqub et al., 2012]. Automatic extraction of TACs can improve the accuracy of SIME method as it can determine TACs with the highest kinetic variations more easily than manual observations.

- In this work, ITK-SNAP was used for the segmentation of carotid arteries from TOF-MR Angiography images with a clustering and region growing algorithm. The region growing stage requires the user to input initial starting points on each carotid artery which later expands in 3D and delineate the arterial voxels. Even though this step only requires a minimal user input, an automatic carotid artery segmentation method can be used instead to speed up the IDIF extraction method. Adaptive segmentation methods for fully automatic segmentation of carotid arteries from TOF-MRA images are available in the literature [Wilson and Noble, 1999] [Bogunovic et al., 2011] and have

been accurately used in similar IDIF extraction methods [Su et al., 2013a] [Su et al., 2015].

- Currently, the Single Target Correction method assumes a single background region and corrects for spill-over effects by performing a voxelwise correction to the carotid arteries and the neighbouring background regions. The STC can be improved by implementing a voxel clustering algorithm to determine voxels with similar intensities and group them to automatically form multiple regions in the background. This can improve the performance of the PVC by reducing the noise present in the background region.

Bibliography

[Aerts et al., 2008] Aerts, H. J. W. L., van Riel, N. a. W., and Backes, W. H. (2008). System identification theory in pharmacokinetic modeling of dynamic contrast-enhanced MRI: influence of contrast injection. *Magnetic Resonance in Medicine*, 59(5):1111–9.

[Alf et al., 2013] Alf, M. F., Wyss, M. T., Buck, A., Weber, B., Schibli, R., and Krämer, S. D. (2013). Quantification of brain glucose metabolism by 18F-FDG PET with real-time arterial and image-derived input function in mice. *Journal of Nuclear Medicine*, 54(1):132–8.

[Arabi et al., 2015] Arabi, H., Rager, O., Alem, A., Varoquaux, A., Becker, M., and Zaidi, H. (2015). Clinical Assessment of MR-Guided 3-Class and 4-Class Attenuation Correction in PET/MR. *Molecular Imaging and Biology*, 17(2):264–276.

[Ashburner and Friston, 1999] Ashburner, J. and Friston, K. J. (1999). Nonlinear spatial normalization using basis functions. *Human Brain Mapping*, 7(4):254–266.

[Bauman et al., 2012] Bauman, G., Belhocine, T., Kovacs, M., Ward, a., Beheshti, M., and Rachinsky, I. (2012). 18F-fluorocholine for prostate cancer imaging: a systematic review of the literature. *Prostate Cancer and Prostatic Diseases*, 15(1):45–55.

[Berker et al., 2012] Berker, Y., Franke, J., Salomon, a., Palmowski, M., Donker, H. C. W., Temur, Y., Mottaghy, F. M., Kuhl, C., Izquierdo-Garcia, D., Fayad, Z. a., Kiessling, F., and Schulz, V. (2012). MRI-Based Attenuation Correction for Hybrid PET/MRI Systems: A 4-Class Tissue Segmentation Technique Using a Combined Ultrashort-Echo-Time/Dixon MRI Sequence. *Journal of Nuclear Medicine*, 53(5):796–804.

[Beyer et al., 2000] Beyer, T., Townsend, D. W., Brun, T., Kinahan, P. E., Charron, M., Roddy, R., Jerin, J., Young, J., Byars, L., and Nutt, R. (2000). A combined PET/CT scanner for clinical oncology. *Journal of Nuclear Medicine*, 41(8):1369–1379.

[Bogunovic et al., 2011] Bogunovic, H., Pozo, J. M., Villa-Uriol, M. C., Majoie, C. B., van den Berg, R., Gratama van Andel, H. A., Macho, J. M., Blasco, J., Roman, L. S., and Frangi, A. F. (2011). Automated segmentation of cerebral vasculature with aneurysms in 3DRA and TOF-MRA using geodesic active regions: an evaluation study. *Medical Physics*, 38(1):210–222.

[Bousquet et al., 1988] Bousquet, J. C., Saini, S., Stark, D. D., Hahn, P. F., Nigam, M., Wittenberg, J., and Ferrucci, J. T. (1988). Gd-DOTA: characterization of a new paramagnetic complex. *Radiology*, 166:693–698.

[Boussion et al., 2006] Boussion, N., Hatt, M., Lamare, F., Bizais, Y., Turzo, A., Cheze-Le Rest, C., and Visvikis, D. (2006). A multiresolution image based approach for correction of partial volume effects in emission tomography. *Physics in Medicine and Biology*, 51(7):1857–1876.

[Brownell et al., 1969] Brownell, G., Burnham, C., Wilensky, S., Aronow, S., Kazemi, H., and Strieder, D. (1969). New developments in positron scintigraphy and the application of cyclotron- produced positron emitters.

[Brownell and Sweet, 1953] Brownell, G. and Sweet, W. (1953). Localization of brain tumors with positron emitters. *Nucleonics*, 11:40–45.

[Burgos et al., 2015] Burgos, N., Cardoso, M. J., Thielemans, K., Modat, M., Dickson, J., Schott, J. M., Atkinson, D., Arridge, S. R., Hutton, B. F., and Ourselin, S. (2015). Multi-contrast attenuation map synthesis for PET/MR scanners: assessment on FDG and Florbetapir PET tracers. *European Journal of Nuclear Medicine and Molecular Imaging*, 42(9):1447–1458.

[Burgos et al., 2014] Burgos, N., Cardoso, M. J., Thielemans, K., Modat, M., Pedemonte, S., Dickson, J., Barnes, A., Ahmed, R., Mahoney, C. J., Schott, J. M., Duncan, J. S., Atkinson, D., Arridge, S. R., Hutton, B. F., and Ourselin, S. (2014). Attenuation correction synthesis for hybrid PET-MR scanners: Application to brain studies. *IEEE Transactions on Medical Imaging*, 33(12):2332–2341.

[Bushong and Clarke, 2013] Bushong, S. and Clarke, G. (2013). *Magnetic Resonance Imaging: Physical and Biological Principles*. Elsevier Health Sciences.

[Calamante, 2002] Calamante, F. (2002). Quantification of Perfusion Using Bolus Tracking Magnetic Resonance Imaging in Stroke: Assumptions, Limitations, and Potential Implications for Clinical Use. *Stroke*, 33(4):1146–1151.

[Calamante, 2013] Calamante, F. (2013). Arterial input function in perfusion mri: A comprehensive review. *Progress in Nuclear Magnetic Resonance spectroscopy*, 74:1 – 32.

[Calamante et al., 1999] Calamante, F., Thomas, D. L., Pell, G. S., Wiersma, J., and Turner, R. (1999). Measuring cerebral blood flow using magnetic resonance imaging techniques. *Journal of Cerebral Blood Flow and Metabolism*, 19(7):701–735.

[Carson et al., 2003] Carson, R., Barker, W., Liow, J.-S. L. J.-S., and Johnson, C. (2003). Design of a motion-compensation OSEM list-mode algorithm for resolution-recovery reconstruction for the HRRT. *2003 IEEE Nuclear Science Symposium. Conference Records*, 5.

[Catana et al., 2011] Catana, C., Benner, T., van der Kouwe, A., Byars, L., Hamm, M., Chonde, D. B., Michel, C. J., El Fakhri, G., Schmand, M., and Sorensen, A. G. (2011). MRI-Assisted PET Motion Correction for Neurologic Studies in an Integrated MR-PET Scanner. *Journal of Nuclear Medicine*, 52(1):154–161.

[Catana et al., 2012] Catana, C., Drzezga, A., Heiss, W.-D., and Rosen, B. R. (2012). PET/MRI for neurologic applications. *Journal of nuclear medicine : official publication, Society of Nuclear Medicine*, 53(12):1916–25.

[Catana et al., 2010] Catana, C., van der Kouwe, A., Benner, T., Michel, C. J., Hamm, M., Fenchel, M., Fischl, B., Rosen, B., Schmand, M., and Sorensen, A. G. (2010). Toward Implementing an MRI-Based PET Attenuation-Correction Method for Neurologic Studies on the MR-PET Brain Prototype. *Journal of Nuclear Medicine*, 51(9):1431–1438.

[Chan and Vese, 2001] Chan, T. F. and Vese, L. A. (2001). Active contours without edges. *IEEE Transactions on Image Processing*, 10(2):266–277.

[Chavhan et al., 2008] Chavhan, G. B., Babyn, P. S., Jankharia, B. G., Cheng, H.-L. M., and Shroff, M. M. (2008). Steady-state MR imaging sequences: physics, classification, and clinical applications. *Radiographics*, 28(4):1147–1160.

[Chawluk et al., 1990] Chawluk, J. B., Dann, R., Alavi, A., Hurtig, H. I., Gur, R. E., Resnick, S., Zimmerman, R. A., and Reivich, M. (1990). The effect of focal cerebral atrophy in positron emission tomographic studies of aging and dementia. *Int.J.Rad.Appl.Instrum.B*, 17(0883-2897):797–804.

[Chen et al., 1998] Chen, K., Bandy, D., Reiman, E., Huang, S.-C., Lawson, M., Feng, D., Yun, L.-s., and Palant, A. (1998). Noninvasive quantification of the cerebral metabolic rate for glucose using positron emission tomography, 18F-

fluoro-2-deoxyglucose, the Patlak method, and an image-derived input function. *Journal of Cerebral Blood Flow and Metabolism*, 18(7):716–723.

[Cheng et al., 2006] Cheng, K., Koeck, P. J. B., Elmlund, H., Idakieva, K., Parvanova, K., Schwarz, H., Ternstrom, T., and Hebert, H. (2006). Rapana thomasiana hemocyanin (RtH): comparison of the two isoforms, RtH1 and RtH2, at 19A and 16A resolution. *Micron*, 37(6):566–576.

[Cherry and Dahlbom, 2006] Cherry, S. R. and Dahlbom, M. (2006). *PET: Physics, Instrumentation, and Scanners*, pages 1–117. Springer New York, New York, NY.

[Choi et al., 1991] Choi, Y., Hawkins, R. a., Huang, S. C., Gambhir, S. S., Brunken, R. C., Phelps, M. E., and Schelbert, H. R. (1991). Parametric images of myocardial metabolic rate of glucose generated from dynamic cardiac PET and 2-[18F]fluoro-2-deoxy-d-glucose studies. *Journal of Nuclear Medicine*, 32(4):733–8.

[Committee, 2012] Committee, D. M. T. (2012). DCE MRI Quantification Profile, Quantitative Imaging Biomarkers Alliance. Ver.1.0. Reviewed Draft.

[Conti et al., 1996] Conti, P. S., Lilien, D. L., Hawley, K., Keppler, J., Grafton, S. T., and Bading, J. R. (1996). PET and [18F]-FDG in oncology: A clinical update. *Nuclear Medicine and Biology*, 23(6):717–735.

[Coombs et al., 1997] Coombs, B. D., Szumowski, J., and Coshow, W. (1997). Two-point Dixon technique for water-fat signal decomposition with B0 inhomogeneity correction. *Magnetic Resonance in Medicine*, 38(6):884–9.

[Cootes et al., 2004] Cootes, T., Twining, C., Taylor, C., and Babalola, K. (2004). Diffeomorphic Statistical Shape Models. *Procedings of the British Machine Vision Conference 2004*, 1:47.1–47.10.

[Crone, 1965] Crone, C. (1965). Facilitated transfer of glucose from blood into brain tissue. *The Journal of Physiology*, 181(1):103–13.

[Cunningham and Jones, 1993] Cunningham, V. J. and Jones, T. (1993). Spectral analysis of dynamic PET studies. *Journal of Cerebral Blood Flow and Metabolism*, 13(1):15–23.

[da Silva et al., 2013] da Silva, N. A., Herzog, H., Weirich, C., Tellmann, L., Kops, E. R., Hautzel, H., and Almeida, P. (2013). Image-derived input function obtained in a 3TMR-brainPET. *Nuclear Instruments and Methods in Physics Research Section A: Accelerators, Spectrometers, Detectors and Associated Equipment*, 702:22–25.

[Delso et al., 2011] Delso, G., Fürst, S., Jakoby, B., Ladebeck, R., Ganter, C., Nekolla, S. G., Schwaiger, M., and Ziegler, S. I. (2011). Performance Measurements of the Siemens mMR Integrated Whole-Body PET/MR Scanner. *Journal of Nuclear Medicine*, 52(12):1914–1922.

[Detre et al., 2012] Detre, J. A., Rao, H., Wang, D. J., Chen, Y. F., and Wang, Z. (2012). Applications of arterial spin labeled mri in the brain. *Journal of Magnetic Resonance Imaging*, 35(5):1026–1037.

[Dickson et al., 2015] Dickson, J., Erlandsson, K., Sari, H., Wan, S., and Groves, A. (2015). Partial volume correction of image derived input functions using a novel single target correction technique. *European Journal of Nuclear Medicine and Molecular Imaging, Hamburg 2015*, 42:S49.

[E.D. Morris, 2004] E.D. Morris, C.J. Endres, K. S. B. C. R. M. R. (2004). *Kinetic Modeling in Positron Emission Tomography*. Elsevier.

[Erlandsson et al., 2012a] Erlandsson, K., Buvat, I., Pretorius, P. H., Thomas, B. a., and Hutton, B. F. (2012a). A review of partial volume correction techniques for emission tomography and their applications in neurology, cardiology and oncology. *Physics in Medicine and Biology*, 57(21):R119–59.

[Erlandsson et al., 2012b] Erlandsson, K., Buvat, I., Pretorius, P. H., Thomas, B. A., and Hutton, B. F. (2012b). A review of partial volume correction techniques for emission tomography and their applications in neurology, cardiology and oncology. *Physics in Medicine and Biology*, 57(21):R119.

[Erlandsson et al., 2006] Erlandsson, K., Wong, A., van Heertum, R., Mann, J., and Parsey, R. (2006). An improved method for voxel-based partial volume correction in PET and SPECT. *Neuroimage*, (31):T84.

[Essig et al., 2013] Essig, M., Nguyen, T. B., Shiroishi, M. S., Saake, M., Provenzale, J. M., Enterline, D. S., Anzalone, N., Dörfler, A., Rovira, A., Wintermark, M., and Law, M. (2013). Perfusion MRI: the five most frequently asked clinical questions. *American Journal of Roentgenology*, 201:495–510.

[Evans, 2015] Evans, E. (2015). *Improved Quantification in Small Animal PET/MR*. PhD thesis, University of Cambridge.

[Evans et al., 2012] Evans, E., Sawiak, S. J., and Carpenter, T. A. (2012). MRI-derived arterial input functions for PET kinetic modelling in rats. *Nuclear Instruments and Methods in Physics Research, A*, pages 1–3.

[Fan et al., 2016] Fan, A., Khaligni, M. M., Gulaka, P., Guo, J., Holley, D., Gandhi, H., Shen, B., Park, J., Singh, P., Chin, F. T., and Zaharchuk, G. (2016). Comparison of cerebral blood flow from standard- and multi-delay arterial spin labeling MRI with [15O]-water PET by simultaneous PET/MRI. Conference on PET/MR and SPECT/MR.

[Feng et al., 1993] Feng, D., Huang, S. C., and Wang, X. (1993). Models for computer simulation studies of input functions for tracer kinetic modeling with positron emission tomography. *International Journal of Bio-medical Computing*, 32(2):95–110.

[Feng et al., 1994] Feng, D., Wang, X., and Yan, H. (1994). A computer simulation study on the input function sampling schedules in tracer kinetic modeling

with positron emission tomography (PET). *Computer Methods and Programs in Biomedicine*, 45(3):175–186.

[Feng et al., 1997] Feng, D., Wong, K. P., Wu, C. M., and Siu, W. C. (1997). A technique for extracting physiological parameters and the required input function simultaneously from PET image measurements: theory and simulation study. *IEEE Transactions on Information Technology in Biomedicine*, 1(4):243–54.

[Fletcher et al., 2008] Fletcher, J. W., Djulbegovic, B., Soares, H. P., Siegel, B. A., Lowe, V. J., Lyman, G. H., Coleman, R. E., Wahl, R., Paschold, J. C., Avril, N., Einhorn, L. H., Suh, W. W., Samson, D., Delbeke, D., Gorman, M., and Shields, A. F. (2008). Recommendations on the use of 18F-FDG PET in oncology. *Journal of Nuclear Medicine*, 49(3):480–508.

[Freeman et al., 1998] Freeman, A. J., Gowland, P. A., and Mansfield, P. (1998). Optimization of the ultrafast look-locker echo-planar imaging {T1} mapping sequence. *Magnetic Resonance Imaging*, 16(7):765–772.

[Fulton et al., 2002] Fulton, R., Meikle, S., Eberl, S., Pfeiffer, J., and Constable, C. (2002). Correction for head movements in positron emission tomography using an optical motion-tracking system. *IEEE Transactions on Nuclear Science*, 49(1):116–123.

[Fung and Carson, 2013] Fung, E. K. and Carson, R. E. (2013). Cerebral blood flow with [15O]water PET studies using an image-derived input function and

MR-defined carotid centerlines. *Physics in Medicine and Biology*, 58(6):1903–23.

[Gee et al., 2008] Gee, A. D., Martarello, L., Passchier, J., Wishart, M., Parker, C., Matthews, J., Comley, R., Gunn, R. H., and R (2008). Synthesis and Evaluation of [11C]SB207145 as the First In Vivo Serotonin 5-HT4 Receptor Radioligand for PET Imaging in Man.

[Geraldes and Laurent, 2009] Geraldes, C. F. G. C. and Laurent, S. (2009). Classification and basic properties of contrast agents for magnetic resonance imaging. *Contrast Media & Molecular Imaging*, 4(1):1–23.

[Gillan et al., 1992] Gillan, G. D., Nitz, W. R., and Brant-Zawadzki, M. (1992). MP RAGE: a three-dimensional, T1-weighted, gradient-echo sequence–initial experience in the brain. *Radiology*, 182(3):1–7.

[Gillings et al., 2007] Gillings, N., Marner, L., and Knudsen, G. (2007). Rapid, robust and fully automated method for analysis of radioactive metabolites in plasma samples from PET studies. *Journal of Labelled Compounds and Radiopharmaceuticals*, 50:S503.

[Graham et al., 2002] Graham, M. M., Muzi, M., Spence, A. M., OSullivan, F., Lewellen, T. K., Link, J. M., and Krohn, K. A. (2002). The FDG lumped constant in normal human brain. *Journal of Nuclear Medicine*, 43(9):1157–1166.

[Guo et al., 2003] Guo, H., Renaut, R., Chen, K., and Reiman, E. (2003). Clustering huge data sets for parametric PET imaging. In *BioSystems*, volume 71, pages 81–92.

[Guo et al., 2007] Guo, H., Renaut, R. A., and Chen, K. (2007). An input function estimation method for FDG-PET human brain studies. *Nuclear Medicine and Biology*, 34(5):483–492.

[Haaga, John R. Lanzieri and C., 2004] Haaga, John R. Lanzieri, C. F. and C., G. R. (2004). CT and MR Imaging of the Whole Body, 4th ed, 2 vols. *Radiology*, 232(2):324.

[Hawkins and Huang, 1986] Hawkins, R A, P. M. E. and Huang, S. C. (1986). Effects of temporal sampling, glucose metabolic rates, and disruptions of the blood-brain barrier on the FDG model with and without a vascular compartment: studies in human brain tumors with PET. *Journal of Cerebral Blood Flow and Metabolism*, 6(2):170–183.

[Henderson et al., 1999] Henderson, E., McKinnon, G., Lee, T.-Y., and Rutt, B. K. (1999). A fast 3D Look-Locker method for volumetric {T1} mapping. *Magnetic Resonance Imaging*, 17(8):1163–1171.

[Hofmann et al., 2008] Hofmann, M., Steinke, F., Scheel, V., Charpiat, G., Farquhar, J., Aschoff, P., Brady, M., Scholkopf, B., and Pichler, B. J. (2008). MRI-based attenuation correction for PET/MRI: a novel approach combining pattern

recognition and atlas registration. *Journal of Nuclear Medicine*, 49(11):1875–1883.

[Holt et al., 2011] Holt, A., Pasca, E., Heijmink, S., Teertstra, J., Muller, S., and Van der Heide, U. (2011). The impact of overall injection time on the arterial input function and pharmaco-kinetic analysis using the Tofts model in DCE-MRI for prostate cancer patients. *Magnetic Resonance in Medicine*, 66(5):1267–74.

[Hudson and Larkin, 1994] Hudson, H. M. and Larkin, R. S. (1994). Accelerated image reconstruction using ordered subsets of projection data. *IEEE Transactions on Medical Imaging*, 13:601–609.

[Iagaru et al., 2015] Iagaru, A., Mittra, E., Minamimoto, R., Jamali, M., Levin, C., Quon, A., Gold, G., Herfkens, R., Vasanawala, S., Gambhir, S. S., and Zaharchuk, G. (2015). Simultaneous Whole-Body Time-of-Flight 18F-FDG PET/MRI: A Pilot Study Comparing SUVmax With PET/CT and Assessment of MR Image Quality. *Clinical Nuclear Medicine*, 40(1).

[Ibaraki et al., 2005] Ibaraki, M., Shimosegawa, E., Toyoshima, H., Ishigame, K., Sugawara, S., Takahashi, K., Miuram, S., and Kanno, I. (2005). Evaluation of arterial input function for Perfusion MRI: comparison with that of PET study. *Proceedings of the International Society for Magnetic Resonance in Medicine*, 13(1):1125.

[Iida et al., 1988] Iida, H., Higano, S., Tomura, N., Shishido, F., Kanno, I., Miura, S., Murakami, M., Takahashi, K., Sasaki, H., and Uemura, K. (1988). Evaluation

of regional differences of tracer appearance time in cerebral tissues using [15O] water and dynamic positron emission tomography. *Journal of Cerebral Blood Flow and Metabolism*, 8(2):285–288.

[International Atomic Energy Agency, 2008] International Atomic Energy Agency (2008). A Guide to Clinical PET in Oncology: Improving Clinical Management of Cancer Patients. *International Atomic Energy Agency*, (October).

[Irving et al., 2013] Irving, B., Tanner, L., Enescu, M., Bhushan, M., Hill, E. J., Franklin, J., Anderson, E. M., Sharma, R. A., Schnabel, J. A., and Brady, M. (2013). *Abdominal Imaging. Computation and Clinical Applications: 5th International Workshop, Held in Conjunction with MICCAI 2013, Nagoya, Japan, September 22, 2013. Proceedings*, chapter Personalised Estimation of the Arterial Input Function for Improved Pharmacokinetic Modelling of Colorectal Cancer Using dceMRI, pages 126–135. Springer Berlin Heidelberg, Berlin, Heidelberg.

[Ishii et al., 1997] Ishii, K., Sasaki, M., Kitagaki, H., Yamaji, S., Sakamoto, S., Matsuda, K., and Mori, E. (1997). Reduction of cerebellar glucose metabolism in advanced Alzheimer's disease. *Journal of nuclear medicine : official publication, Society of Nuclear Medicine*, 38(6):925–928.

[Ishikawa et al., 1990] Ishikawa, M., Kikuchi, H., Nagata, I., Yamagata, S., Taki, W., Yonekura, Y., Nishizawa, S., Iwasaki, Y., and Mukai, T. (1990). Glucose consumption and rate constants for 18F-fluorodeoxyglucose in human gliomas. *Neurologia Medico-Chirurgica*, 30:377–381.

[Izquierdo-Garcia et al., 2014] Izquierdo-Garcia, D., Sawiak, S. J., Knesaurek, K., Narula, J., Fuster, V., Machac, J., and Fayad, Z. A. (2014). Comparison of MR-based attenuation correction and CT-based attenuation correction of whole-body PET/MR imaging. *European Journal of Nuclear Medicine and Molecular Imaging*, 41(8):1574–1584.

[Jahng et al., 2014] Jahng, G. H., Li, K. L., Ostergaard, L., and Calamante, F. (2014). Perfusion magnetic resonance imaging: A comprehensive update on principles and techniques. *Korean Journal of Radiology*, 15(5):554–577.

[Jenkinson et al., 2002] Jenkinson, M., Bannister, P., Brady, M., and Smith, S. (2002). Improved optimization for the robust and accurate linear registration and motion correction of brain images. *NeuroImage*, 17(2):825–841.

[Jenkinson et al., 2012] Jenkinson, M., Beckmann, C. F., Behrens, T. E., Woolrich, M. W., and Smith, S. M. (2012). FSL. *NeuroImage*, 62(2):782–790.

[Jenkinson and Smith, 2001a] Jenkinson, M. and Smith, S. (2001a). A global optimisation method for robust affine registration of brain images. *Medical Image Analysis*, 5(2):143–156.

[Jenkinson and Smith, 2001b] Jenkinson, M. and Smith, S. (2001b). A global optimisation method for robust affine registration of brain images. *Medical Image Analysis*, 5(2):143–156.

[Jochimsen et al., 2016] Jochimsen, T. H., Zeisig, V., Schulz, J., Werner, P., Patt, M., Patt, J., Dreyer, A. Y., Boltze, J., Barthel, H., Sabri, O., and Sattler, B.

(2016). Fully automated calculation of image-derived input function in simultaneous PET/MRI in a sheep model. *EJNMMI Physics*, 3:2.

[Kak and Slaney, 1988] Kak, A. C. and Slaney, M. (1988). Principles of Computerized Tomographic Imaging. *Engineering*, 33:327.

[Keereman et al., 2010] Keereman, V., Fierens, Y., Broux, T., De Deene, Y., Lonneux, M., and Vandenberghe, S. (2010). MRI-based attenuation correction for PET/MRI using ultrashort echo time sequences. *Journal of Nuclear Medicine*, 51(5):812–818.

[Keller et al., 2015] Keller, S. H., Hansen, C., Hansen, C., Andersen, F. L., Ladefoged, C., Svarer, C., Kjaer, A., Hojgaard, L., Law, I., Henriksen, O. M., and Hansen, A. E. (2015). Motion correction in simultaneous PET/MR brain imaging using sparsely sampled MR navigators: a clinically feasible tool. *EJNMMI physics*, 2(1):14.

[Kennan and Jäger, 2003] Kennan, R. P. and Jäger, H. R. (2003). T2- and T2*-W DCE-MRI: Blood Perfusion and Volume Estimation using Bolus Tracking. In *Quantitative MRI of the Brain*, pages 365–412. John Wiley & Sons, Ltd.

[Kety and Schmidt, 1945] Kety, S. S. and Schmidt, C. F. (1945). The determination of cerebral blood flow in man by the use of nitrous oxide in low concentrations. *American Journal of Physiology*, 143:53–66.

[Khaligni et al., 2016a] Khaligni, M., Fan, A., Delso, G., Gulaka, P. K., Shen, B., Hoehne, A., Singh, P., Park, J., Holley, D., Chin, F. T., and Zaharchuk,

G. (2016a). Non-invasive estimation of arterial input function for imaging of cerebral blood flow on a PET/MR scanner. International Society for Magnetic Resonance in Medicine Annual Meeting.

[Khaligni et al., 2016b] Khaligni, M., Fan, A., Delso, G., Gulaka, P. K., Shen, B., Hoehne, A., Singh, P., Park, J., Holley, D., Chin, F. T., and Zaharchuk, G. (2016b). Optimizing MR Angiography for Image-based Arterial Input Function Estimation in 15O-H2O Study. Conference on PET/MR and SPECT/MR.

[Kim et al., 1994] Kim, C. K., Gupta, N. C., Chandramouli, B., and Alavi, A. (1994). Standardized uptake values of FDG: body surface area correction is preferable to body weight correction. *Journal of Nuclear Medicine*, 35(1):164–7.

[Kim and Kim, 2007] Kim, H. S. and Kim, S. Y. (2007). A prospective study on the added value of pulsed arterial spin-labeling and apparent diffusion coefficients in the grading of gliomas. *American Journal of Neuroradiology*, 28:1693–1699.

[Kimura et al., 2009] Kimura, N., Yamamoto, Y., Kameyama, R., Hatakeyama, T., Kawai, N., and Nishiyama, Y. (2009). Diagnostic value of kinetic analysis using dynamic 18F-FDG-PET in patients with malignant primary brain tumor. *Nuclear Medicine Communications*, 30:602–609.

[Kinahan et al., 1998] Kinahan, P. E., Townsend, D. W., Beyer, T., and Sashin, D. (1998). Attenuation correction for a combined 3D PET/CT scanner. *Medical Physics*, 25:2046–2053.

[Krejza et al., 2006a] Krejza, J., Arkuszewski, M., Kasner, S. E., Weigele, J., Ustymowicz, A., Hurst, R. W., Cucchiara, B. L., and Messe, S. R. (2006a). Carotid artery diameter in men and women and the relation to body and neck size. *Stroke*, 37(4):1103–1105.

[Krejza et al., 2006b] Krejza, J., Arkuszewski, M., Kasner, S. E., Weigele, J., Ustymowicz, A., Hurst, R. W., Cucchiara, B. L., and Messe, S. R. (2006b). Carotid artery diameter in men and women and the relation to body and neck size. *Stroke*, 37:1103–1105.

[Kudo et al., 2007] Kudo, K., Sasaki, M., Momoshima, S., Yamada, K, T. S., and Shirato, H. (2007). Development of Perfusion Mismatch Analyzer (PMA): Fully Automated, Operator-Independent, and Standardized PWI-DWI Analysis Software. *Radiological Society of North America 2007 Scientific Assembly and Annual Meeting*, 33(9).

[Kwong et al., 1995] Kwong, K. K., Chesler, D. A., Weisskoff, R. M., Donahue, K. M., Davis, T. L., Ostergaard, L., Campbell, T. A., and Rosen, B. R. (1995). MR perfusion studies with T1-weighted echo planar imaging. *Magnetic Resonance in Medicine*, 34:878–887.

[Landaw and DiStefano, 1984] Landaw, E. M. and DiStefano, J. J. (1984). Multiexponential, multicompartmental, and noncompartmental modeling. II. Data analysis and statistical considerations. *The American Journal of Physiology*, 246:665–677.

[Lauterbur, 1973] Lauterbur, P. (1973). Image formation by induced local interactions: Examples employing nuclear magnetic resonance. *Nature*, 242:190–191.

[Leenders et al., 1990] Leenders, K. L., Perani, D., Lammertsma, A. A., Heather, J. D., Buckingham, P., Healy, M. J., Gibbs, J. M., Wise, R. J., Hatazawa, J., and Herold, S. (1990). Cerebral blood flow, blood volume and oxygen utilization. Normal values and effect of age. *Brain*, 113:27–47.

[Levin et al., 2014] Levin, C., Deller, T., Peterson, W., Maramraju, S. H., Kim, C., and Prost, R. (2014). Initial results of simultaneous whole-body ToF PET/MR. *Society of Nuclear Medicine Annual Meeting Abstracts*, 55(1_MeetingAbstracts):660.

[Levin et al., 2016] Levin, C. S., Maramraju, S. H., Khalighi, M. M., Deller, T. W., Delso, G., and Jansen, F. (2016). Design Features and Mutual Compatibility Studies of the Time-of-Flight PET Capable GE SIGNA PET/MR System. *IEEE Transactions on Medical Imaging*, 0062(c):1–1.

[Lewellen, 1998] Lewellen, T. K. (1998). Time-of-flight PET.

[Litton, 1997] Litton, J. E. (1997). Input function in PET brain studies using MR-defined arteries. *Journal of Computer Assisted Tomography*, 21(6):907–909.

[Logan et al., 1990] Logan, J., Fowler, J. S., Volkow, N. D., Wolf, A. P., Dewey, S. L., Schlyer, D. J., MacGregor, R. R., Hitzemann, R., Bendriem, B., and Gatley, S. J. (1990). Graphical analysis of reversible radioligand binding from time-

activity measurements applied to [N-11C-methyl]-(-)-cocaine PET studies in human subjects. *Journal of Cerebral Blood Flow and Metabolism*, 10:740–747.

[Lubberink et al., 2010] Lubberink, M., Harms, H. J., Halbmeijer, R., de Haan, S., Knaapen, P., and Lammertsma, A. A. (2010). Low-Dose Quantitative Myocardial Blood Flow Imaging Using 15O-Water and PET Without Attenuation Correction. *Journal of Nuclear Medicine*, 51(4):575–580.

[Lyoo et al., 2014] Lyoo, C. H., Zanotti-Fregonara, P., Zoghbi, S. S., Liow, J. S., Xu, R., Pike, V. W., Zarate, C. A., Fujita, M., and Innis, R. B. (2014). Image-derived input function derived from a supervised clustering algorithm: Methodology and validation in a clinical protocol using [11C](R)-rolipram. *PLoS ONE*, 9(2).

[Maintz and Viergever, 1998] Maintz, J. B. and Viergever, M. A. (1998). A survey of medical image registration. *Medical Image Analysis*, 2(1):1–36.

[Mansfield, 1977] Mansfield, P. (1977). Multi-planar image formation using NMR spin echoes. *Journal of Physics C*, 10:55–58.

[Marner et al., 2009] Marner, L., Gillings, N., Comley, R. a., Baaré, W. F. C., Rabiner, E. a., Wilson, A. a., Houle, S., Hasselbalch, S. G., Svarer, C., Gunn, R. N., Laruelle, M., and Knudsen, G. M. (2009). Kinetic modeling of 11C-SB207145 binding to 5-HT4 receptors in the human brain in vivo. *Journal of Nuclear Medicine*, 50(6):900–908.

[Martinez-Möller et al., 2009] Martinez-Möller, A., Souvatzoglou, M., Delso, G., Bundschuh, R. a., Chefd'hotel, C., Ziegler, S. I., Navab, N., Schwaiger, M., and Nekolla, S. G. (2009). Tissue classification as a potential approach for attenuation correction in whole-body PET/MRI: evaluation with PET/CT data. *Journal of Nuclear Medicine*, 50(4):520–526.

[McRobbie et al., 2006] McRobbie, D. W., Moore, E. A., Graves, M. J., and Prince, M. R. (2006). *MRI from Picture to Proton*. Cambridge University Press, second edition.

[Mehranian et al., 2016] Mehranian, A., Arabi, H., and Zaidi, H. (2016). Vision 20/20: Magnetic resonance imaging-guided attenuation correction in PET/MRI: Challenges, solutions, and opportunities. *Medical Physics*, 43(3):1130–1155.

[Meltzer et al., 1990] Meltzer, C. C., Leal, J. P., Mayberg, H. S., Wagner, H. N., and Frost, J. J. (1990). Correction of PET data for partial volume effects in human cerebral cortex by MR imaging. *Journal of Computer Assisted Tomography*, 14(4):561–70.

[Meyer et al., 1992] Meyer, C. H., Hu, B. S., Nishimura, D. G., and Macovski, A. (1992). Fast spiral coronary artery imaging. *Magnetic Resonance in Medicine*, 28:202–213.

[Meyer, 1989] Meyer, E. (1989). Simultaneous correction for tracer arrival delay and dispersion in CBF measurements by the H215O autoradiographic method and dynamic PET. *Journal of Nuclear Medicine*, 30(6):1069–1078.

[Miller, 2004] Miller, K. L. (2004). *Novel methods for steady state neuroimaging* . PhD thesis, Stanford University.

[Modat et al., 2010] Modat, M., Ridgway, G. R., Taylor, Z. A., Lehmann, M., Barnes, J., Hawkes, D. J., Fox, N. C., and Ourselin, S. (2010). Fast free-form deformation using graphics processing units. *Computer Methods and Programs in Biomedicine*, 98(3):278–284.

[Mosconi et al., 2009] Mosconi, L., Mistur, R., Switalski, R., Tsui, W. H., Glodzik, L., Li, Y., Pirraglia, E., De Santi, S., Reisberg, B., Wisniewski, T., and De Leon, M. J. (2009). FDG-PET changes in brain glucose metabolism from normal cognition to pathologically verified Alzheimer's disease. *European Journal of Nuclear Medicine and Molecular Imaging*, 36(5):811–822.

[Mourik et al., 2011] Mourik, J. E. M., Lubberink, M., Lammertsma, A. A., and Boellaard, R. (2011). Image derived input functions: Effects of motion on tracer kinetic analyses. *Molecular Imaging and Biology*, 13(1):25–31.

[Mugler and Brookeman, 1990] Mugler, J. P. and Brookeman, J. R. (1990). Three-dimensional magnetization-prepared rapid gradient-echo imaging (3D MP RAGE). *Magnetic Resonance in Medicine*, 15(1):152–157.

[Müller-Gärtner et al., 1992] Müller-Gärtner, H. W., Links, J. M., Prince, J. L., Bryan, R. N., McVeigh, E., Leal, J. P., Davatzikos, C., and Frost, J. J. (1992). Measurement of radiotracer concentration in brain gray matter using positron

emission tomography: MRI-based correction for partial volume effects. *Journal of Cerebral Blood Flow and Metabolism*, 12(4):571–583.

[Muzi et al., 2012] Muzi, M., O'Sullivan, F., Mankoff, D. a., Doot, R. K., Pierce, L. a., Kurland, B. F., Linden, H. M., and Kinahan, P. E. (2012). Quantitative assessment of dynamic PET imaging data in cancer imaging. *Magnetic Resonance Imaging*, 30(9):1203–15.

[Muzic and Cornelius, 2001] Muzic, R. F. and Cornelius, S. (2001). COMKAT: compartment model kinetic analysis tool. *Journal of Nuclear Medicine*, 42(4):636–45.

[Nichols et al., 2002] Nichols, T. E., Qi, J., Asma, E., and Leahy, R. M. (2002). Spatiotemporal reconstruction of list-mode PET data. *IEEE Transactions on Medical Imaging*, 21:396–404.

[Nitz, 1999] Nitz, W. R. (1999). MR imaging: Acronyms and clinical applications.

[Ogden et al., 2010] Ogden, R. T., Zanderigo, F., Choy, S., Mann, J. J., and Parsey, R. V. (2010). Simultaneous estimation of input functions: an empirical study. *Journal of Cerebral Blood Flow and Metabolism*, 30(4):816–826.

[Oliveira and Tavares, 2014] Oliveira, F. P. M. and Tavares, J. M. R. S. (2014). Medical image registration: a review. *Computer Methods in Biomechanics and Biomedical Engineering*, 17(2):73–93.

[Orton et al., 2008] Orton, M. R., D'Arcy, J. A., Walker-Samuel, S., Hawkes, D. J., Atkinson, D., Collins, D. J., and Leach, M. O. (2008). Computationally efficient

vascular input function models for quantitative kinetic modelling using DCE-MRI. *Physics In Medicine And Biology*, 53(5):1225–1239.

[Pakkenberg and Gundersen, 1997] Pakkenberg, B. and Gundersen, H. J. G. (1997). Neocortical neuron number in humans: Effect of sex and age. *Journal of Comparative Neurology*, 384(2):312–320.

[Parker et al., 2006] Parker, G. J. M., Roberts, C., Macdonald, A., Buonaccorsi, G. A., Cheung, S., Buckley, D. L., Jackson, A., Watson, Y., Davies, K., and Jayson, G. C. (2006). Experimentally-Derived Functional Form for a Input Function for Dynamic Contrast-Enhanced MRI. *Magnetic Resonance in Medicine*, 1000(October 2005):993–1000.

[Patlak et al., 1983] Patlak, C. S., Blasberg, R. G., Fenstermacher, J. D., et al. (1983). Graphical evaluation of blood-to-brain transfer constants from multiple-time uptake data. *Journal of Cerebral Blood Flow and Metabolism*, 3(1):1–7.

[Phelps et al., 1979] Phelps, M., Huang, S., Hoffman, E., Selin, C., Sokoloff, L., and Kuhl, D. (1979). Tomographic measurement of local cerebral glucose metabolic rate in humans with (F-18) 2-fluoro-2-deoxy-D-glucose: validation of method. *Annals Neurology*, 6(5):371–388.

[Poulin et al., 2013] Poulin, E., Lebel, R., Croteau, E., Blanchette, M., Tremblay, L., Lecomte, R., Bentourkia, M., and Lepage, M. (2013). Conversion of arterial input functions for dual pharmacokinetic modeling using Gd-DTPA/MRI and 18F-FDG/PET. *Magnetic Resonance in Medicine*, 69:781–792.

[Poulin et al., 2015] Poulin, É., Lebel, R., Croteau, É., Blanchette, M., Tremblay, L., Lecomte, R., Bentourkia, M., and Lepage, M. (2015). Optimization of the reference region method for dual pharmacokinetic modeling using Gd-DTPA/MRI and 18F-FDG/PET. *Magnetic Resonance in Medicine*, 73(2):740–748.

[Quarantelli et al., 2004] Quarantelli, M., Berkouk, K., Prinster, A., Landeau, B., Svarer, C., Balkay, L., Alfano, B., Brunetti, A., Baron, J.-C., and Salvatore, M. (2004). Integrated software for the analysis of brain PET/SPECT studies with partial-volume-effect correction. *Journal of Nuclear Medicine*, 45(2):192–201.

[Reader et al., 2002] Reader, A. J., Ally, S., Bakatselos, F., Manavaki, R., Walledge, R. J., Jeavons, A. P., Julyan, P. J., Zhao, S., Hastings, D. L., and Zweit, J. (2002). One-pass list-mode EM algorithm for high-resolution 3-D PET image reconstruction into large arrays. *IEEE Transactions on Nuclear Science*, 49 I:693–699.

[Rempp et al., 1994] Rempp, K. a., Brix, G., Wenz, F., Becker, C. R., Gückel, F., and Lorenz, W. J. (1994). Quantification of regional cerebral blood flow and volume with dynamic susceptibility contrast-enhanced MR imaging. *Radiology*, 193(3):637–641.

[Renkin, 1959] Renkin, E. M. (1959). Transport of potassium-42 from blood to tissue in isolated mammalian skeletal muscles. *American Journal of Physiology*, 197:1205–1210.

[Roentgen, 1895] Roentgen, W. C. (1895). *Eine neue Art von Strahlen*. II. Mittheilung.

[Roselli et al., 2010] Roselli, F., Pisciotta, N. M., Aniello, M. S., Niccoli-Asabella, A., Defazio, G., Livrea, P., and Rubini, G. (2010). Brain F-18 Fluorocholine PET/CT for the assessment of optic pathway glioma in neurofibromatosis-1. *Clinical Nuclear Medicine*, 35(10):838–9.

[Rosen et al., 1990] Rosen, B. R., Belliveau, J. W., Vevea, J. M., and Brady, T. J. (1990). Perfusion imaging with NMR contrast agents. In *Magnetic Resonance in Medicine*, volume 14, pages 249–265.

[Rousset et al., 1998a] Rousset, O. G., Ma, Y., and Evans, A. C. (1998a). Correction for partial volume effects in PET: principle and validation. *Journal of Nuclear Medicine*, 39(5):904–911.

[Rousset et al., 1998b] Rousset, O. G., Ma, Y., Evans, A. C., et al. (1998b). Correction for partial volume effects in pet: principle and validation. *Journal of Nuclear Medicine*, 39(5):904–911.

[Rueckert et al., 2006] Rueckert, D., Aljabar, P., Heckemann, R. A., Hajnal, J. V., and Hammers, A. (2006). Diffeomorphic Registration Using B-Splines. In *MICCAI*, pages 702–709.

[Rutland, 1985] Rutland, M. D. (1985). A comprehensive analysis of renal DTPA studies. I. Theory and normal values. *Nuclear Medicine Communications*, 6:11–20.

[Salerno and Beller, 2009] Salerno, M. and Beller, G. A. (2009). Noninvasive assessment of myocardial perfusion.

[Saloner, 1995] Saloner, D. (1995). The AAPM/RSNA physics tutorial for residents. An introduction to MR angiography. *Radiographics*, 15(2):453–65.

[Sanabria-Bohórquez, 2003] Sanabria-Bohórquez, S. (2003). Image-Derived Input Function for [11C]Flumazenil Kinetic Analysis in Human Brain. *Molecular Imaging & Biology*, 5(2):72–78.

[Sari et al., 2016] Sari, H., Erlandsson, K., Law, I., Larsson, H. B., Ourselin, S., Arridge, S., Atkinson, D., and Hutton, B. F. (2016). Estimation of an image derived input function with MR-defined carotid arteries in FDG-PET human studies using a novel partial volume correction method. *Journal of Cerebral Blood Flow and Metabolism*.

[Sari et al., 2014] Sari, H., Erlandsson, K., Thielemans, K., Atkinson, D., Arridge, S., Ourselin, S., and Hutton, B. (2014). Incorporation of MRI-AIF information for improved kinetic modelling of dynamic PET data. *EJNMMI Physics*, 1(Suppl 1):A43.

[Schild, 1990] Schild, H. (1990). *MRI, Made Easy: (... Well Almost)*. Schering AG.

[Sekine et al., 2016] Sekine, T., Burgos, N., Warnock, G., Huellner, M. W., Buck, a., ter Voert, E. E., Cardoso, M. J., Hutton, B. F., Ourselin, S., Veit-Haibach, P., and Delso, G. (2016). Multi atlas-based attenuation correction for brain FDG-

PET imaging using a TOF-PET/MR scanner- comparison with clinical single atlas- and CT-based attenuation correction. *Journal of Nuclear Medicine*.

[Shao et al., 1997] Shao, Y., Cherry, S. R., Farahani, K., Meadors, K., Siegel, S., Silverman, R. W., and Marsden, P. K. (1997). Simultaneous PET and MR imaging. *Physics in Medicine and Biology*, 42(10):1965–1970.

[Sharma and McConathy, 2013] Sharma, A. and McConathy, J. (2013). Overview of PET tracers for brain tumor imaging. *PET Clinics*, 8(2):129–146.

[Shepp and Vardi, 1982] Shepp, L. A. and Vardi, Y. (1982). Maximum likelihood reconstruction for emission tomography. *IEEE Transactions on Medical Imaging*, 1:113–122.

[Shidahara et al., 2009] Shidahara, M., Tsoumpas, C., Hammers, A., Boussion, N., Visvikis, D., Suhara, T., Kanno, I., and Turkheimer, F. E. (2009). Functional and structural synergy for resolution recovery and partial volume correction in brain PET. *NeuroImage*, 44(2):340–348.

[Shrestha et al., 2014] Shrestha, S. S., Liow, J.-S., Lu, S., Jenko, K., Gladding, R. L., Svenningsson, P., Morse, C. L., Zoghbi, S. S., Pike, V. W., and Innis, R. B. (2014). (11)C-CUMI-101, a PET radioligand, behaves as a serotonin 1A receptor antagonist and also binds to α(1) adrenoceptors in brain. *Journal of Nuclear Medicine*, 55(1):141–6.

[Shukla-Dave et al., 2009] Shukla-Dave, A., Lee, N., Stambuk, H., Wang, Y., Huang, W., Thaler, H. T., Patel, S. G., Shah, J. P., and Koutcher, J. a. (2009).

Average arterial input function for quantitative dynamic contrast enhanced magnetic resonance imaging of neck nodal metastases. *BMC Medical Physics*, 9:4.

[Soret et al., 2007] Soret, M., Bacharach, S. L., and Buvat, I. (2007). Partial-volume effect in PET tumor imaging. *Journal of Nuclear Medicine*, 48(6):932–45.

[Spence et al., 2004] Spence, A. M., Muzi, M., Mankoff, D. A., O'Sullivan, S. F., Link, J. M., Lewellen, T. K., Lewellen, B., Pham, P., Minoshima, S., Swanson, K., and Krohn, K. A. (2004). 18F-FDG PET of gliomas at delayed intervals: improved distinction between tumor and normal gray matter. *Journal of Nuclear Medicine*, 45:1653–1659.

[Su et al., 2013a] Su, Y., Arbelaez, A. M., Benzinger, T. L., Snyder, A. Z., Vlassenko, A. G., Mintun, M. A., and Raichle, M. E. (2013a). Noninvasive estimation of the arterial input function in positron emission tomography imaging of cerebral blood flow. *Journal of Cerebral Blood Flow and Metabolism*, 33(1):115–121.

[Su et al., 2013b] Su, Y., Arbelaez, A. M., Benzinger, T. L. S., Snyder, A. Z., Vlassenko, A. G., Mintun, M. a., and Raichle, M. E. (2013b). Noninvasive estimation of the arterial input function in positron emission tomography imaging of cerebral blood flow. *Journal of Cerebral Blood Flow and Metabolism*, 33(1):115–21.

[Su et al., 2015] Su, Y., Blazey, T. M., Snyder, A. Z., Raichle, M. E., Hornbeck, R. C., Aldea, P., Morris, J. C., and Benzinger, T. L. S. (2015). Quantitative amyloid imaging using image-derived arterial input function. *PLoS ONE*, 10(4):1–16.

[Surti et al., 2007] Surti, S., Kuhn, A., Werner, M. E., Perkins, A. E., Kolthammer, J., and Karp, J. S. (2007). Performance of Philips Gemini TF PET/CT scanner with special consideration for its time-of-flight imaging capabilities. *Journal of Nuclear Medicine*, 48:471–480.

[Tahari et al., 2014] Tahari, A. K., Chien, D., Azadi, J. R., and Wahl, R. L. (2014). Optimum lean body formulation for correction of standardized uptake value in PET imaging. *Journal of Nuclear Medicine*, 55(9):1481–4.

[Takikawa et al., 1993] Takikawa, S., Dhawan, V., Spetsieris, P., Robeson, W., Chaly, T., Dahl, R., Margouleff, D., and Eidelberg, D. (1993). Noninvasive quantitative fluorodeoxyglucose PET studies with an estimated input function derived from a population-based arterial blood curve. *Radiology*, 188:131–136.

[Thielemans et al., 2012] Thielemans, K., Tsoumpas, C., Mustafovic, S., Beisel, T., Aguiar, P., Dikaios, N., and Jacobson, M. W. (2012). STIR: software for tomographic image reconstruction release 2. *Physics in Medicine and Biology*, 57(4):867.

[Thomsen et al., 2002] Thomsen, H. S., Almèn, T., and Morcos, S. K. (2002). Gadolinium-containing contrast media for radiographic examinations: a position

paper. *European Radiology*, 12:2600–2605.

[Tofts et al., 1999] Tofts, P. S., Brix, G., Buckley, D. L., Evelhoch, J. L., Henderson, E., Knopp, M. V., Larsson, H. B. W., Lee, T.-y., Mayr, N. A., Parker, G. J. M., Port, R. E., Taylor, J., and Weisskoff, R. M. (1999). Contrast-Enhanced T 1 -Weighted MRI of a Diffusable Tracer : Standardized Quantities and Symbols. 232:223–232.

[Tofts and Kermode, 1991] Tofts, P. S. and Kermode, A. G. (1991). Measurement of the blood-brain barrier permeability and leakage space using dynamic MR imaging. 1. Fundamental concepts. *Magnetic Resonance in Medicine*, 17(2):357–367.

[Tomasi et al., 2012] Tomasi, G., Kimberley, S., Rosso, L., Aboagye, E., and Turkheimer, F. (2012). Double-input compartmental modeling and spectral analysis for the quantification of positron emission tomography data in oncology. *Physics in Medicine and Biology*, 57(7):1889–906.

[Tonietto et al., 2016] Tonietto, M., Rizzo, G., Veronese, M., Fujita, M., Zoghbi, S. S., Zanotti-Fregonara, P., and Bertoldo, A. (2016). Plasma radiometabolite correction in dynamic PET studies: Insights on the available modeling approaches. *Journal of Cerebral Blood Flow and Metabolism*, 36(2):326–39.

[Trebossen et al., 1998] Trebossen, R., Bendriem, B., and Ribeiro, M. J. (1998). Quantifying cerebral PET with FDG using dynamic internal carotid arteries

imaging. *Nuclear Science Symposium, 1998. Conference Record.*, pages 1737–1740.

[Turkheimer et al., 1999] Turkheimer, F. E., Brett, M., Visvikis, D., and Cunningham, V. J. (1999). Multiresolution analysis of emission tomography images in the wavelet domain. *Journal of Cerebral Blood Flow and Metabolism*, 19(11):1189–208.

[van der Weerdt et al., 2001] van der Weerdt, a. P., Klein, L. J., Boellaard, R., Visser, C. a., Visser, F. C., and Lammertsma, a. a. (2001). Image-derived input functions for determination of MRGlu in cardiac (18)F-FDG PET scans. *Journal of Nuclear Medicine*, 42(11):1622–1629.

[Van Velden et al., 2008] Van Velden, F. H. P., Kloet, R. W., Van Berckel, B. N. M., Molthoff, C. F. M., Lammertsma, A. A., and Boellaard, R. (2008). Gap filling strategies for 3-D-FBP reconstructions of high-resolution research tomograph scans. *IEEE Transactions on Medical Imaging*, 27(7):934–942.

[Wagenknecht et al., 2013] Wagenknecht, G., Kaiser, H. J., Mottaghy, F. M., and Herzog, H. (2013). MRI for attenuation correction in PET: Methods and challenges.

[Watabe et al., 2006] Watabe, H., Ikoma, Y., Kimura, Y., Naganawa, M., and Shidahara, M. (2006). PET kinetic analysis–compartmental model. *Annals of Nuclear Medicine*, 20(9):583–8.

[Watson et al., 1996] Watson, C., Newport, D., and Casey, M. (1996). A single scatter simulation technique for scatter correction in 3D PET. In *Three-Dimensional Image Reconstruction in Radiology and Nuclear Medicine (Computational Imaging and Vision)*, pages 255–268.

[Wilson and Noble, 1999] Wilson, D. L. and Noble, J. A. (1999). An adaptive segmentation algorithm for time-of-flight MRA data. *IEEE Transactions on Medical Imaging*, 18(10):938–945.

[Wollenweber et al., 2012] Wollenweber, S. D., Ambwani, S., Lonn, A. H. R., Mullick, R., Wiesinger, F., Piti, Z., Tari, A., Novak, G., and Fidrich, M. (2012). Evaluation of an atlas-based pet head attenuation correction using pet/ct amp; mr patient data. In *Nuclear Science Symposium and Medical Imaging Conference (NSS/MIC), 2012 IEEE*, pages 4048–4053.

[Wong et al., 2001] Wong, K. P., Feng, D., Meikle, S. R., and Fulham, M. J. (2001). Simultaneous estimation of physiological parameters and the input function–in vivo PET data. *IEEE Transactions on Information Technology in Biomedicine*, 5(1):67–76.

[Wong et al., 2002] Wong, K.-p., Meikle, S. R., Member, S., Feng, D., and Fulham, M. J. (2002). Estimation of Input Function and Kinetic Parameters Using Simulated Annealing : Application in a. *IEEE Transactions on Nuclear Science*, 49(3):707–713.

[Woolrich et al., 2009] Woolrich, M. W., Jbabdi, S., Patenaude, B., Chappell, M., Makni, S., Behrens, T., Beckmann, C., Jenkinson, M., and Smith, S. M. (2009). Bayesian analysis of neuroimaging data in FSL. *NeuroImage*, 45(1 Suppl).

[Yang et al., 1996] Yang, J., Huang, S. C., Mega, M., Lin, K. P., Toga, A. W., Member, A., Small, G. W., and Phelps, M. E. (1996). Investigation of Partial Volume Correction Methods for Brain FDG PET Studies. *IEEE Transactions on Nuclear Science*, 43(6):3322–3327.

[Yaqub et al., 2012] Yaqub, M., van Berckel, B. N. M., Schuitemaker, A., Hinz, R., Turkheimer, F. E., Tomasi, G., Lammertsma, A. A., and Boellaard, R. (2012). Optimization of supervised cluster analysis for extracting reference tissue input curves in (R)-[(11)C]PK11195 brain PET studies. *Journal of Cerebral Blood Flow and Metabolism*, 32(8):1600–8.

[Yushkevich et al., 2006] Yushkevich, P. A., Piven, J., Hazlett, H. C., Smith, R. G., Ho, S., Gee, J. C., and Gerig, G. (2006). User-guided 3D active contour segmentation of anatomical structures: significantly improved efficiency and reliability. *Neuroimage*, 31(3):1116–1128.

[Zanderigo et al., 2014] Zanderigo, F., Ogden, R. T., and Parsey, R. V. (2014). Non-invasive blood-free full quantification of positron emission tomography radioligand binding. *Journal of Cerebral Blood Flow and Metabolism*, 35(1):148–156.

[Zanotti-Fregonara et al., 2009a] Zanotti-Fregonara, P., Fadaili, E. M., Maroy, R., Comtat, C., Souloumiac, A., Jan, S., Ribeiro, M.-J., Gaura, V., Bar-Hen, A., and

Trébossen, R. (2009a). Comparison of eight methods for the estimation of the image-derived input function in dynamic [(18)F]-FDG PET human brain studies. *Journal of Cerebral Blood Flow and Metabolism*, 29(11):1825–35.

[Zanotti-Fregonara et al., 2009b] Zanotti-Fregonara, P., Fadaili, E. M., Maroy, R., Comtat, C., Souloumiac, A., Jan, S., Ribeiro, M.-J., Gaura, V., Bar-Hen, A., and Trebossen, R. (2009b). Comparison of eight methods for the estimation of the image-derived input function in dynamic [(18)F]-FDG PET human brain studies. *Journal of Cerebral Blood Flow and Metabolism*, 29(11):1825–1835.

[Zanotti-Fregonara et al., 2012] Zanotti-Fregonara, P., Liow, J.-S., Comtat, C., Zoghbi, S. S., Zhang, Y., Pike, V. W., Fujita, M., and Innis, R. B. (2012). Image-derived input function in PET brain studies: blood-based methods are resistant to motion artifacts. *Nuclear medicine communications*, 33(9):982–9.